Radial transport of stars and gas in the plane of disc galaxies

A study with numerical simulations and semi-analytic models

Periklis Okalidis

München 2022

Radial transport of stars and gas in the plane of disc galaxies

A study with numerical simulations and semi-analytic models

Periklis Okalidis

Dissertation
der Fakultät für Physik
der Ludwig-Maximilians-Universität
München

vorgelegt von
Periklis Okalidis
aus Thessaloniki, Greece

München, den 01/09/2022

Erstgutachter: Prof. Dr. Volker Springel
Zweitgutachter: PD Dr. Klaus Dolag
Tag der mündlichen Prüfung: 25th October 2022

Table of Contents

List of Figures

List of Tables

Zusammenfassung

Die Galaxienentstehung und -entwicklung ist eines der vielfältigsten Forschungsthemen auf dem Gebiet der Astrophysik und wurde deshalb bereits in einer Vielzahl von Forschungsarbeiten sowohl aus theoretischer als auch aus beobachtender Perspektive untersucht. Insbesondere Scheibengalaxien stoßen auf großes Interesse, da sie vermutlich die ersten Strukturen sind, die sich direkt nach dem Kollaps von Gas in Halos aus dunkler Materie bilden, als Folge des Drehimpulses, der von der einfallenden Materie erhalten bleibt. Die Entwicklung der entstehenden Scheibe ist besonders faszinierend aufgrund der Fülle interner und externer physikalischer Prozesse, die auf das System einwirken. Im Einführungskapitel dieser Arbeit diskutieren wir die diesbezügliche Theorie der Galaxienentstehung genauer.

In dieser Forschungsarbeit beschäftigen wir uns mit der konkreten Frage, wie Materie innerhalb der schmalen Ebene einer galaktischen Scheibe radial transportiert wird. Wir möchten untersuchen, wie Gas von den äußeren in die zentralen Regionen der Galaxie geleitet wird und welche strukturellen Eigenschaften der Scheibe dazu beitragen, stärkere Gasströme zu induzieren. In Bezug auf die stellare Komponente ist es unser Ziel zu verstehen, ob und inwieweit sich Sterne zu anderen Radien als die, bei denen sie geboren wurden, bewegen, ein Prozess, der als Sternmigration bezeichnet wird, und welche Mechanismen dieses Verhalten antreiben. Wir nähern uns diesen Fragen aus einer theoretischen Perspektive, indem wir leistungsstarke Vorhersagewerkzeuge nutzen, die durch numerische Simulationen und sogenannte semi-analytische Modelle der Galaxienentstehung bereitgestellt werden.

Im ersten Hauptkapitel untersuchen wir die Radialbewegungen von kaltem, sternbildendem Gas in der säkularen Entwicklungsphase eines Satzes von 14 kosmologischen magnetohydrodynamischen Simulationen von Galaxien mit einer Masse ähnlich der Milchstraße. Diese Modelle stammen aus dem sogenannten Auriga-Projekt. Wir untersuchen den radialen Materialtransport innerhalb der Scheibenebene auf Basis einer Reihe konzentrischer Ringe. Für das Gas, das sich zu einem gegebenen Zeitpunkt in einem Ring befindet, berechnen wir für jeden Ring zwei Größen als Funktion von Zeit und Radius: 1) die radiale Massenströmung des Gases; und 2) die radiale Ausbreitung des Gases relativ zur Massenströmung. Durch Mittelung der Daten aller Galaxien finden wir, dass die radiale Ausbreitung mit dem Radius in Form eines Potenzgesetzes zunimmt, mit starken sekundären Abhängigkeiten wie dem Anteil des angesammelten Materials und der lokalen radialen Geschwindigkeitsdispersion des Gases. Die Bewegung des Gases in den inneren Scheibenregionen wird durch eine radial unabhängige mittlere Einwärtsströmungsgeschwindigkeit von $-2,4\,\mathrm{km\,s^{-1}}$ gut beschrieben. Die Streuung um diesen Wert wird durch die Änderung des Drehimpulses des Gases und auch durch die Menge an angelagertem Material bestimmt.

Im zweiten Hauptkapitel untersuchen wir das Vorhandensein und die Bedeutung der Sternmigration in der Entwicklung von 17 milchstraßenähnlichen Scheibengalaxien aus den Auriga Simulationen mit einer Sternmasse $10 < \log(M_*/\mathrm{M}_\odot) < 11$. Wir vergleichen die Geburtsradien der Sterne mit ihren Radien bei $z = 0$ für jedes System und präsentieren Mittelwerte der Stärke der Sternwanderung als Funktion von Radius und Sternalter, die zwischen 1-4 kpc variieren. Wir untersuchen auch die Auswirkung der Migration auf das Alter und die radialen Profile der Metallizität in den Scheiben. Wir finden mehrere Fälle einer Abflachung des Altersgradienten aufgrund von Migration, sowie signifikante Änderungen der Metallizitätsprofile für ältere Sternpopulationen und in Scheibengalaxien, die einen starken Balken entwickeln. Darüber hinaus untersuchen wir die Sternmigration aus der Sicht der Änderung des galaktozentrischen Radius (ΔR) und aus Sicht von Änderungen des orbitalen Führungsradius (ΔR_g) von Sternteilchen zwischen gegebenen Zeitintervallen. Wir finden, dass Sterne nur in den äußeren Teilen der Scheiben und für bestimmte Galaxien, die einen schwachen Balken haben, näherungsweise in der Form eines Diffusionsprozesses wandern. Galaxien mit starken Balken zeigen eine stärkere Sternmigration, aber ihre zeitliche Entwicklung ist langsamer als bei einer Diffusion. Abschließend geben wir Parametrisierungen an, die die Abhängigkeit der Stärke der radialen Migration als Funktion von Zeit und Radius beschreiben.

Im dritten Hauptkapitel wenden wir die Parametrisierungen, die wir durch Analyse der Auriga Simulationen bestimmt haben, auf das semi-analytische Modell “L-Galaxies” der Galaxienentstehung und -entwicklung an. Wir aktualisieren dabei das radiale Strömungsrezept, das derzeit in L-Galaxies verwendet wird, und fügen eine neue Funktionalität hinzu, die die Sternmigration berücksichtigt. Wir beschreiben unsere algorithmische Implementierung zusammen mit den notwendigen Anpassungen, um diese neuen Prozesse in das Modell zu integrieren. Wir diskutieren auch Punkte, die weiterer Forschung bedürfen. In den vorläufigen Ergebnissen, die wir in dieser Dissertation präsentieren, haben wir die Auswirkungen dieser neuartigen Implementierung auf das Ergebnis des Modells sowohl in Bezug auf globale Eigenschaften, wie auch hinsichtlich der Stern- und Gasmasse der Galaxien, als auch bezüglich der radial aufgelösten Profile untersucht. Eine wichtige Erkenntnis ist, dass die neue Implementierung je nach zugrundeliegender räumlicher Auflösung des Modells noch unterschiedliche Ergebnisse liefert.

Am Ende dieser Arbeit fassen wir unsere Schlussfolgerungen zusammen und diskutieren mögliche Erweiterungen in zukünftiger Forschung.

Abstract

Galaxy formation and evolution is the most diverse topic of research in the field of astrophysics and has been studied in a vast number of research projects both from a theoretical and an observational perspective. Disc galaxies in particular draw much interest since they are thought to be the first structures that form directly after the collapse of gas into dark matter halos, as a consequence of the angular momentum which is carried by the infalling matter. The evolution of the disc is even more fascinating because of the plethora of internal and external physical processes that have an effect on the system. We present a discussion on the theory of galaxy formation in the Introduction chapter of this work.

In this thesis we are concerned with the specific question of how matter is transported radially within the narrow plane of a galactic disc. We wish to explore how gas is funnelled from the outer towards the central regions of the galaxy and what structural properties of the disc contribute in inducing stronger gas flows. Regarding the stellar component our goal is to understand whether and to what extent stars move to radii other than the one they were born in, a process called stellar migration, and what mechanisms are driving this behaviour. We approach these questions from a theoretical perspective by utilising the powerful predictive tools provided by numerical simulations and semi-analytic models of galaxy formation.

In the first main chapter, we study the radial motions of cold, star-forming gas in the secular evolution phase of a set of 14 Milky Way-mass galaxies from the Auriga suite of zoom-in cosmological magnetohydrodynamical simulations. We study the radial transport of material within the disc plane in a series of concentric rings. For the gas in each ring at a given time we compute two quantities as a function of time and radius: 1) the radial bulk flow of the gas; and 2) the radial spread of the gas relative to the bulk flow. Averaging the data from all the halos, we find that the radial spread increases with radius in the form of a power law with strong secondary dependencies on the fraction of accreted material and the local radial velocity dispersion of the gas. We find that the bulk motion of gas is well described in the inner disc regions by a radially-independent mean inward flow speed of $-2.4\,\mathrm{km\ s^{-1}}$. The spread around this value relates to the change in angular momentum of the gas and also the amount of accreted material.

In the second main chapter we study the presence and importance of stellar migration in the evolution of 17 Milky-Way like discs with stellar mass $10 < \log(M_*/\mathrm{M_\odot}) < 11$ in Auriga. We compare the birth radii of the stars to their radii at $z = 0$ for each system and present mean values of the strength of stellar migration as a function of radius and stellar age which vary between 1-4 kpc. We also investigate the effect of migration on age and metallicity radial profiles in the discs. We find several cases of age gradient flattening due to migration, but significant changes to metallicity profiles only for older stellar populations and discs that develop a strong bar. Furthermore, we study stellar migration from the perspective of the change of the galactocentric radius (ΔR) and orbital guiding centre radius (ΔR_g) of stellar particles between given time intervals. We find that stars migrate approximately as a diffusion process only in the outer parts of the discs and for particular galaxies that have a weak bar. Strongly barred galaxies in our sample show larger stellar migration but its timestep evolution is slower-than-diffusion. Finally, we give parametrizations that encapsulate the dependence of the strength of the radial migration as a function of time and radius.

In the third main chapter we apply the parametrizations that were extracted in the analysis of Auriga into the L-Galaxies semi-analytic model of galaxy formation and evolution. We are updating the radial flow recipe that is currently used in L-Galaxies and adding anew functionality that accounts for the stellar migration. We describe our algorithmic implementation along with the necessary adaptations in order to incorporate the new recipes to the model as well as potential caveats that require further research. In the preliminary results that we present in this thesis, we have explored the effect of this novel implementation in the outcome of the model both with respect to global properties, such as the stellar and gas mass of the galaxies, and in the radially resolved profiles of the same quantities. The most important finding is that the new implementation yields different results depending on the underlying spatial resolution of the model.

In the end of this thesis we summarize our conclusions and discuss potential extensions of this work in future research.

Chapter 1

Introduction

1.1 Introductory remarks

Galaxies are some of the most complex systems that form in our universe. Consequently, they have been subject to extended research since the early days of the 20th century when Edwin Hubble's observations conclusively pointed to the fact that there are nebular structures at such extreme distances that could not constitute part of our own Galaxy (Hubble, 1929a,b).

Hubble's understanding of galaxy formation and evolution was based on a morphological classification of different types of galaxies in what is known as the Hubble's tuning fork diagram. In this picture galaxies are split into two main evolutionary types; the featureless *elliptical* galaxies which may have a varying degree of ellipticity, ranging from almost circular to highly oblate/prolate objects and the *spiral* galaxies characterised by a thin disc with active star formation and the presence of spiral arms. Spiral galaxies are further separated into those who contain or not an elongated mass concentration in their central regions, which is called a bar. Moreover in the transition between spirals and ellipticals lies the category of *lenticular* galaxies which have a smooth light distribution, similarly to ellipticals, but also contain a thin disc and a bulge like spirals. Finally, in later years the category of *irregular* galaxies, which are usually asymmetric without a pronounced bulge or clearly defined disc, was added to this morphological classification. This picture is shown schematically in Figure 1.1.

This thesis is mainly concerned with the disc structures that we most often encounter in spiral galaxies, hence we explain more extensively their formation and evolution scenarios in the following sections. Even more specifically, we are interested in the *secular evolution* of these galaxies which refers to internal processes that operate during the lifetime of the disc and include among others the accretion of new gas onto the disc, the onset of instabilities that cause the formation of bars and spiral arms and the redistribution of material within the disc via radial flows of gas and stellar migration. All these processes are explored in the remainder of this introduction chapter as well as the main chapters of this thesis. For more extended relevant discussion some of the most useful resources include reviews by Sellwood & Sánchez (2010) and Kormendy & Kennicutt (2004) regarding *secular evolution*, van der Kruit & Freeman (2011) more generally on disc evolution as well as the textbooks by Binney & Tremaine (2008) on galactic dynamics

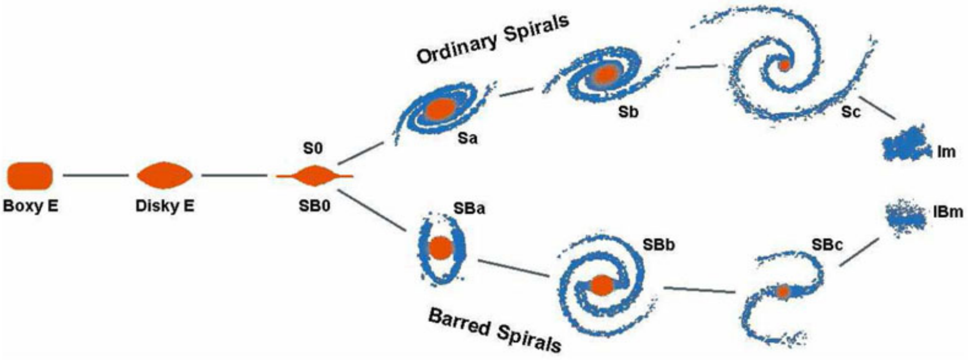

Figure 1.1: Representation of a modern version of the Hubble tuning fork diagram adapted from Kormendy (2013). Elliptical galaxies are shown on the left and spiral galaxies on the right with the various degrees of spiral arm tightness and branching between barred and ordinary spirals. Lenticular galaxies, named S0/SB0, are on the transition between the two populations.

and Mo, van den Bosch & White (Mo et al., 2010) on galaxy formation and evolution as a whole.

1.2 Formation and evolution of disc galaxies

In the standard picture of galaxy formation proto-galaxies form in the central parts of over-dense regions of the universe, called dark matter halos. The study of the properties of dark matter halos such as their spatial distribution, mass and angular momentum, are the subject of the broader field of cosmology which immediately ties galaxy formation with the underlying large scale structure of the universe. The currently accepted standard cosmological paradigm is the Lambda-Cold Dark Matter (ΛCDM) cosmology (Springel et al., 2006). ΛCDM suggests that the universe comprises of 1) a cosmological constant Λ which gives rise to a 'dark energy' field that drives today's accelerated expansion of space, 2) cold dark matter, a non-relativistic, weakly interacting form of matter and 3) ordinary baryonic matter. According to the most recent measurements by the Planck satellite (Planck Collaboration, 2020) the energy density associated with the cosmological expansion has a value of $\Omega_\Lambda \approx 0.68$ whereas the mass density accounts $\Omega_m \approx 0.32$ out of which only 15% is in the form of baryonic matter and the rest constitutes the dark matter component. It is this $\sim$ 5% of the total mass of the universe that accounts for the stellar and gas light that we collect at all wavelengths of the electromagnetic spectrum and gives us the magnificent observations of galaxies (such as the spiral galaxy Fig. 1.2). However, the importance of the existence of the elusive 'dark matter' cannot be stressed enough with regards to providing the gravitational attraction required to initiate and subsequently regulate the process of galaxy formation.

Baryonic matter in the gaseous phase becomes confined to the bottom of the deep gravitational potential well which is produced by the dark matter overdensities. Infalling gas is initially shock heated to the virial temperature of the dark matter halos but for the gas to collapse to the centre of the well it needs to dissipate its internal energy and lose its pressure support. This happens via the process of radiative cooling, as pointed out by early seminal papers on galaxy formation (Rees & Ostriker, 1977; White & Rees, 1978). While infalling and because cooling is thought to be isotropic, the baryons are subject to the conservation of their angular momentum and they eventually settle to a disc like structure supported by rotation. It has been postulated for long that the specific angular momentum of the baryons (i.e. angular momentum divided by mass) is similar to that of the dark matter halo and this has been confirmed in simulation studies such as in van den Bosch et al. (2002).

The angular momentum of a galaxy is often characterized by the dimensionless spin parameter which is defined as [1]:

$$\lambda = \frac{J\,|E|^{1/2}}{GM^{5/2}} \tag{1.1}$$

where J is the angular momentum, M the mass and E the total energy of the galaxy (Peebles, 1971).

The question of how the gas settles in a disc and what determines the subsequent size of the system has been theorised by early work by Fall & Efstathiou (1980) and further explored by Mo et al. (1998). Following the derivation in Mo, Van Den Bosch & White (Mo et al., 2010) we can show how a realistic self-gravitating disc is formed inside a dark matter halo. If the dark matter halo follow a density profile

$$\rho(r) = \frac{1}{4\pi r^2}\frac{dM(r)}{dr} \tag{1.2}$$

the energy of the halo is:

$$E = -\frac{M_{\rm vir}V_{\rm vir}^2}{2}F_E \tag{1.3}$$

where $M_{\rm vir}$ is the virial mass, $V_{\rm vir}$ the virial velocity and the factor F_E depends on the form of the density profile. Under the assumptions that the baryons have the same specific angular momentum as the dark matter and that orbits are exactly circular then the disc has angular momentum given by:

$$J_d = 2M_d R_d V_{vir} F_R \tag{1.4}$$

where the subscript d refers to disc properties and $F_R = 0.5\int_0^{r_{vir}/R_d} u^2 e^{-u}\frac{V_c(uR_d)}{V_{vir}}du$, with $V_c(r)$ being the circular velocity. Substituting Eq. 1.3 into Eq. 1.1 yields the relation for the disc radius:

$$R_d = \frac{1}{\sqrt{2}}(\frac{j_d}{m_d})\lambda r_{vir} F_R^{-1} F_E^{-1/2} \tag{1.5}$$

where $j_d = J_d/J_{vir}$ is the specific angular momentum of the disc.

Once the gas in the disc becomes sufficiently cold and dense, star formation can occur, building a stellar component in the disc that evolves in parallel with the gas. It must be noted that the gas and stars follow different dynamics; gas behaves as collisional fluid subject to many energy dissipation processes whereas stars act like a collisionless fluid, i.e. the relaxation time of the stellar disc is much larger than the age of the universe. Moreover the typical velocity dispersion

---

[1] The same expression is used for the spin of a dark matter halo

of the gas component is around ~10 km s^{-1} while the stellar discs have usually much higher values of ~40 km s^{-1}.

1.2.1 Stellar component

Figure 1.2: Optical image of the spiral galaxy Messier 101 which nicely illustrates the extended disc with the significant presence of spiral arms. In this image one can observe that at the location of the spiral arms there is predominantly blue color, an indication of young stellar populations, and brown stripes of material which is dust in the interstellar medium. On the contrary the reddish hues in the center of the disc are a sign of older stars. Credits: Hubble Image: NASA, ESA, K. Kuntz (JHU), F. Bresolin (University of Hawaii), J. Trauger (Jet Propulsion Lab), J. Mould (NOAO), Y.-H. Chu (University of Illinois, Urbana) and STScI;

The stellar mass of a spiral galaxy is distributed between four main components.

1. Central Bulge
2. Thin disc
3. Thick disc
4. Stellar halo

The bulge is a concentration of stars at the central regions of many galaxies. Contrasting to the nearly circular orbits of the disc stars, those in the bulge have more random motions resulting in high velocity dispersion in that region of the galaxy. In addition bulge stars are on average older and richer in metals. Bulges fall into two categories depending on their formation mechanism, a) true bulges and b) pseudo-bulges. The former result from galaxy merger events whereas the latter are related to the secular evolution of the disc and form likely from instabilities (discussed further in a following section). The surface brightness of the bulge component of a galaxy is usually modeled by a Sercić profile $I_b(r) = I_b \exp(-\beta_n (R/R_b)^{1/n})$, where n denotes the Sercić index. This expression with $n = 4$ is also used as fit to the surface brightness profiles of elliptical galaxies (de Vaucouleurs's law).

The thin disc is the main component associated with a spiral galaxy. It contains young stars that rotate in a narrow plane while star formation is still active in it, especially around the spiral arms. Observational evidence suggests that the stellar discs follow a surface brightness radial profile of exponential form $I(r) = I_d \exp(-R/R_d)$, where R_d is the scale radius. The exact mechanisms that lead to the formation of exponential discs are not clear. Some of the suggested theories are that the exponential profile is shaped by the specific angular momentum distribution of the early proto-galaxy, the viscosity in the disc, or the supernova outflows removing low angular momentum gas from the disc (Dutton, 2009; Mo et al., 2010).

Despite the term 'thin disc', all discs have a vertical extent which is usually modeled by a function of the form $\mathrm{sech}^{2/n}(\frac{nz}{2z_d})$ where z_d is the vertical scale height. The $n = 1$ case corresponds to the equilibrium structure of a an isothermal infinite sheet. Thin discs are subject to heating mechanisms which increase the velocity dispersion of their stars. Stars formed near the mid-plane of the disc with low velocity dispersion move to larger scale-heights as they are heated, resulting in the observed vertical profiles. There are various proposals for these mechanisms in the literature such as the interactions and mergers with satellites or the scattering of stars against massive clouds of gas in the disc.

The thick disc appears as a separate component to the thin disc both in terms of kinematics and chemical content of its stars. In particular, thick disc stars are found to be older, more metal poor and more enriched in α elements compared to thin disc stars. In addition the thick disc is kinematically hotter and appears more diffuse, extending to larger scale heights but having roughly the same radial extent as the thin disc. The formation of the thick disc and the origin of thick disc stars is a matter of debate. Thick disc stars could 1) be thin disc stars that have been kinematically heated, 2) have formed in-situ as part of the thick disc in a star-formation episode in the early phases of the galaxy formation or, 3) have formed in external systems such as small merging satellites.

Finally, the galactic halo constitutes a component of much lower density that surrounds the disc at much larger scaleheights. The stellar population in the halo has kinematically hot orbits, older ages and low metallicities. The stellar halo of the Milky Way contains a wealth of globular clusters and remnants of merger events in the form of elongated stellar streams. The recent review by Helmi (2020) is excellent material for more discussion on the stellar halo as well as the thick disc component of our Milky Way.

Milky Way

Our own Milky Way is a typical spiral galaxy. Because of our position within it, considerable research has been carried out concerning its history, formation and evolution which can also give an indication to how spiral galaxies have evolved more generally in the universe. Indeed most theoretical works on disc galaxies (simulations and analytic models) aim to reproduce the well constrained characteristics of our galaxy. In terms of its structural characteristics, the Milky Way's disc has a scale length of of $\sim$ 3 kpc and $\sim$ 3.3 kpc for its thin and thick disc respectively (McMillan, 2011) while the vertical scaleheight of its thick disc is roughly three times larger than its thin disc (0.9 vs 0.3 kpc) according to Jurić et al. (2008). Observations have shown that in addition to four spiral arms (Georgelin & Georgelin, 1976; Vallée, 2014), the Milky Way is a barred spiral galaxy with a peanut-shaped bar (Wegg & Gerhard, 2013). Furthermore, it is now firmly established that it harbours a central supermassive black hole with mass $\sim 4 \times 10^6 M_\odot$ (Genzel et al., 2010). Recently the most significant advances in Milky Way research are being made by the GAIA survey (Gaia Collaboration, 2016) which has mapped with unprecedented precision the positions and properties of $\sim$ 1.5 billion stars in the latest data release (Gaia Collaboration, 2021). The purpose of such large scale surveys is to disentangle the history of Milky Way's formation by studying both the kinematics and chemical content of the stars in order to determine their origins and how their orbital characteristics have changed over the course of Milky Way's lifetime.

1.2.2 Gas component

Spiral galaxies are gas rich systems with most of the gas being in the molecular (H_2) and neutral (HI) hydrogen phases (contrasting with the mostly ionised gas in ellipticals). Similarly to the stars the gas in the disc moves in an ordered rotation, in mostly circular orbits and in a relatively narrow plane. The neutral hydrogen extends radially to larger distances compared to the stellar disc but most of the molecular hydrogen distribution follows that of the stellar component. Observationally these gas motions can be traced by the strong emission line produced by the spin-flip transition of neutral hydrogen at the wavelength of 21cm. These observations are available at very large distances and are extremely useful in studying the dynamics of the galaxy and constructing the rotation curves of the disc, i.e. the mean rotational velocity at any given galactocentric radius. For most spiral galaxies the rotation curve reaches values in the range of 150-300 km s^{-1} and then flattens around these values at the outer regions. The rotation curve can give us a measurement of the total mass enclosed within a radius by simply invoking the relation $M(< r) = rv_{rot}^2/G$ from gravitation theory. The observed flat rotation curves and the absence of a Keplerian fall-off were instrumental for postulating the presence of an additional 'dark' component of mass.

Motivated by the discussion of the rotational velocity measurements being obtained from the gas in the disc, we mention here, as an aside, that a well-established correlation exists between the rotational velocity and the luminosity of a spiral galaxy a finding called the Tully-Fischer relation (Tully & Fisher, 1977).

$$L \propto V_{rot}^a \tag{1.6}$$

The Tully-Fischer relation has an important physical implication because it directly links a property of the baryonic component of the galaxy (luminosity) with the rotational velocity which is largely determined by the mass of the dark matter halo, thus pointing out the co-evolution of galaxies and the dark matter haloes within which they reside.

The molecular gas is harder to observe directly and most studies use other molecular tracers, such as carbon monoxide (CO) in order to infer its mass. Nevertheless the existence of H_2 is of utmost importance since it forms dense clouds that become sites for the formation of stars.

The gas that is consumed from star formation is replenished by new gas that is accreted onto the disc. In the literature there are two gas accretion mechanisms that are discussed, a 'hot mode' accretion where gas is shock heated at the virial radius of the halo and slowly settles onto the disc (White & Rees, 1978) and a 'cold mode' accretion where gas is directly funneled onto the disc by filaments (e.g. Kereš et al., 2005).

The gaseous component is continuously stirred by turbulence which is sourced by a number of mechanisms (Elmegreen & Scalo, 2004). These include the energy expelled from the supernovae and stellar winds, infall of new gas, interactions with satellite galaxies, magnetic fields and even the presence of spiral arms.

1.2.3 Orbits

In this thesis we are concerned with the motions of stars and gas within the galactic plane so it is essential to outline how material orbits under the effect of gravity in the disc. The central regions of a dark matter halo, that are populated with baryons, are dominated by the gravitational potential that is generated by the galaxy. An axisymmetric potential is a good approximation in particular for a disc galaxy because of its ordered rotation around a preferred axis.

The motion of a particle under the effect of an underlying gravitational potential Φ is described by Newtons's equation of motion:

$$\frac{d^2\mathbf{r}}{dt^2} = -\nabla\Phi \tag{1.7}$$

Considering the symmetry of a galactic disc it is natural to solve this equation using cylindrical coordinates (R, ϕ, z). In that case an equation of motion is obtained for each coordinate:

$$\frac{d^2R}{dt^2} - R\left(\frac{d\phi}{dt}\right)^2 = -\frac{\partial\Phi}{\partial R} \tag{1.8}$$

$$\frac{d}{dt}\left(R^2\frac{d\phi}{dt}\right) = 0 \tag{1.9}$$

$$\frac{d^2z}{dt^2} = -\frac{\partial\Phi}{\partial z} \tag{1.10}$$

Eq. 1.9 denotes the conservation of the term in the brackets which can be identified as the angular momentum in the perpendicular direction to the plane, z, $L_z = \left(R^2\frac{d\phi}{dt}\right)$.

Using this conserved quantity it is useful to define the effective potential $\Phi_{\rm eff}(R, z) = \Phi(R, z) + (L_z^2/2R^2)$ and express the equations of motion for the two remaining coordinates in terms of it as:

$$\frac{d^2R}{dt^2} = -\frac{\partial\Phi_{\rm eff}}{\partial R}, \quad \frac{d^2z}{dt^2} = -\frac{\partial\Phi_{\rm eff}}{\partial z} \tag{1.11}$$

Important quantities derive from these equations and are widely used in literature in galactic dynamics. The *guiding centre*, R_g, is the minimum of the effective potential, $\frac{\partial\Phi_{eff}}{\partial R}(R_g, z) = 0$. The guiding centre corresponds to the radius of a circular orbit with energy equal to the effective potential. Associated with this orbit is the circular frequency $\Omega(R) = \frac{V_c(R)}{R} = \frac{L_z}{R^2}$

The epicyclic frequency, κ, is the second derivative of the effective potential $\kappa^2 = \frac{\partial\Phi_{eff}}{\partial R^2}$ evaluated at the guiding centre. In the epicyclic approximation where higher than second order terms are excluded it reduces to a relation that connects κ to the circular frequency Ω:

$$\kappa = \left(R\frac{d\Omega^2}{dR} + 4\Omega\right)^{1/2} \tag{1.12}$$

All in all the motion of a star in the frame of the disc is, in general, a rosette, described by a circular motion at a mean radius (guiding centre) on which smaller radial oscillations around the guiding radius are superimposed, called epicycles.

1.2.4 Disc stability

Another useful concept in understanding galactic discs is that of their stability against gravitational collapse. Disc instabilities can occur both in a global and local fashion.

Local instabilities happen on scales much smaller than the disc size such as for example the gravitational collapse of a cloud of gas that can lead to th formation of stars.

Toomre (1964) introduced the dimensionless parameter Q to determine the local stability of a disc. For a gaseous disc this parameter is defined as:

$$Q = \frac{\kappa c_s}{\pi G\Sigma} \tag{1.13}$$

where κ is the epicyclic frequency, c_s the speed of sound and Σ is the surface density of the disc. The corresponding equation for the stellar component is:

$$Q = \frac{\kappa\sigma_r}{3.36G\Sigma} \tag{1.14}$$

where σ_r is the radial velocity dispersion of the stars.

In either case the local stability criterion requires $Q > 1$ whereas $Q \leq 1$ in gaseous discs will lead to fragmentation into smaller clumps.

The physical interpretation of the above equations is that some sort of internal pressure (numerator) in the disc is required in order to counteract gravity (denominator). Depending on whether we are concerned about the gaseous or stellar disc this internal pressure can result from the kinetic energy of either the gas particles or the stars that form the disc, expressed by the sound speed and the velocity dispersion respectively.

Global instabilities have an effect on the whole disc and can lead to structural changes, such as the formation of a bar (bar instability). Efstathiou et al. (1982) suggested that the disc becomes stable against the bar instability if it is embedded in a dark matter halo since the additional dark matter mass increases the rotation velocity and provides support against gravitational collapse. However it has also been argued that the presence of a dense mass concentration at the galactic centre, such as a bulge, can also contribute as a stabilizing mechanism (Sellwood & Moore, 1999; Sellwood & Evans, 2001).

1.2.5 Non-axisymmetries in disc galaxies

As discussed in section 1.1 the properties of the spiral arms and the presence of a bar are central in classifying spiral galaxies. Besides the morphological aspect, these so-called **non-axisymmetric** features have a profound effect on the evolution of a galaxy and their formation mechanism is a matter of intense research. Such non-axisymmetries are particularly relevant in this thesis since they are main sources of torque to the surrounding material which in turn can cause changes to the orbital properties of both the gaseous and stellar components of the disc.

Spiral arms are transient structures in the disc and are associated with enhanced star formation activity. A spiral arm is fundamentally a density perturbation of the disc that manifests itself both in the gas and stellar component. One theory for the formation of spiral arms is the 'spiral density waves theory' (originally introduced in Lin & Shu (1964)). It suggests that spiral arms are created by stationary spiral-like density waves propagating in the plane of the disc and rotating with a defined pattern speed. Gas and stars move in and out of the wave congesting in the enhanced density regions. However, this hypothesis has been challenged on the basis that the density waves that form the spiral arms are not stationary (Binney & Tremaine, 2008).

Bars are elongated structures that are found in the centres of spiral galaxies. According to Sheth et al. (2008) 65% of the spiral galaxies in their sample have a bar at $z = 0$ but that number declines down to 20% for higher redshift ($z \sim 0.85$) while bars are found in both massive spiral galaxies like our own Milky Way as well as in the smaller dwarf galaxies such as the Large Magellanic Cloud. As mentioned before, the formation of a bar is thought to happen because of a global instability in the disc. Bars are rotating structures that, unlike the differential rotation of the surrounding disc, follow a solid-body rotation with an angular speed that is called bar pattern speed Ω_b.

This specific frequency acts as a forcing frequency that creates resonances in the disc which interact with the stellar orbits when crossing them. The most important of these resonances are the **corotation resonance (CR)** where the angular frequency of the stellar orbit at the guiding centre (Ω_0) equals the bar pattern speed:

$$\Omega_0 = \Omega_b \quad \text{for corotation resonance} \tag{1.15}$$

and the **Lindblad resonances** which occur where:

$$m(\Omega_0 - \Omega_b) = \pm\kappa_0 \quad \text{for Lindblad resonance} \tag{1.16}$$

where m is an integer. The plus sign corresponds to the **inner Lindblad resonance (ILR)** where the star moves faster and overtakes the pattern speed whereas the minus sign refers to the **outer Lindblad resonance (OLR)** where the star lags behind the forcing (Binney & Tremaine,

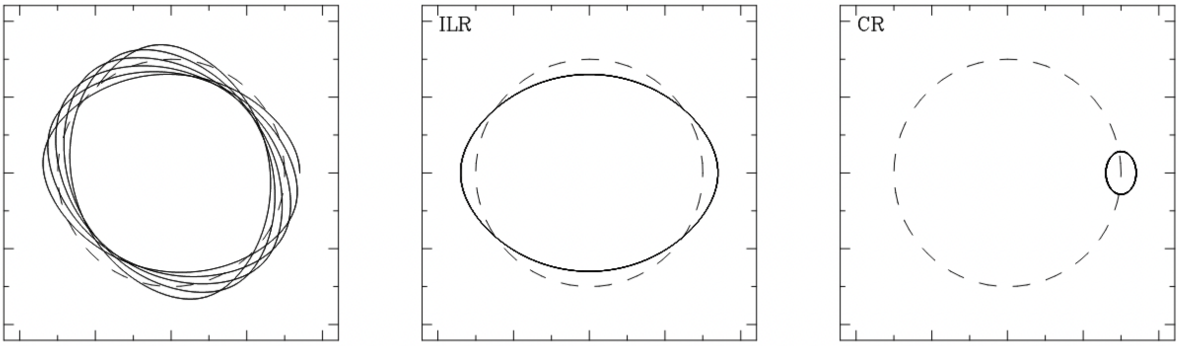

Figure 1.3: Examples of a non-resonant epicyclic orbit (left panel) and epicyclic orbits trapped at the Inner Lindblad (middle) and corotation (right) resonances. The circular dashed line is the guiding radius. Adapted from Athanassoula (2013).

2008) [3]. Resonances are of critical importance for the redistribution of material within the disc because it is where exchange of angular momentum happens more efficiently. In particular angular momentum is thought to be gained at the ILR and absorbed at the OLR (Lynden-Bell & Kalnajs, 1972; Athanassoula, 2013). Moreover in barred galaxies there is significant radial transport of material around the corotation radius where strong torques are exerted resulting in material within the CR moving outwards and material outside the CR being pushed inwards.

1.2.6 Chemical content

In addition to its dynamical properties, a galaxy is also characterized by its chemical properties. The latter are useful indicators of the evolution of the system and can help in identifying the star formation as well as merger histories. The most common measure of the chemical composition of a galaxy is the metallicity, i.e. its mass in metals compared to its total baryonic mass. In the astrophysical context metals refer to any element other than hydrogen (H) and Helium (He) therefore the metallicity in the simplest form is defined as:

$$Z = \frac{M_{\text{metals}}}{M_{\text{tot,baryons}}} \tag{1.17}$$

A well-known scaling relation in disc galaxies is that between their mean gas phase metallicity and luminosity which because of the mass-luminosity proportionality yields also a relation between the stellar mass and metallicity (Tremonti et al., 2004).

Furthermore, additional information is obtained from the abundances of individual elements, which are usually expressed as a ratio of the specific element number density with respect to the mass in hydrogen. Such abundance ratios can be used as indicators of the total metallicity which is much harder to measure observationally since many different elements need to be traced in the

---

[3] The same resonances are created by the pattern speed of the spiral arms

spectra of the galaxies. The most useful tracer of the gas metallicity is the abundance in oxygen, which is by convention expressed as the scaled ratio:

$$12 + \log(\mathrm{O/H}) \equiv 12 + \log(n_O/n_H) \tag{1.18}$$

When measuring the stellar metallicity a more commonly used option is the iron abundance owing to the importance of iron in stellar evolution as well as the strong lines that produces in spectra of individual stars and galaxies. The iron abundance is usually normalised by the solar values:

$$[\mathrm{Fe/H}] = \log\left(\frac{n_{\mathrm{Fe}}/n_{\odot}}{n_H/n_{\odot}}\right) \tag{1.19}$$

Another useful chemical tracer regarding the evolution of a galaxy is the ratio of their content in alpha elements to iron, [α/Fe], called *alpha enhancement*. Alpha elements refers to those elements that consist of nucleons in multiples of four, the most important being example oxygen (O) but also neon (Ne), magnesium (Mg), silicon (Si), calcium (Ca) and sulfur (S). These elements are byproducts of type two supernovae (SNe-II) by massive stars that happen on short timescales. Therefore a high presence of alpha elements in a galaxy signifies a rapid formation of their stellar mass. On the other hand when there is increased presence of iron, that is produced over longer timescales predominantly in type Ia supernovae (SNe-Ia), it is an indication of more time extended star formation.

Besides the global metallicity, a most interesting question is the radial metallicity profiles or equivalently whether there are metallicity gradients in discs. In a standard scenario of inside-out formation of a galactic disc the inner regions will have older stars and gas that has been chemically enriched by previous supernovae events. On the other hand the outskirts of the disc are fueled with unprocessed, low metallicity gas which will form stars that are also less chemically enriched. Therefore it is expected that metallicity will decrease monotonically with radius creating a negative radial gradient. The observations of galaxies with very flat gradients or even a reversed (i.e. positive) gradient at the outer regions thus strongly point to the fact that throughout the evolution of the disc there is exchange of material between different radii. Examples for this would be the flow of gas towards inner regions or the transport of chemically rich stars from the more central regions to the outside. Such processes are the core subject of this thesis as discussed in the following subsection.

1.2.7 Radial motions of material

There are a number of physical mechanisms that can induce radial flows of gas within the disc. Lin & Pringle (1987), for example, explore the effect of the viscosity of the disc in instigating radial transport of the gas and eventually leading to the observed exponential profiles of galactic discs. In addition, the presence of a bar in the centre of the disc is often associated with inflowing streams of gas on either end of the elongated bar structure. Spiral arms can similarly to the bar apply torques that can alter the gas's angular momentum and result in it moving inwards or outwards (Sellwood & Binney, 2002). Mergers or interactions with smaller satellite galaxies can also cause gas to flow inwards. These radial flows of gas are extremely important in the evolution of the galaxy because a) the location of the gas dictates where star formation is happening b) inflowing gas towards the centre can end up in the central black hole, triggering an active galactic nucleus (AGN) c) there can be considerable mixing of newly inflowing gas to the existing ISM, hence altering the metallicity profiles that are observed.

Stars, during their lifetime, are also subject to changes in their radial position which has been termed 'stellar migration'. Stellar migration is caused by changes in the orbital angular momentum of the stars that lead to changes in the mean orbital radius, the guiding centre. If by some mechanism the star gains angular momentum then it moves to an orbit with a larger radius and vice versa loss of angular momentum leads to the star orbiting at a smaller radius. Similar to the gas it is the presence of spiral arms or a bar that primarily causes these changes to the angular momentum that lead to migration (Minchev & Famaey, 2010; Sellwood & Binney, 2002). Stellar migration is thought to be a process that also contributes to the shaping of metallicity gradients of disc galaxies and the mixing of younger/metal-rich and older/metal-poor stellar populations at different radii within the galaxy. We discuss more extensively about radial migration in the introductory section of Chapter 3.

1.3 Numerical simulations of galaxy formation and evolution

The scales and energies involved in astrophysical processes make it impossible to conduct experiments to study these phenomena in laboratory conditions in the same way as in other fields of physics. Hence, astrophysicists resort to computational modelling, that is combining their knowledge of the physics involved in the universe's evolution with sophisticated numerical algorithms in order to simulate whole regions of the universe, individual galaxies, parts of galaxies or even individual stars in a controlled environment in a computer. Upon years of constant development these so called 'numerical simulations' have proven to be the most powerful theoretical tools through which astrophysicists can test the validity of their theories by comparing their simulated output against real astrophysical observations.

In this thesis we focus on simulations that study the formation and evolution of galaxies. Such simulations are primarily hydrodynamical simulations meaning that one solves both the gravitational equations for all the collisionless components of a galaxy (stars and dark matter) and the hydrodynamical and radiation equations that govern the dynamics of gas.

All mass components in a simulation interact via gravitational forces, the computation of which requires knowledge of the gravitational potential at any point of space. The potential is created by the underlying density distribution and is described by the Poisson equation:

$$\nabla^2\Phi = 4\pi G\rho \tag{1.20}$$

Once Φ is computed, the forces (or accelerations) on the particles are given by the simple equation of motion: $\mathbf{a} = -\nabla\Phi$. Knowing the accelerations, the velocities and positions of the particles can then be updated. There are numerous numerical algorithms that are used to integrate the equations of motion, however discussion on them is beyond the scope of this chapter and we refer to useful summary reviews such as Springel (2016).

The dynamics of the gas is dictated by the three Euler equations which describe the conservation of mass, momentum and energy of the fluid and can be written as: [2]

$$\frac{\partial \rho}{\partial t} + \nabla(\rho \mathbf{v}) = 0, \tag{1.21}$$

$$\frac{\partial (\rho \mathbf{v})}{\partial t} + \nabla(\rho \mathbf{v}\mathbf{v}^T + P) = 0, \tag{1.22}$$

$$\frac{\partial (\rho \epsilon)}{\partial t} + \nabla[(\rho \epsilon + P)\mathbf{v}] = 0, \tag{1.23}$$

where ρ is the density, P the pressure, $\mathbf{v}$ the velocity vector and ϵ the total energy per unit mass. The above equations describe an ideal fluid and can be transformed to the Navier-Stokes equations for real fluids when a viscosity term is added on the right-hand sides of Eq. 1.22 and 1.23.

Different codes are using different algorithms in order to solve the hydordynamical equations but most fall in one of the two most prevalent methods which are 1) the smoothed-particle hydrodynamics (SPH) codes and 2) grid-based codes.

The former use a Lagrangian approach and the fluid is simulated by particles that sample the mass. Translating the discrete distribution of the point particles to a continuum requires the use of a kernel function which describes how the mass of each particle is distributed to the surrounding space. So in SPH the fields, ($F(\mathbf{r})$) related to the particles, such as the density, are represented as a convolution of the field with a kernel function.

$$F_s(\mathbf{r}) = \int F(\mathbf{r}')W(\mathbf{r} - \mathbf{r}', h)d\mathbf{r}' \tag{1.24}$$

Grid-based codes on the other hand solve the equation of the hydrodynamics in a -usually Cartesian- grid of fixed points. This is the Eulerian approach. The equations of hydrodynamics are solved across the faces of the 3D cells of the grid and the fluxes from one cell to another are computed as a result. Because of the varying scales of the astrophysical phenomena an adaptive mesh is commonly utilised. That is to say the size of the cells is reduced in regions of higher density achieving higher spatial resolution.

Each of these methods has its specific shortcomings; SPH for example suffers from poor resolution of shock discontinuities and a suppression of fluid instabilities whereas mesh codes show no Galilean invariance and exhibit a tendency for prefered spatial directions (Springel, 2016).

Recent advanced codes such as AREPO (Springel, 2010; Pakmor et al., 2016; Weinberger et al., 2020) are combining the advantages of each of the aforementioned methods by solving the hydrodynamics equations on a moving mesh. That is to say the cells that constitute the fluid mass are dynamically changing in shape and size following the underlying flow of the gas. AREPO in

---

[2] This is the *Eulerian* form of the Euler equations. There is also the *Lagrangian* representation of these equations, describing the same dynamics from a different frame of reference and with a different notation

particular uses a Voronoi tessellation of the space to compute the sizes and shapes of the cells. Similar to the grid codes, moving-mesh codes are computing the fluxes across the cell faces.

A fundamental problem of all galaxy formation simulations is the fact that different processes work on very different length scales and densities. In order to simulate very high densities it is necessary to increase significantly the resolution of the simulation, by including more particles (in SPH) or more cells (in grid codes) but in either case, as mentioned before, the computational cost is prohibitive and each simulation has a certain resolution limit. Processes that fall below the resolution limit need to be modelled with a sub-grid prescription. These are theoretically or observationally motivated recipes that aim to approximate the phenomena. Some of the most important evolutionary processes in galaxies in need of a sub-grid treatment are the star formation and stellar and AGN feedback. There is variety of feedback recipes which differ mainly on the fashion in which the energy is coupled to the surrounding medium.

Apart from the code that is used, galaxy simulations differ in their box size and resolution, and depending on the science goals of each project a different type of simulation is employed.

The first category are the ’cosmological simulations’, which aim to reproduce a relatively large region of the universe and millions of galaxies over all mass scales. Such simulations include IllustrisTNG (Nelson et al., 2018; Pillepich et al., 2018; Springel et al., 2018), EAGLE (Schaye et al., 2015), Magneticum (Hirschmann et al., 2014), SIMBA (Davé et al., 2019) and Horizon-AGN (Dubois et al., 2014). The large number of galaxies in these simulations can be used to extract statistically robust conclusions for the galaxy population. However, large simulated volume cannot be easily combined with very fine mass resolution due to the immense computational expenses. Recent advances in computational power and the invention of more efficient algorithms have expanded the limits of those simulations achieving high resolution in a relatively large box (Nelson et al., 2019).

The second type are the ’zoom-in’ simulations. These simulations are performed by extracting a particular region from a parent dark-matter-only simulation and re-simulating this part of the universe with much higher resolution. The advantage of zoom-in simulations in galaxy formation is that they combine relatively high resolution (comparing to cosmological simulations) while the simulated galaxy is fully embedded in a cosmological environment. Hence, the very crucial process of gas accretion from the circum-galactic medium (CGM) is included in the simulation. Examples of suites of zoom-in simulations of galaxies include Auriga (Grand et al., 2017), FIRE-2 (Hopkins et al., 2018) and NIHAO (Wang et al., 2015).

The last type are simulations of isolated galaxies. In this approach, the focus is on reproducing single galaxies in controlled conditions without the effect of their surroundings. These simulations are ideal for studying secular processes in the discs of galaxies such as the development of bar (e.g. Fanali et al., 2015) and spiral structures, radial migration of stars (e.g. Kubryk et al., 2013) or the effect of stellar feedback on the interstellar medium of the galaxies. Moreover, mergers of two or more galaxies can be studied in an isolated environment with great control over the mass ratios and incidence angle of the merger (e.g. Naab & Burkert, 2003). However, in contrast to the ’zoom-in’ simulations effects from the interaction of the galaxy with the circum-galactic medium are excluded. The review by Vogelsberger et al. (2020) offers a comprehensive summary of these simulation types and their design techniques.

It is interesting to note that early numerical simulations of individual disc galaxies suffered from what is called 'angular momentum catastrophe' (Navarro & Benz, 1991). In those simulations the gas that was infalling into dark matter halos during mergers was losing angular momentum to the surrounding dark matter via the dynamical friction mechanism, a process that is intensified when the gas is falling in as clumps rather than with a smooth distribution. Because of the loss of angular momentum the resulting discs were too small in size and could not reproduce the extended gas distribution that we observe in real objects. This issue has been alleviated in modern simulations (Grand et al., 2017) owing to the realisation that the injection of some sort of thermal energy in the baryons of the infalling galaxy is needed in order to counteract the gravitational collapse of the gas into clumps and limit the effect of the dynamical friction and loss of angular momentum. Such heat-injection mechanisms include the supernova explosions of massive stars and the activity of a central black hole. Another possible contributing factor to angular momentum losses could be the numerical implementation of the simulation (Mayer et al., 2008).

1.4 Semi-Analytic models of galaxy formation and evolution

An alternative approach to the modelling of galaxy evolution is the use of Semi-Analytic Models (SAMs). These models offer a much more simplified approach compared to the full numerical simulations, which were discussed before, since the complex hydrodynamical equations are not solved exactly. Instead, several physical processes are modelled with simple, but physically motivated, recipes/prescriptions which are governed by a set of free parameters. This leads to the main advantage of SAMs over numerical simulations which is the fact that many different realisations of the universe can be simulated in considerably faster and in a less computationally expensive manner by simply altering and tuning the free parameters.

Dark matter halo merger trees are used as the backbone of semi-analytic models by providing the properties of the halos (such as mass, spin etc.) on top of which the galaxy properties are approximated using the recipes of the model. Initial semi-analytic models were using theoretically computed trees arising from the extended Press-Schechter formalism (Press & Schechter, 1974). However, in recent years most models are built using halo trees extracted from large scale dark-matter-only cosmological simulations, such as the Millennium simulation (Springel et al., 2005).

Several groups of researchers have developed versions of semi-analytic models. Some of the best known models include L-Galaxies (Henriques et al., 2020; Springel et al., 2001), GALFORM (Lacey et al., 2016), the Santa-Cruz model (Somerville et al., 2008) and SAGA (Croton et al., 2016). Despite the many differences in the choice of the recipes and the free parameters, all semi-analytic models follow a similar pathway to populate the dark matter halos with galaxies and subsequently evolve these galaxies in time. In brief, hot/non-star forming gas is assigned to each halo based on the cosmic baryon fraction. A fraction of the hot gas is allowed to cool, using a cooling recipe, which turns into the cold-star forming gas that most closely models a galaxy. Based on a star formation prescription cold gas is turned into stars while usually stellar and AGN feedback are modelled as an energy input to the gas that decreases the cooling rate. Furthermore, galaxies can merge following the merger trees of their dark matter halos and a recipe based on dynamical friction principles needs to be introduced to determine how much the baryonic merger lags behind the dark matter halo merger. Recent advances in SAMs also include tidal stripping of satellite galaxies and detailed analysis of the chemical evolution by tracking a number of elements and metals.

Semi-analytic models aim to reproduce observables that are central for in the understanding of galaxy evolution such as the galaxy mass function, the black hole - stellar bulge relation or the color dichotomy between star forming and non-star forming galaxies.

We discuss in greater detail the structure and the several recipes of the L-Galaxies semi-analytic model in Chapter 4.

1.5 Chemodynamical models of disc galaxies

Semi-analytic models study the galaxy evolution in a holistic approach, trying to simulate a range of different galaxies and physical processes. Another type of theoretical models, called chemodynamical models, bear great resemblance to the semi-analytic approach but are more focused on the chemical evolution of disc galaxies with a particular emphasis on trying to replicate the properties of our own Milky Way (Schönrich & Binney, 2009; Kubryk et al., 2015). For example, chemodynamical models aim to reproduce the metallicity distribution and metallicity gradients observed in Milky Way discs as well as the ages and velocity dispersion of the stars.

In most chemodynamical models the disc of the galaxy is decomposed in a series of concentric rings. This ring decomposition allows for information about the radial profiles of the studied properties to be obtained that can be directly compared with observations. Initially the rings contain low (or zero) metallicity gas. For example, in the model by Schönrich & Binney (2009) the rings are populated with cold ($\sim$ 30K) and warm ($\sim 10^4$K) gas of which only the former is available for star formation. As the processes of star formation and stellar evolution proceed, this gas is enriched with metals that are expelled during the stellar evolution. Moreover new gas is allowed to accrete with a given radial profile onto each ring. The rings in the models evolve in an independent fashion, however there can be exchanges of material between different rings in the form of radial flows of gas and migration of stars. Schönrich & Binney (2009) in particular employed two mechanisms that redistribute mass between the rings, which they termed ’churning’ and ’blurring’, a nomenclature that has prevailed in the literature in studies of stellar migration. ’Churning’ applies to both the cold gas component and the stars and refers to the exchange of angular momentum between non-axisymmetries in the disc and these components. In the ’churning’ process there is a change in the angular momentum of the affected material but no change in the eccentricity of the orbit. In this model the ’churning’ probability, that is the probability that a star or gas particle moves from ring i to ring j is given by:

$$p_{ij} = \begin{cases} k_{ch} M_j / M_{\max}, & \text{for } j = i \pm 1 \\ 0, & \text{otherwise} \end{cases} \tag{1.25}$$

where k_{ch} is a free parameter, and $M_{\max} = \max(M_j)$.

The process of ’blurring’, which refers only to the stellar component, is the result of changes in the amplitude of the oscillations around the guiding centre of the stellar orbit. Schönrich & Binney (2009) present their application of the 'blurring' with a rigorous mathematical formulation, that is not necessary to repeat in this section, and they obtain a probability distribution for the radius of a star with a given angular momentum L. We return to a discussion of these two processes in the introductory part of Chapter 3.

1.6 Outline of the thesis

The goal of this thesis is to study the radial transport of mass within the plane of disc galaxies. Whereas it is established that both radial flows of gas and the change of orbital properties of stars happen during the lifetime of a galaxy, their importance for the overall evolution is still not well constrained. The semi-analytic and chemodynamical models, mentioned above, have mostly approached the modelling of these processes from a purely theoretical/first principles standpoint. Moreover, in numerical simulations there is limited exploration of the stellar migration and radial gas flows compared to other physical processes such as the stellar and AGN feedback and on top of that a quantitative description is usually lacking. In this thesis we look at this relatively unexplored topic of theoretical astrophysics and aim to constrain the two processes using a state of the art numerical simulation as well as one of the most advanced semi-analytic models.

We use a set of simulated galaxies from the Auriga suite of cosmological 'zoom-in' simulations. In Chapter 2 we present an analysis of the radial gas flows in a selection of these galaxies, we provide a parametrization that describes these radial flows and we discuss several physical processes that can induce or influence the radial transport of gas. Material from this chapter was published in Okalidis et al. (2021). In Chapter 3 we focus on the stellar component in our simulations and in particular study the radial migration of stars during their lifetime. We analyse the effect of stellar migration on the metallicity and age profiles of the disc and arrive in a parametrized form that quantifies the strength of migration as a function of radius and time. Material from this chapter was published in Okalidis et al. (2022). In Chapter 4 we present a preliminary application of the aforementioned parametrizations in the L-Galaxies semi-analytic model. We explore the effect of our implementation in a simple toy model as well as in the output of the full scale L-Galaxies model. Finally, in Chapter 5 we provide a summary of the findings of this work and the future paths of research that arise from it.

Chapter 2

Radial gas flows in the Auriga simulations

2.1 Introduction

Examining the kinematics and flow of gas within the disc can give us useful insights into some key aspects of the disc evolution. Gas inflowing through the disc plane is directed to the central regions, fuelling star formation. Furthermore, radial flows result in mixing of metal poor gas accreted in the outer regions of the disc with more metal-enriched gas due to the stellar evolution in the plane and can influence the metallicity gradients we observe in disc galaxies (Spitoni & Matteucci, 2011; Schönrich & McMillan, 2017; Yates et al., 2021). Similarly, the redistribution of gas due to these flows determines the locations of star formation hence influences the star-formation rate (SFR), stellar and gas density profiles.

There have been studies of, and recent interest in, how gas flows across the virial radius of dark matter (DM) haloes (e.g. Nelson et al. 2015) and eventually reaches the central galaxy. However, in the field of numerical simulations there are relatively fewer studies concerning how gas flows in the plane of the disc affect the galaxies within these haloes.

Therefore, in this study, we focus on the path of the gas inside the galactic disc. The gas that is in place in the disc along with the newly accreted gas (Stevens et al., 2017), are subject to angular momentum loses, resulting in infalls towards the centre of the potential well, while following the rotational pattern of the galaxy. The collisional nature of the gas means that turbulent behaviour can become important, while the gas is also subject to external torques from surrounding subhalos or non-axisymmetric structures such as bars.

Radial gas flows have been studied in early work by Lacey & Fall (1985), who concluded that flows of the order of a few kms^{-1} are necessary in their galactic disc models to reproduce the exponential gas density profiles observed in discs (Bigiel & Blitz, 2012; Wang et al., 2014). Their arguments for the emergence of radial flows were based on physical grounds relating to three processes. Firstly, the viscosity of the gas whereby the gas clouds interact which each other, dissipating energy and leading to inwards flows. Secondly, the angular momentum difference between the newly accreted onfalling gas and the gas already present in the disc. And thirdly, the presence of non-axisymmetric density patterns, such as bars and spirals arms, which can add or remove angular momentum from the gas.

Following this work, many models that study the evolution of disc galaxies include recipes for the transport of gas mass within the disc, usually by modelling the fluxes across different radii, or the radial inflow velocity of gas at a given radius (Kubryk et al., 2015; Cavichia et al., 2014; Bilitewski & Schönrich, 2012; Schönrich & Binney, 2009). These recipes, based on the physical grounds laid-out by Lacey & Fall (1985), are necessary in most cases to reproduce the observed metallicity profiles and construct accurate chemical evolution models.

From a theoretical perspective, Krumholz et al. (2018) have developed a model that includes radial transport of gas via differential equations which depends on parameters such as the surface density and velocity dispersion of the gas, the presence of non-axisymmetric torques and also energy injection and dissipation from star-formation feedback and turbulence. This model is based on previous works (Krumholz & Burkert, 2010; Forbes et al., 2012, 2014) that were aimed at establishing the processes that relate to the radial mass transport in discs. These developments are very useful in constructing advanced semi-analytic models that include radial transport of gas and stars (Forbes et al., 2019). Similarly, Stevens et al. (2018), using the DARK SAGE semi-analytic model (Stevens et al., 2016), allows for radial transport of material in the discs, transferring mass between different annuli when there is a gravitational instability in a given annulus, while conserving the angular momentum in the process.

From an observational perspective, gas movement in the disc plane can be studied using high-resolution 21 cm atomic hydrogen (HI) (Sellwood & Sánchez, 2010; Schmidt et al., 2016; Speights et al., 2019) or CO (Wong et al., 2004) gas maps of nearby galaxies. These studies look for residual non-circular components of the gas motions in the disc by removing the bulk rotational motions. They consistently report radial speeds in the range of a few km s^{-1} towards the center (i.e. inflows). Schmidt et al. (2016) have found evidence of inflowing gas in most of the HI THINGS galaxy sample, but also find some galaxies with no clear inflow, and some with outward gas motions or more complex kinematics, showing that there is substantial variation between different galaxies.

Using zoom-in simulations of disc galaxies, Nuza et al. (2019) have measured fluxes for the gas through cylindrical shells at given radii, looking separately at the inflowing/outflowing gas but also for the fluxes of gas leaving/entering the disc in the perpendicular direction. They report net inwards radial flux in the discs, which is more pronounced in the inner regions and also during the presence of merger events. Goldbaum et al. (2015, 2016) have run isolated disc simulations with and without star formation feedback to study the effect of gravitational instability driven turbulence as a mass transport mechanism in discs. They conclude that the gravitational instability, expressed by the Toomre Q parameter, is a dominant source of radial transport of material even when feedback is present and they find that this transport of gas is sufficient to fuel the star formation in the inner part of discs. They show radial profiles of gas mass fluxes in the disc, measuring fluxes of the order of $\sim 1 M_{\odot}\ \mathrm{yr}^{-1}$ with high variability around the median values at any given radius, with both radially inwards and outwards flows dominating at different times.

With the advent of new generations of high-resolution simulations and numerical codes, modelling gas flows has become more detailed and accurate. Many simulations have also managed to reproduce disc-dominated, rotationally-supported, star-forming systems (e.g. Font et al. 2020; Marinacci et al. 2014; Aumer et al. 2013; Agertz et al. 2013) and have also studied bar formation (Fragkoudi et al., 2020). Driven by these advances, we are opting to use the Auriga simulation suite (Grand et al., 2017) as a means to study detailed gas flows in galactic discs. The gas properties in the Auriga simulations have been studied in Marinacci et al. (2017), finding good agreement with observed properties such as the extent of the gas disc and the radial gas profiles. It has been established in many simulations that merger events are drivers of gas flows to the central regions of galaxies (Bustamante et al., 2018). Furthermore, bars have been shown to be responsible for strong gas flows within the co-rotation radius. In this study, we focus more on the epochs of the disc galaxies evolution that are free of major merger events, in order to examine the gas inflow that arises from the internal processes of the disc evolution or smooth gas accretion from the environment.

Our approach is to use our knowledge of gas flows gained from the Auriga simulation to provide parametrizations that can be readily implemented into semi-analytic models (SAMs) of galaxy formation. More specifically, we would like to later apply the results of this study to the L-Galaxies SAM, that has recently been updated to include radial rings that allow the study of radial dependencies in galactic discs (Henriques et al., 2020). The new model version also includes the radial flow recipe presented by Fu et al. (2013), which allows gas to be transferred from outer to inner rings with an inflow speed proportional to the galactocentric radius of the gas. SAMs have the advantage over hydrodynamical simulations of requiring shorter computational times, allowing for an easier exploration of the parameter space describing sub-grid physical processes, and thus helping us understand which processes are primary and which are secondary in influencing different observational phenomena.

We structure this chapter as follows. First, we outline the Auriga galaxy formation model and the characteristics of the halos that we choose to use. Then, we describe our analysis, which is done using the tracer particles that are implemented in the Auriga runs and is based on a decomposition of the galactic discs into a set of concentric radial rings. In the next section we present our results, looking at the effect of several physical quantities on the process of radial gas inflow and finally, we extract parametrizations that describe this process and we provide a basic method for including these in the context of a semi-analytic model.

2.2 Simulations

Auriga is a set of high resolution, magneto-hydrodynamical cosmological "zoom" simulations for the formation of Milky-Way-mass galaxies. Our sample for this study comprises 14 Auriga halos; 6 halos from the original simulation suite (Grand et al., 2017) with a halo mass[1] in the range $1-2\times10^{12}M_{\odot}$, and 8 simulations of slightly lower halo masses of $0.5-1\times10^{12}M_{\odot}$ (Grand et al., 2019). We have selected these halos because they include tracers particles which are necessary for our analysis. In addition to their mass, halos are selected based on a mild isolation criterion from the $z = 0$ snapshot of the dark matter-only counterpart to the cosmological Eagle simulation of comoving side length 100 cMpc (L100N1504) introduced in Schaye et al. (2015). The cosmological parameters that are used are $\Omega_m = 0.307$, $\Omega_b = 0.048$, $\Omega_\Lambda = 0.693$, $H_0 = 100h$ km s^{-1} Mpc^{-1} and $h = 0.667$, taken from Planck Collaboration (2014).

---

[1] Defined to be the mass inside a sphere in which the mean matter density is 200 times the critical density, $\rho_{\rm crit} = 3H^2(z)/(8\pi G)$.

The initial conditions of the zoom simulations are set at $z = 127$. The high-resolution regions of these simulations have a mass resolution of $\sim 5 \times 10^4$ $M_\odot$ per baryonic element and a comoving softening length of 500 pc h^{-1}. The physical softening length grows until $z = 1$, after which time it is kept fixed. The physical softening value for the gas cells is scaled by the gas cell radius (assuming a spherical cell shape given the volume), with a minimum softening set to that of the collisionless particles.

The simulations are then evolved forward in time with the quasi-Lagrangian magneto-hydrodynamics code AREPO (Springel, 2010; Pakmor et al., 2016) and a galaxy formation model that includes the physical processes important for the formation and evolution of galaxies (for a detailed overview, see Grand et al., 2017). In AREPO, gas cells are modelled with an unstructured mesh in which cells move with the local bulk flow. The galaxy formation model includes primordial and metal-line cooling (Vogelsberger et al., 2013) and a prescription for a spatially uniform background UV field for reionization. Gas that becomes denser than 0.11 atoms cm^{-3} is considered part of the star-forming interstellar medium (ISM), which is modelled as a two phase medium: cold clouds embedded in a hot, volume filling phase (Springel & Hernquist, 2003) assumed to be in pressure equilibrium. Star particles form stochastically from this gas following a Schmidt-type star formation law, and are modelled as Simple Stellar Populations (SSPs) defined by an age, mass and metallicity. The stellar evolution model follows type Ia supernovae (SNe-Ia) and winds from Asymptotic Giant Branch (AGB) stars that return mass and metals (9 elements are tracked: H, He, C, O, N, Ne, Mg, Si and Fe) to the surrounding gas. Supernovae type II are also assumed to return mass and metals following the instantaneous recycling approximation. Galactic winds from SNII are modelled by the wind particle scheme for non-local energetic feedback (Vogelsberger et al., 2013), which effectively models the removal of mass from star-forming regions and deposits mass, momentum and energy into gas of density lower than 5% of the density of star-forming gas. The model includes prescriptions for the accretion of gas onto black holes and energetic feedback from Active Galactic Nuclei (as described in Grand et al., 2017). Magnetic fields are seeded at $z = 127$ with a comoving field strength of 10^{-14} cG (Pakmor et al., 2014). The magnetic field strength in the Milky Way-like halo has been shown to quickly amplify to a strength and radial profile in excellent agreement with observations (Pakmor et al., 2017, 2018, 2020).

For each halo we have 252 snapshots down to redshift 0, spaced at intervals ranging between 45 - 75 Myr with a median value of ~ 60 Myr.

2.3 Methods

2.3.1 Tracer particles

Owing to the quasi-Lagrangian nature of the AREPO code, gas cells move both with the bulk local gas flow and advect mass across their boundaries to neighbouring cells. In order to track the evolution of fluid elements, therefore, we need to follow tracer particles that connect gas cells at different snapshots in time. The tracers are initialized at the beginning of the simulation with one tracer particle per gas cell. Tracers can move across neighbouring cell faces in a probabilistic

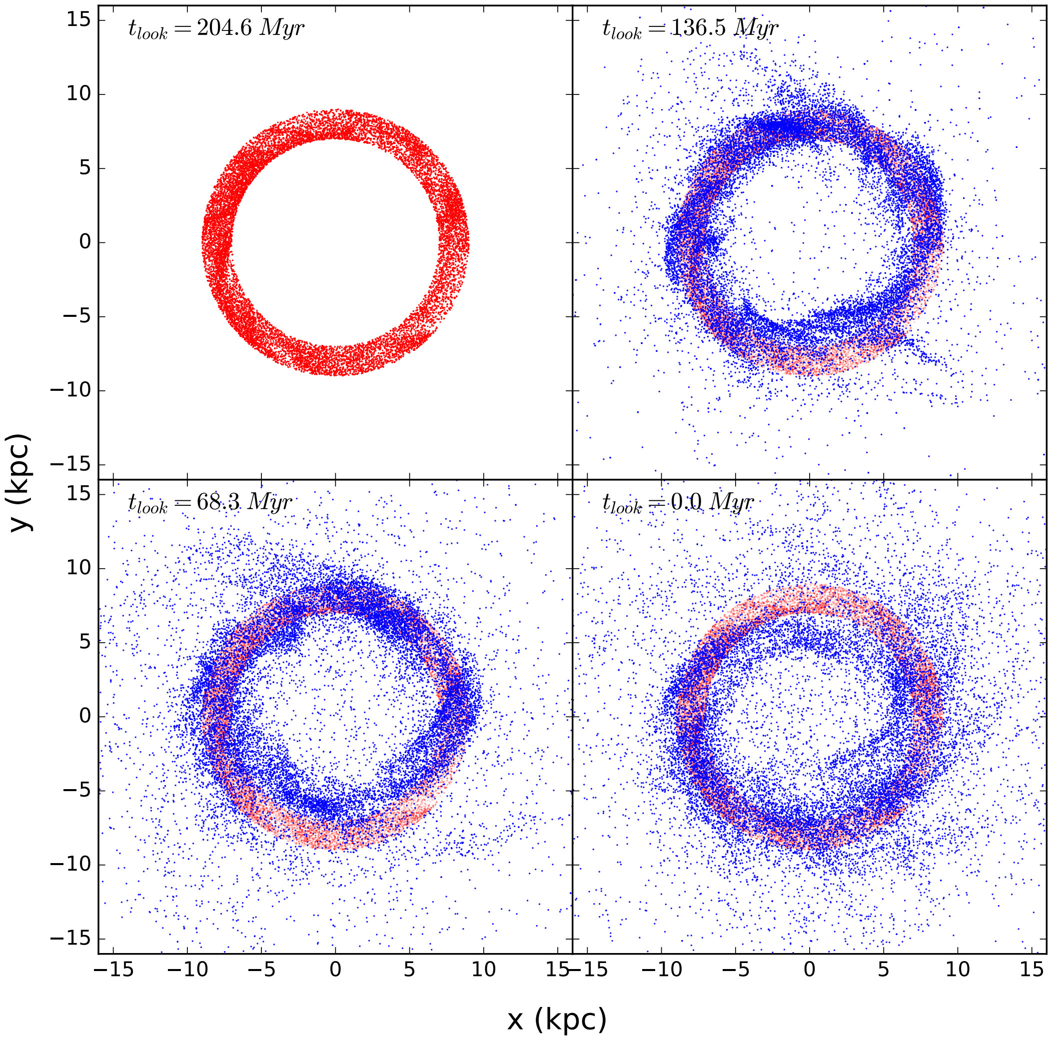

Figure 2.1: Top left: Tracers selected in a ring centered at 8kpc for one of the haloes. Shown here are their x and y positions in the plane of the disc. The next three panels show the evolution of the planar distribution of tracers at the next three snapshots, with the lookback time from redshift 0 quoted on top.

way depending on the ratio of the outward-moving mass flux across the face and the mass of the cell, which is essentially a Monte Carlo sampling of the outward mass flux for each gas cell in the simulation box (Genel et al., 2013; Grand et al., 2019; DeFelippis et al., 2017).

Tracer particles are not exclusively locked in the gas state but can occupy five different cell/particle types depending on the physical processes they are subject to:

- non-star forming gas cells
- star-forming gas cells
- wind particles
- star particles
- black hole particles

A tracer can alternate between the different states. For example if a star-forming gas cell creates a new star particle, the tracer associated initially with the star-forming gas cell will subsequently track the star particle. Tracers can also alternate between the star-forming (SF) and non-star-forming (non-SF) gas phases based on their cell density. Thermal dumps from AGN feedback can directly heat SF to non-SF gas, while cooling processes naturally change non-SF gas to SF. In addition, tracers can transfer into wind particles via supernova activity and potentially return via fountain flows at a later time (Grand et al., 2019). Finally, tracers can move from star particles back to gas cells via stellar evolution, e.g. AGB winds, though this is not a dominant pathway, as Grand et al. (2019) find that comparatively small number of tracers move from star particles to gas cells via AGB winds compared to supernova events.

The Auriga simulation volume is a cube of side length equal to 100 Mpc, with the high-resolution region around the central galaxy being of order 1 Mpc (no low-resolution particles/gas cells are found within this region). In this project, we are interested in the kinematics of the main disc galaxy which in the majority of cases is under 50 kpc in diameter with regard to both its stellar and gas content. Matter structures farther than a few times the disc radius at any given snapshot should not immediately influence the gas flows in the disc, however they may become relevant at a subsequent snapshot. For example, a subhalo just entering the virial radius of the main halo does not influence the central disc. However the material (hence the tracers) carried by this subhalo may potentially become part of the main disc at a later time, should it merge with the main galaxy. Tracers locked in structures that never arrive at the vicinity of the main galaxy are thus ignored during the analysis.

We make a selection of all the tracers which at the final snapshot of the simulation are within a radius of 500 kpc from the centre of the galaxy. When initially selecting tracers, we do not differentiate between those in the gas phase, winds or in stars, since a tracer locked in a star particle at $z = 0$ was most likely in the gas phase at an earlier time and hence was part of the gas inflow that we study. The gas tracers at the final snapshot that are inside or in the vicinity of the disc could either have been in place from early times or been accreted at a later stage smoothly or by merging. Our radial cut is sufficiently large that tracers are unlikely to escape this boundary even if they are launched in winds, ensuring that we do not lose information about the flow elements even at earlier times. Once selected, tracers can be tracked back in time to get information on their positions and velocities.

2.3.2 Ring analysis

Motivated by the implementation of ring decomposition of the cold gas disc in L-Galaxies, we decide to perform a similar kind of ring analysis in Auriga. We aim to have a description of the kinematics of the gas that belongs to a ring centred at a given galactocentric radius in the plane of the disc. We split galactic discs into a series of concentric rings of equal width extending out to 20 kpc from the galactic centre and 2 kpc above and below the galactic plane. In order to do this, we rotate the coordinate system of the simulation box so that the plane of the disc is described by the x and y coordinates, and the z-coordinate indicates the distance above or below the plane. The disc plane itself is determined using information on the angular momentum of the stellar disc in the simulation (as described in Grand et al., 2017). More specifically, the z-axis of the disc plane is identified by calculating the dot product of the eigenvectors of the moment of inertia tensor of star particles within 0.1 R_{200}, with the angular momentum vectors of the same star particles in the coordinate reference frame of the simulation box. The eigenvector of the inertia tensor that is most closely aligned with the principal angular momentum axis is chosen as the z-axis.

Our height and radius cuts are chosen so that they include most of the cold gas that comprises the disc in the majority of cases. The radial cut was selected by inspecting the extent of the cold gas distribution in the different halos. In only one halo did the cold gas disc extend further than 20 kpc, but for the rest of the cases the disc was fully included within the cut. Cold gas tracers above our height cut are not directly associated with the radial motions in the disc that we want to study, but are rather in an accretion phase perpendicular to the disc plane. These tracers are also at a much lower density, so would not significantly contribute to the median properties of the flows we compute for the disc.

Each ring is simply characterised by its galactocentric radius. Given that the extent of cold gaseous discs varies between haloes and snapshots, we choose to normalise the radius of each ring by dividing by the disc radius, of the star-forming gas disc at each snapshot. The radius is calculated as the radius which encloses 95 per cent of the star forming gas in the disc, hence we name it R_{95}. We choose this definition for the disc edge, instead of 100 per cent of the SF gas, to account for cases where blobs of cold gas are potentially accreting in the outer edges of the disc without yet constituting part of it. It should be noted that we do not vary the width of the rings between galaxies or snapshots, and we also use the same number of rings (20) in each case.

For each ring, we identify the tracers in the star-forming gas phase that lie in it at snapshot n and then ask what the positions of these tracers are at the next snapshot $n + 1$. In the absence of major disturbances in the disc, a given parcel of gas initially confined within one ring and at a specific azimuth, will be spread in the next snapshot in a way that follows the rotational motion of the disc. That is to say, the parcel is stretched in the azimuthal direction. Together with radial motion ascribed to bulk flows and/or diffusion, this creates an arc like feature in planar configuration space. This is illustrated in Fig. 2.1, which shows how tracers spread out in the x-y plane from an initial ring, centered at 8 kpc from the galactic centre, over the subsequent three snapshots. We can see from the figure that, after three snapshots, there is considerable radial

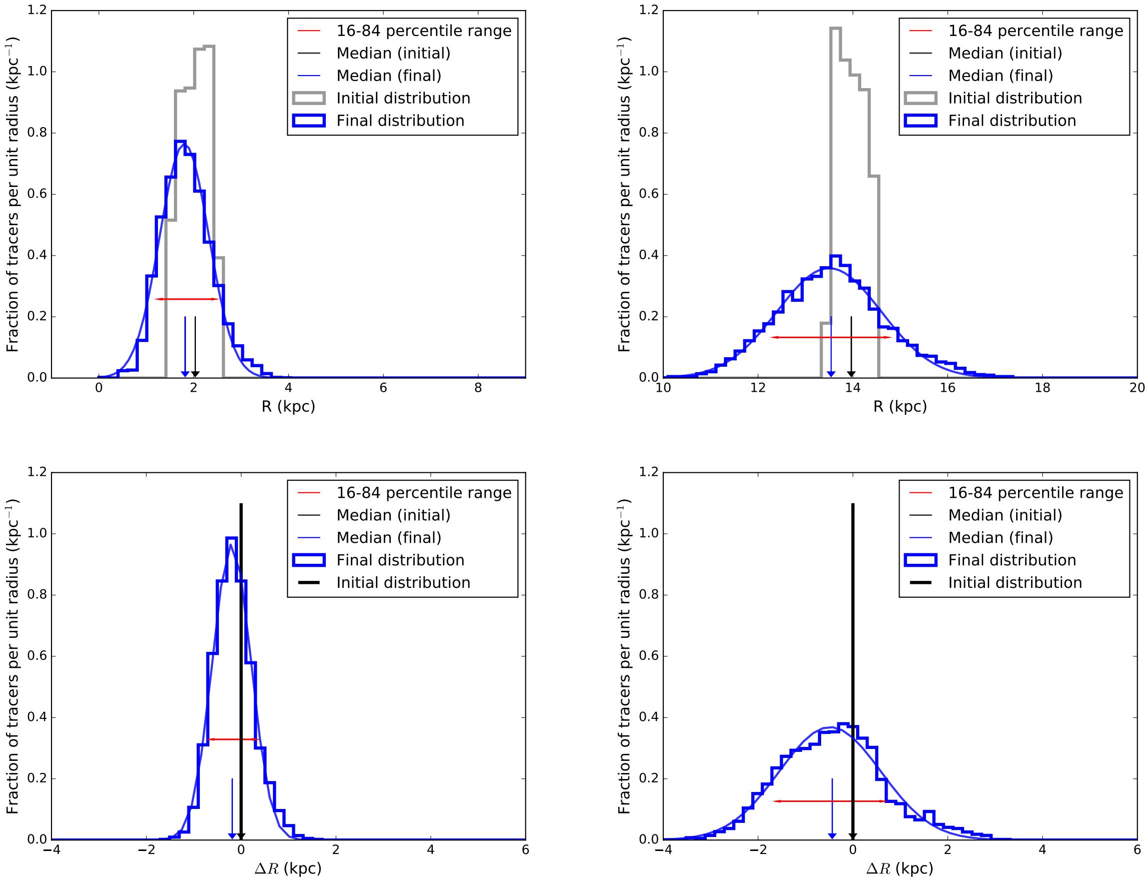

Figure 2.2: Examples of the histograms that are computed in order to extract the information for the dispersion of tracers. At the top row we show the histograms in terms of the galactocentric radius of the tracers. The initial distributions (in gray) are calculated at snapshot n and the final (in blue) at the subsequent snapshot n+1. At the bottom row we show the histograms for the same rings in terms of the difference in galactocentric radii $\Delta R = R_{n+1;n} - R_n$. In this case the distribution at snapshot n is a delta function whereas the one at $n + 1$ displays the spread and median shift of the tracers. The median of the distributions in all cases is marked with the vertical arrows. Over-plotted is the Gaussian fit to the final distribution. The red horizontal arrows show the 16-84 percentile ranges of the final distribution. Here we select the cases for an inner ring (left) at ~ 2 kpc and an outer ring (right) at ~ 14 kpc to show the difference in the spread of the tracers.

movement of the tracers spreading both inwards and outwards from the initial ring boundaries.

We can quantify this effect of gas redistribution by constructing the histogram of the new radial position of tracers at snapshot $n + 1$. Initially, at snapshot n, the distribution of tracers is approximately a top hat function with the width of the ring and median at the centre of the ring. At the next snapshot, the movement of tracers outside the ring leads to a new distribution with an different width (usually larger) and a shift (inwards or outwards) of the median of the distribution. We can directly utilize the information of the distribution at $n + 1$ to describe the radial motion of the gas, using the difference between the new and initial median as a measure of the bulk radial motion and the width of the distribution as the measure of the spread of values around the new median. The caveat with this approach is the introduction of a floor in the value of the width because the width of the top hat distribution at snapshot n is inherently included in the width of the distribution at snapshot $n + 1$. This can become more problematic at the inner rings where gas is naturally more constrained in its radial motion. To avoid the presence of a floor value we can alternatively look at the distribution of tracers expressed by the difference in their initial and final galactocentric radii, by computing $\Delta R = R_{final} - R_{initial}$ for each individual tracer. Then by construction the initial distribution at snapshot n is a delta function at $\Delta R = 0$ and the distribution at $n + 1$ is a histogram centered at the new median with its the width similarly measuring the spread around the median, unconstrained from of a floor value. By testing both approaches we find that the resulting values for the widths are comparable, apart from the innermost rings, so the effect of the width of the ring does not appear very pronounced in the spread of the tracers between the two snapshots. Nevertheless, it is more reliable to use the histograms of ΔR in our analysis, eliminating the possible effect of the width of the rings on the results. In Fig. 2.2 we show the histograms both in terms the galactocentric radii of the tracers and the difference ΔR.

Tracking gas motions

In our analysis, we exclude the tracers that in the time between the two snapshots have been in the wind phase. Although wind particles are launched in random directions in the Auriga wind implementation, the enhanced matter density in the plane of the disc restricts the outflows mainly in the perpendicular direction to the disc in a fountain flow. As a result, between the two snapshots a tracer can be launched from an inner ring in fountain trajectory and re-deposited in an outer ring. Hence, tracers that have been or are in winds may contaminate the information about pure radial motions within the plane. Tracers that have entered a wind particle are removed only for the snapshot pair but once they have returned to the disc later they may be included again as long as they have not entered a wind particle between the next pair of snapshots.

We further clean the sample by removing the data for rings belonging to halos that are in a merger state or more generally experiencing interaction with a satellite subhalo at a given snapshot. We choose 1/50 as the limit for the subhalo-to-central total mass ratio for a merger of importance. Merger cases are excluded on the reasoning that the disruption of the disc in the merger process can be significant enough that the cylindrical symmetry is lost and assigning rings cannot accurately represent the geometry of the gas motions. Mergers with the central galaxy can be identified using the SUBFIND (Springel et al., 2001) catalogs that are available for the simulations. We remove the snapshots at which the merger occurs according to SUBFIND and

3 snapshots, or equivalently $\sim$ 180 Myr, before and after the merger to partially account for the tidal interactions in the gas and stellar distribution that happen during the merger process and the time for the disc to settle after the merger. Changing the merger ratio limit to higher values (e.g. 1/10) does not influence significantly the results owing to the fact that most of the halos in the last 6 Gyr have very quiet merger histories and there are not many mergers in the mass ratio range 1/10 to 1/50. The number of halos we study is small enough that we have also visually checked the positional distribution of the gas tracers between the different snapshots and confirmed that this method successfully removes periods of significant disturbance by mergers. Filtering out the snapshots during merger phases removes 30 per cent of the total rings in the sample.

In Fig. 2.2, we choose to demonstrate characteristic examples of histograms obtained for two rings in the same halo, one inner and one outer one. We find that the histograms tend to be reasonably symmetric around the new median position of the gas, i.e. gas tracers travel both inwards and outwards in the radial direction by roughly the same amount. In the majority of cases, the histograms can be accurately fit by a Gaussian function and we can use the standard deviation of the Gaussian to approximate the width of the distribution. However, there are cases for which the distribution of tracers in the next snapshot is not well approximated by a Gaussian (see example in Appendix A Fig. A.1). These cases arise almost exclusively in the outer rings of discs, which are more susceptible to external interactions (from subhalos) or mixing with the newly accreted gas because of their lower surface density. Furthermore, in the case of mergers, we observe more irregular distributions because the incoming subhalo can disturb the outer regions of the disc, leading to histograms that appear skewed or more random with large amounts of material having moved much further inwards or outwards. Skewed distributions are mostly eliminated by the merger cut.

Due to the possibility of such asymmetric distributions, we prefer to use the percentile ranges in order to describe the width of the distribution in this work. The 16-84 percentile range in particular is useful for evaluating the goodness of Gaussian fitting. If the histogram resembles a Gaussian, then the 16-84 percentile range should be very similar to twice the width of a Gaussian fit, 2σ. We find that in most cases the two quantities can be used interchangeably, as shown in Fig. A.2 in the Appendix A.

We thus extract two quantities from the shape of the histograms: the 16th-84th percentile divided by 2, which we will refer to as the 'width', w, in kpc; and the difference in median galactocentric radius between the initial (at snapshot n) and final (at snapshot $n + 1$) tracer distribution, which we will refer to as the 'median shift', $\Delta\mu$, in km s^{-1} (i.e. normalising by the time difference Δt between the snapshots).

There is a potential caveat that, to perform this kind of analysis, we ideally need to have a large number of tracers in a given annulus. Annuli with an insufficient number of tracers can contaminate the sample by mere lack of statistics, which leads to low confidence in the measurement of the percentile range. This becomes a problem usually in the outermost rings, where the density of cold/star-forming gas is low. Therefore, in this work we only consider annuli with a minimum of 500 tracers at snapshot n. This cut only removes 0.8 per cent of the rings.

We repeat the above process between all pairs of consecutive snapshots. This gives us a set of data for each ring that is its radius, its initial snapshot, the spread, and the median shift,

$$\mathrm{Ring}\,(\mathrm{halo}_j,\, r_i,\, t_k,\, w_{ijk},\, \Delta\mu_{ijk}) \tag{2.1}$$

where halo_j is the jth halo to which the ith ring belongs at the kth snapshot. Carrying out the analysis for the 14 halos, splitting each disc into 20 rings and working over 100 snapshot pairs, provides 28000 data points in the raw sample. We use the 100 last snapshots of the simulation , which is a total of lookback time of approximately 6 Gyr.

Furthermore, each ring has a set of associated properties that can be measured, such as the gas surface density Σ_{gas}, total surface density Σ_{tot}, gas fraction f_{gas}, velocity dispersion σ_{tot} (as well as in individual directions σ_{r}, σ_{z}), the Toomre Q parameter for the gas $Q = (\sigma_{gas}\kappa_{gas})/(\pi G \Sigma_{gas})$, κ being the epicyclic frequency and σ_{gas} the total gas velocity dispersion using all three spatial components, and finally the star formation rate. These quantities can be extracted from the tracer particle data which inherit their properties from their parent gas cells. The velocity dispersion is calculated using the individual velocities of each tracer in the gas phases. The surface densities, are computed by counting the number of tracers in the gas phases (Σ_{gas}) and stars and gas phases (Σ_{tot}), multiplying by the associated masses and dividing by the surface area of the ring. In addition, we calculate the accretion rate onto a given ring $\dot{M}_{\mathrm{acc}}$ and the accreted mass fraction ,that is the accreted mass divided by the gas mass already present in the ring, $f_{\mathrm{acc}} = M_{\mathrm{acc}}/M_{\mathrm{gas}}$. The accreted mass is calculated by counting the tracers which are in the gas phases (non-SF and SF) and which at snapshot n are outside the ring limits and at snapshot $n+1$ within them. This is strictly accretion of material that is external to the defined disc region at the initial snapshot and does not include material exchange between different rings. The accretion rate is then given by the total mass of accreted tracers divided by the time between the two snapshots, $\dot{M}_{\mathrm{acc}} = M_{\mathrm{acc}}/\Delta t$. We also divide the accreted mass fraction by the snapshot spacing to get a time-normalised quantity: $\dot{f}_{\mathrm{acc}} = f_{\mathrm{acc}}/\Delta t = \dot{M}_{\mathrm{acc}}/M_{\mathrm{gas}}$. The quantity $\dot{f}_{\mathrm{acc}}$ is essentially the inverse of an accretion timescale.

Evolution over time

In the fiducial case, we calculate w and $\Delta\mu$ between consecutive snapshots (i.e. between snapshots n and $n+1$), but we can equally compute them for the time between snapshots n and $n+2$ or $n+3$. In these cases, the time difference is roughly two and three times longer, so the histograms appear naturally broader. The quantity w, as expressed in kpc, is therefore dependent on different timestep or snapshot spacing selections. By looking at the evolution of w in a given ring between $n+1$, $n+2$ and $n+3$, we can identify its time dependence, assuming it follows a proportionality of $w \sim \Delta t^a$, where Δt is the time difference between the two snapshots. This is important if we want to have our parametrized quantities in a timestep invariant form, so that the result can be generally applied to models or simulations with different timestep widths. In Figure 2.3, we show an example of how the radial positions of a group of tracers in a given ring have evolved after 1, 2 and 3 snapshots. We stop at 3 snapshots after snapshot n, which is a time interval comparable to the dynamical time of the disc for most radii, because is sufficient to capture the radial flows that we want to study. Using n+4 or n+5 gives convergent results in the radial and time evolution of w and $\Delta\mu$. If we proceed further, the histograms deviate from a Gaussian distribution, losing

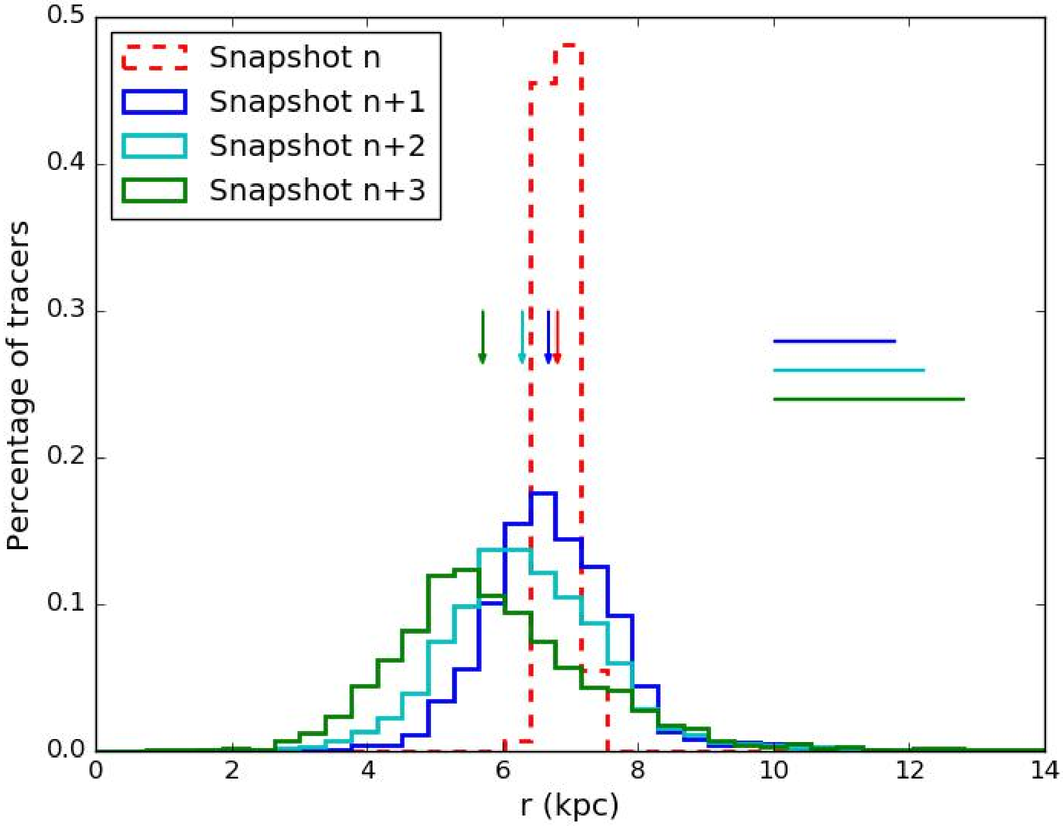

Figure 2.3: Radial distribution of the tracers selected in a ring initially at snapshot n as it evolves at subsequent snapshots $n+1$, $n+2$ and $n+3$. The arrows show the medians of the distributions and the horizontal lines the 16-84th percentile.

a clear peak. In addition as we use larger time difference we increase significantly the error on the measurement of the quantity w.

In section 2.4, we provide the exact time dependence of w and how different snapshot spacings influence it and $\Delta\mu$.

Redshift and mass dependencies

In order to check if there is any significant redshift dependence to the radial flows studied here, we have initially split all the output snapshots into three broad time bins of 2 Gyr. Each bin contains approximately 30 snapshots, for which we calculate the tracer positions at all the snapshot pairs n and $n+1$. We find that the there is no significant redshift evolution in the trends that we present in Section 2.4. Furthermore, we have split the sample between the seven most massive and least massive halos, but find no evidence for any mass dependence. Therefore, for our final study we combine the data over the last ~6 Gyr (100 snapshots) for all the halos.

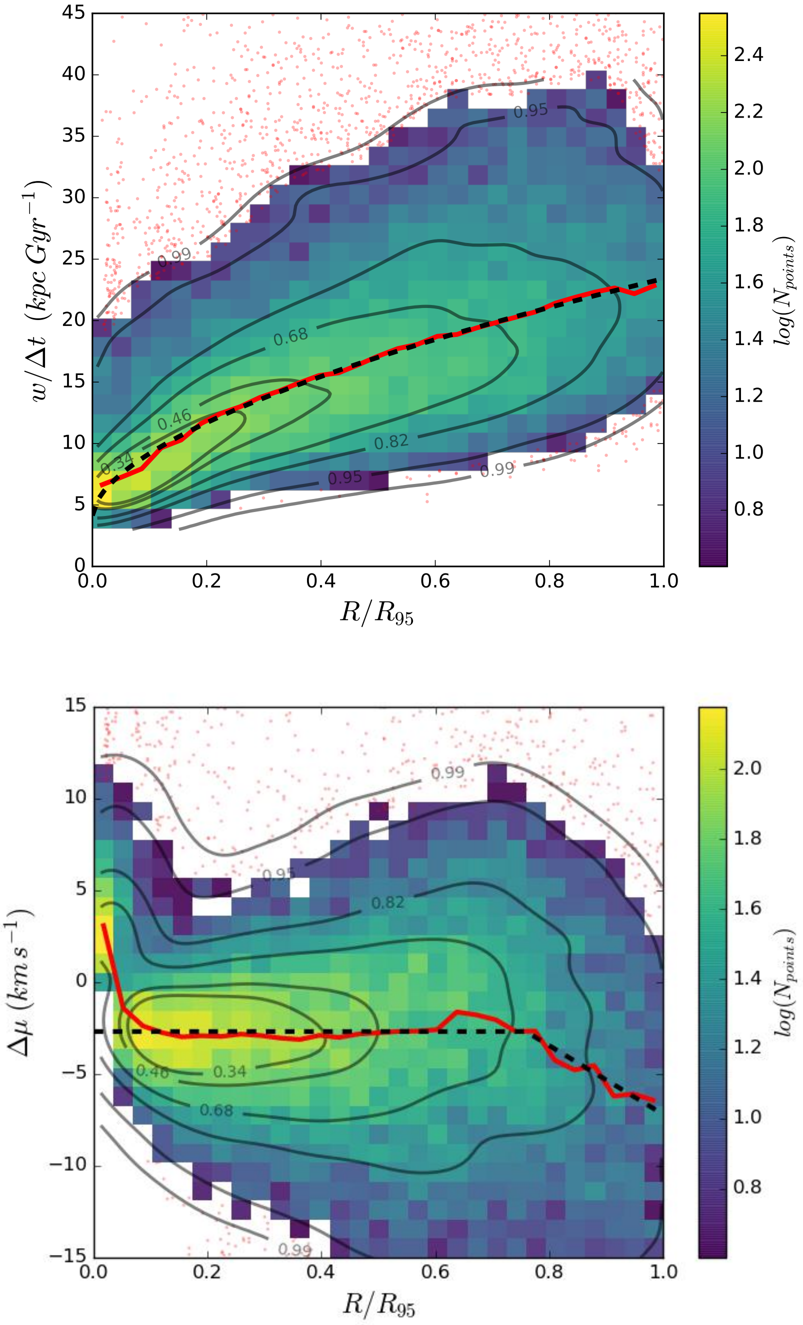

Figure 2.4: Radial dependence of the spread w (left) and the median shift $\Delta\mu$ (right). The data points, for all 14 halos over the range of 6 Gyr, are represented as a number histogram and the red line shows the median curve. Also shown the contours enclosing a given percentage of the points. For these plots, we evaluate the quantities using consecutive snapshots with time difference 60 Myr on average. We observe an increasing trend with the radius for w which can be fit with a power law. In this plot we present w normalised by the snapshot spacing Δt to account for the small differences in the exact spacing between the different snapshot pairs. For $\Delta\mu$ there is a flat trend up to 0.75 disc radii and a linear drop in the outer regions where there is faster inflow of material.

2.4 Results

The first observation that we naturally want to test is how w and $\Delta\mu$ vary with the radial position of the ring. We find that w is larger on average for rings at larger galactocentric radius. The median of the $r - w$ relation for the whole sample can be best fit with a power law of with slope < 1, as shown in the left panel of Fig. 2.4. In the inner regions of discs, $\Delta\mu$ is a constant value of around $-3\,\mathrm{km\,s^{-1}}$ up to almost 70% of the disc radius, in agreement with the observations that show gradual inflows of gas in disc galaxies (e.g. Schmidt et al. (2016)). In the outer regions, the value of $\Delta\mu$ becomes more negative, ranging between -3 and -15 $\mathrm{km\,s^{-1}}$ on average, indicative of enhanced gas inflow. In the very centre of galaxies, positive (outwards) values of low speed are a manifestation of the fact that the gas in the innermost ring cannot travel any further inwards but also that higher outflow speeds are driven by central AGN feedback.

The above statements are visualised in Figure 2.4, which displays the compilation of data for all the halos over the selected rings (excluding merger cases and low number of tracers, as discussed in Section 2.3.2) and over the aforementioned snapshot range.

These statements hold true if we average the data for all halos (as shown in Fig. 2.4) but also if we look at each halo individually. For an individual halo, the curve of w and $\Delta\mu$ versus radius can be less smooth in some cases, although the radial trends are still similar. We find that before removing the merging stages, halos with quieter merger histories and a more stable disc evolution return more consistent results between different time intervals.

For three of the halos from the higher mass sample ($1-2\times10^{12}M_\odot$) in our simulation suite, we measure high w and irregular $\Delta\mu$ values at inner radii. Looking directly at the cold gas tracer x-y plane for these halos, we see large holes devoid of gas in the inner regions which have bubble like profiles. These holes are created by feedback from the AGN, which pushes gas out of the central region, increasing the w measured and giving positive (outwards) $\Delta\mu$ values in these rings. We mitigate these feedback effects by removing the tracers that have been in wind particles, but the overall feedback effect cannot be removed completely. However, these bubbles are only present in a small subset of the snapshots, so do not influence our conclusions statistically.

We test for the convergence of the results by varying the number of radial bins and the height cut. In the first case, if we use a very small number of rings (e.g. 5-7, compared to the 20 rings we use by default), we get higher values for the spread at a given radius. Using more than 25 is oversampling and results in a low number of tracers per ring. In general, we get convergent results if between $\sim$ 10 and 25 rings are used. Varying the maximum height above and below the disc plane between 2 and 4 kpc does not have any qualitative effect on the median trend, although there is no convergence if we use a very conservative height cut (<1 kpc), because not all the tracers that are relevant for disc flows are included.

2.4.1 Timestep invariant expression of w and $\Delta\mu$

As mentioned above, in Fig. 2.4 we present the quantities w and $\Delta\mu$ as calculated between two consecutive snapshots in the simulation. The time difference, Δt, between consecutive snapshots is on average 60 Myr, with a range between ~50-70 Myr. Given this, when looking between snapshot n and $n+2$ or $n+3$, Δt increases to $\sim 100-140$ Myr and $\sim 150-210$ Myr, respectively.

$\Delta\mu$ is presented in units that already account for such differences in Δt, but this is not the case for w. In Fig. 2.5, we show how w and $\Delta\mu$ vary on average if calculated between snapshots n and either $n+1$, $n+2$, or $n+3$. For $\Delta\mu$, we find a convergence in the results around the value of $-3\,\mathrm{km\,s^{-1}}$. For w, a dependence on the number of snapshots chosen is clear. From the distance between the median curves in the top-left panel, we get an indication of how w varies as we double or triple the size of Δt. The increase is not directly proportional to Δt, as shown in the top-right panel where we plot the quantity $w/\Delta t$. Instead, for the quantity $w^2/\Delta t$, corresponding to a $\sqrt{\Delta t}$ time dependence, we see better convergence within the scatter. However, we also find a systematic trend where $n+3$ lies lower on average than $n+2$, which in turn is lower than $n+1$. Whether the spread of the tracers was governed by a pure diffusion process, we would expect a time invariance with $w^2/\Delta t$. Finally, $w^3/\Delta t$ converges very well in all three cases in the inner disc, and the deviation in the outer parts shows no systematic (i.e. the $n+3$ median line now lies in between the other two) so it is also consistent within the scatter. Hence, $w^3/\Delta t$ appears to be the quantity that is most timestep invariant when describing the spread of the tracers.

We want to quantitatively confirm the cubic power dependence by running the following test. Based on the assumption that $w \sim \Delta t^a$, it follows that $w^b/\Delta t$ = const., where $a = b^{-1}$, independently of whether w is calculated between the pairs of snapshots $[n, n+1]$, $[n, n+2]$ or $[n, n+3]$. So, in order to identify the best value for the power b, which will show us how w evolves with time, we calculate the following three ratios,

$$\begin{aligned} q_{12} =& (w_1^b/\Delta t_1)\,/\,(w_2^b/\Delta t_2) \\ q_{13} =& (w_1^b/\Delta t_1)\,/\,(w_3^b/\Delta t_3) \\ q_{23} =& (w_2^b/\Delta t_2)\,/\,(w_3^b/\Delta t_3) \end{aligned} \tag{2.2}$$

where the subscripts on the right-hand side 1, 2, 3 show, respectively, whether w and Δt have been calculated between $[n, n+1]$, $[n, n+2]$ or $[n, n+3]$ for the tracers in a given ring at snapshot n. We can also combine the data for the three ratios to include the information for all three timesteps that are examined. If $w^b/\Delta t$ = const. holds, these ratios should ideally be equal to 1 for the value of b that better describes the process of radial spreading. We thus identify the value of b that minimizes the difference of

$$\sum_{rings} (q-1)^2 \quad , \tag{2.3}$$

where q can either be each of the above ratios independently or the combined data for all three of them. The above sum is minimised very close to the value $b = 3$ (exact value 2.97) when using all the data, as shown in Fig. 2.6, indicating that the quantity $w^3/\Delta t$ is the most timestep invariant. When using the individual ratios the minimum values range around $b = 3$ from 2.7 to 3.4. If we consider only the outer part of the disc (r/R_{95}>0.75) the minimum value for b is 2.7 or only for the inner part (r/R_{95}<0.75) $\mathrm{b}_{min} = 3.2$. We will define $\delta = w^3/\Delta t$ for simplicity from now on. This will be the quantity we aim to parametrize along with $\Delta\mu$. In Fig. 2.7 we show the radial dependence of δ for the whole sample of rings.

2.4.2 Dependence on physical properties

We would like to check whether the radial dependence of w and $\Delta\mu$ are driven by some physical process, or are correlated with physical properties either of the individual rings or the galactic disc as a whole.

If any dependencies present are not due to a global disc property, i.e. do not vary significantly among galaxies, then we can treat each ring as an independent data point no matter which halo it belongs to. Then, the premise is that the width of the histogram is driven by some local, internal property within the ring or process associated with it (for example the perturbing effect of a local feature such as a spiral arm). As mentioned before, we observe an increase in w with increasing radius (see Fig 2.4). There is a considerable scatter in this relation, but the overall trend is clearer when taking mean values of the spreads for given radii.There is also large scatter in the relation of $\Delta\mu$ versus radius towards both negative and positive values, which become more pronounced in the larger radii.

The source of the scatter could be due to a lack of homogeneity among the halos or a dependence on a secondary parameter that could be either directly measurable in the simulation output or acting in between the snapshots. When separating the data between the different halos and reproducing the $w - r$ and $\Delta\mu - r$ relations for each, we find that their median relations lie very close to each other and hence we cannot attribute the scatter in the full dataset to halo variance.

We have chosen to examine a number of local properties that could potentially influence w. Firstly, we consider the total baryonic surface density (Σ_{tot}), the gas surface density (Σ_{gas}), and their ratio the gas fraction (f_{gas}). These properties can tell us whether there is a direct relation between the flows and the amount of material in the ring, as well as distinguish between the effect of gas and total baryonic mass. We also consider the gas velocity dispersion (σ), which is a measure of the internal kinetic energy of the material and of the amount of turbulence. This is further split into the velocity dispersion in the radial direction (σ_r) and that perpendicular to the disc plane (σ_z), in order to identify which is dominant. We also examine the effect of accretion, which has been postulated as a driver of radial flows, by computing the mass accretion rate ($\dot{M}_{acc}$) onto a ring and the accreted gas mass fraction ($\dot{f}_{acc}$). Finally, the star formation rate (SFR), which relates the energy deposition from stellar feedback to the gas that could drive flows and the Toomre parameter Q as a measure of the gravitational instability that, as mentioned before, has also been related to gas flows.

In Figure 2.8, we plot δ against the four properties which correlate most strongly with it. The median curves are plotted above the density histograms to show the trends more clearly. Again, these plots have a non-trivial amount of scatter but also well-defined loci where we have the highest point density. We choose to present δ here, rather than w, as the trends seen are qualitatively similar and δ is the quantity we decide to parametrize in the following section.

We can see in Fig. 2.8 that δ increases with increasing gas fraction, increasing accreted gas fraction, and decreasing total (and gas) surface density. We also find that there is an increasing trend with the velocity dispersion σ_{tot}, which is mainly driven by the radial component σ_r. There is no trend seen with SFR or Toomre Q. It essential to differentiate which of these trends are just correlations with radius, and which have an independent contribution. For example, the increase in δ and decrease in Σ_{tot} with radius naturally leads to an anti-correlation between δ and Σ_{tot}, but does not necessarily mean that the two are causally connected.

The correlation with σ_r can be understood on physical grounds since the tracers in a ring with high velocity dispersion, are more likely to travel to larger distances resulting in broader histograms with higher values of δ. Concerning $\dot{f}_{acc}$, a larger amount of accreted material is likely to disturb the existing material in the ring, driving radial motions. There is a similar, although weaker, trend with the accretion rate to the ring.

Concerning $\Delta\mu$ there are only weak trends with the gas accretion rate, accreted gas fraction, and the velocity dispersion. Larger accretion and velocity dispersion lead to more negative velocities (i.e. larger inflow speeds). The quantity that correlates most strongly with $\Delta\mu$ is the mean change in the specific angular momentum of the gas, as shown in Fig. 2.9. The specific angular momentum in the z-direction of a gas cell is expressed as $l_z = |\mathbf{x} \times \mathbf{v}|$ or simply rv_{rot}. We calculate the change in angular momentum Δl_z for each tracer by taking the difference in the angular momentum in the z-direction (i.e. out of the plane of the disc), l_z, between snapshots n and $n+1$. The values for l_z are drawn from the parent gas cell for each tracer as it is for the other tracer properties. The correlation between $\Delta\mu$ and Δl_z is expected, since a loss of rotational angular momentum will lead to inward motions, expressed as the negative change in the gas' median position. Following the definition of l_z and since most of the gas is in nearly circular orbits in the disc and the rotational velocity curves are reasonably flat, a change in angular momentum Δl_z is correlated with a change in radius, which is expressed as the median shift, $\Delta\mu$, in our case. Further insight is needed with regard to the process that causes the angular momentum change, and hence the bulk flow, in each case.

2.4.3 Identifying the strongest correlations and causations in the data

We have tested for secondary dependencies of δ and $\Delta\mu$ at fixed radius by plotting the residuals around the median $\delta - r$ and $\Delta\mu - r$ relations. The residual is simply the distance of a given data point from a fit to the median relation, which in the case of $\delta - r$ is parametrized as a power law and in the case of $\Delta\mu - r$ as a piece-wise linear fit. Looking at the residuals allows us to make a distinction between quantities that are actual drivers of trends in δ and $\Delta\mu$, and those that only correlate because of a third property (in our case the radius). We quantify the strength of the relation between the residual and a secondary property by calculating the correlation coefficient between the two. Table 2.1 shows the values of these correlation coefficients for the selected quantities, both for the residuals in δ and $\Delta\mu$. A higher absolute value of the correlation coefficient is an indication that this quantity is more likely to drive the scatter we observe around the median.

First of all, we find that the residuals do not show evidence of time dependence as there is an absence of correlation with redshift, and nor any correlation with a specific halo. f_{gas} is an example of a quantity that shows positive correlation with δ but no trend with the $\delta - r$ residuals. On the other hand, the velocity dispersion σ_{tot} has a positive correlation with the $\delta - r$ residuals. Upon splitting the velocity dispersion into different components, we find that this correlation is driven mostly by the dispersion in the radial direction σ_r. In other words, the scatter in the $\delta - r$ plane is produced primarily by the different σ_r among rings at a given radius. Differences in the accreted gas fraction also play a role in producing the scatter seen. The residuals as a function of

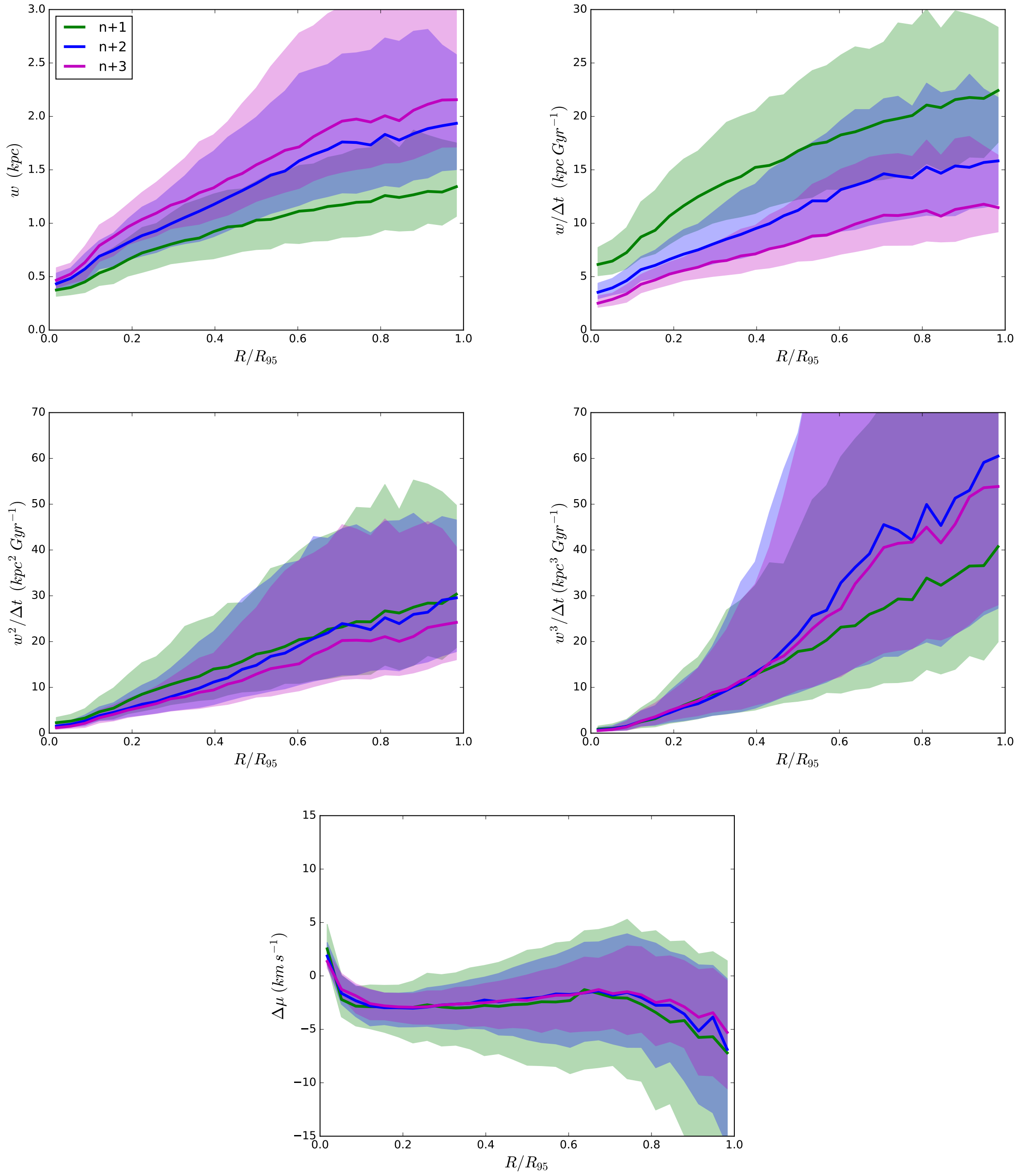

Figure 2.5: Mean radial profile of w (top left), $w/\Delta t$ (top right), $w^2/\Delta t$ (middle left), $w^3/\Delta t$ (middle right) when calculated between snapshots n and $n+1$ (green), $n+2$ (blue) and $n+3$ (magenta). w naturally has higher values for the larger timestep case, between n and $n+3$. The quantity $w^3/\Delta t$ is the one that leads to the best convergence between the three cases in contrast to a simple $w/\Delta t$ expression which does not represent the time evolution of w accurately or $w^2/\Delta t$ which shows a systematic dependence. Bottom right panel: The radial profile of the median shift $\Delta\mu$ is similar in all three cases showing a consistent calculation of the bulk inflow velocity. The shaded regions show the 1σ intervals around the median curves.

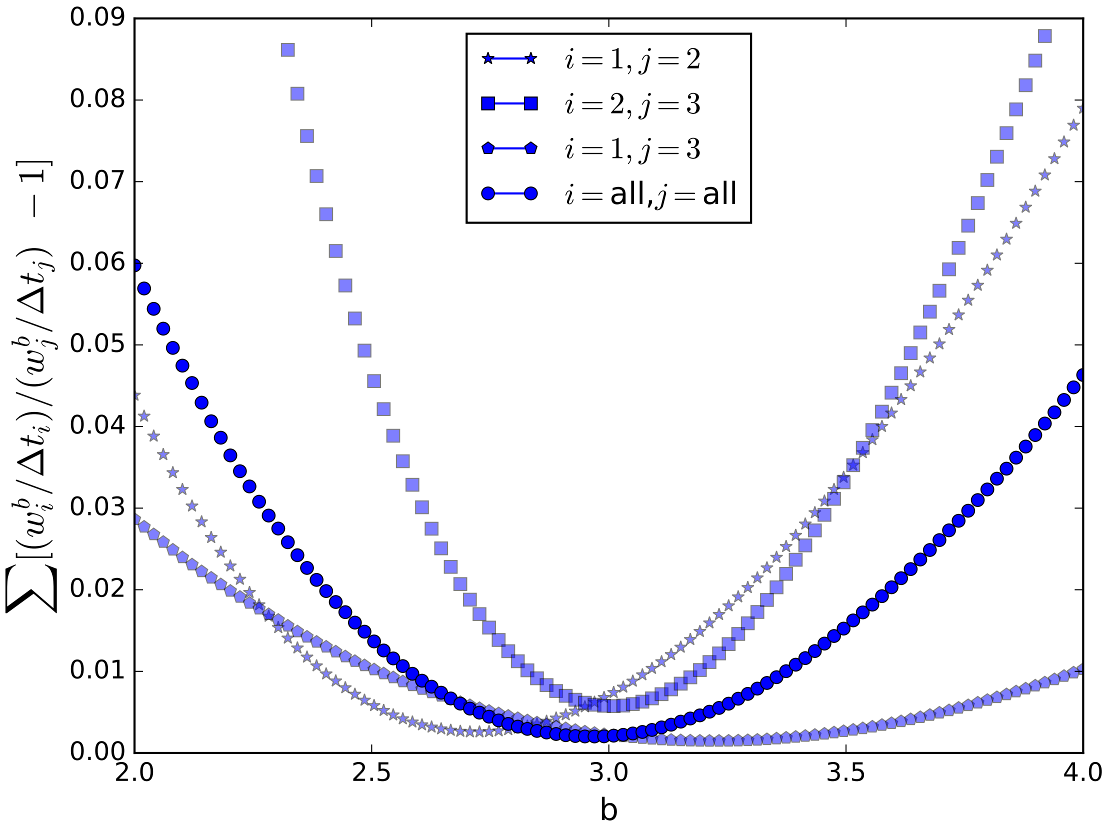

Figure 2.6: The ratios described by Eq. 2.2 in Section 2.4.1 help us identify the best fit value for the power in the expression $w^b/\Delta t$. The x-axis has a range of b values and the y-axis is the measure of the deviation of the ratios from 1 where a smaller value in the y-axis indicates a better fit around 1. The combined data (solid circular points) yield a minimum for the parameter b at a value b = 3, while also taking each ratio individually (semi-transparent points) gives us minima values around b = 3.

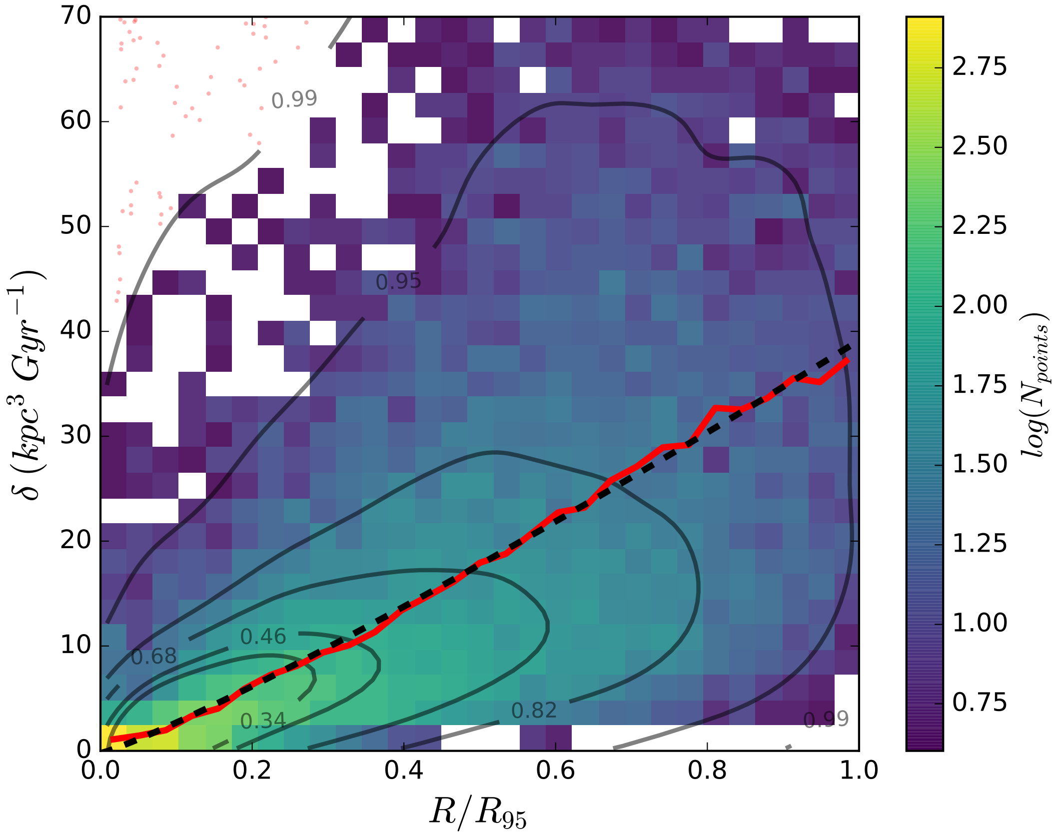

Figure 2.7: Radial dependence of δ, similar to Fig. 2.4, showing the best fit to the median relation. The best fit power is 1.1, slightly different to a linear relation in the inner radii.

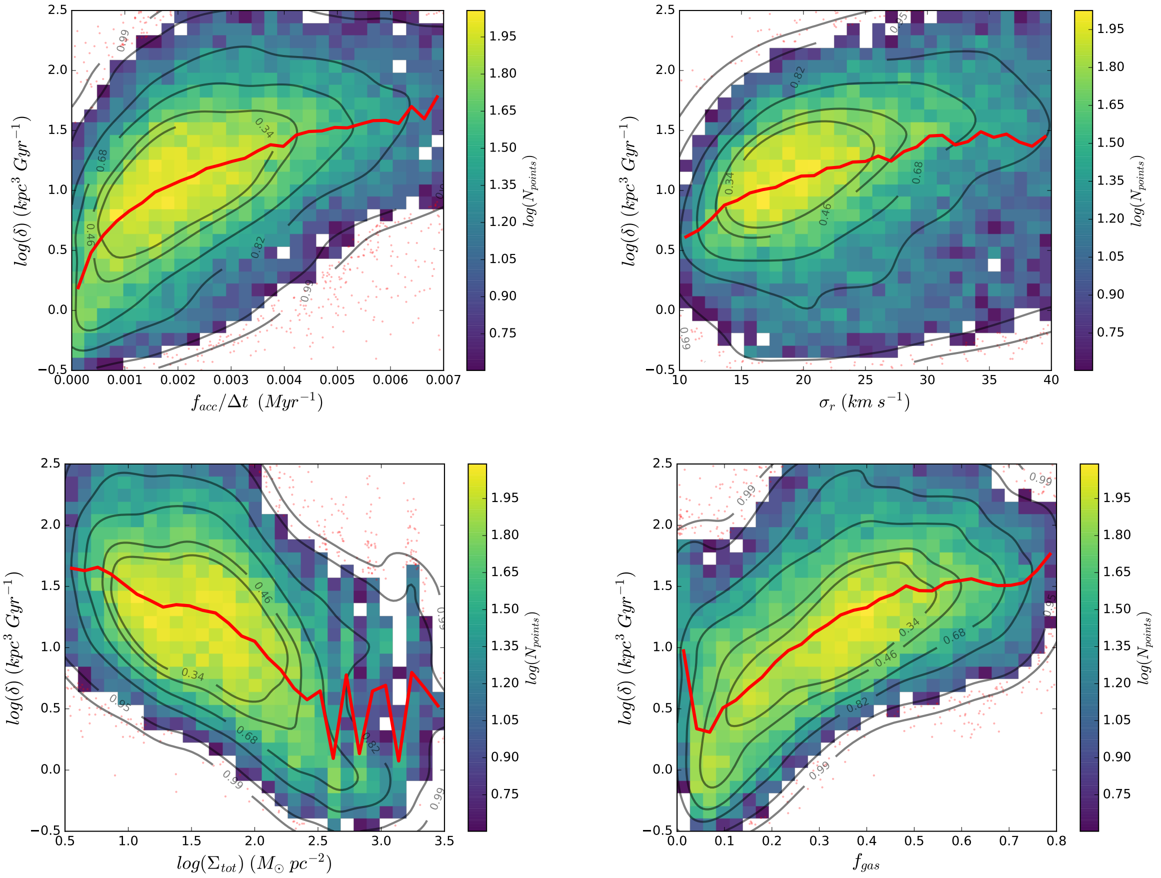

Figure 2.8: Top row: Accreted-to-total gas mass fraction normalised by snapshot spacing (left) and gas velocity dispersion in the radial direction (right) plotted against the spread measure δ. The points are represented as a number histogram and the red line shows the median curve. Also shown the contours enclosing a given percentage of the points. Bottom row: Total surface density and gas fraction plotted against the spread measure δ. The points are represented as a number histogram, the red line shows the median curve. Also shown the contours enclosing a given percentage of the points. There is an anti-correlation in the case of total surface density and a correlation with gas fraction. These trends arise as a consequence of the radial dependence of δ and the radial dependence of these quantities and do not indicate a direct physical relation.

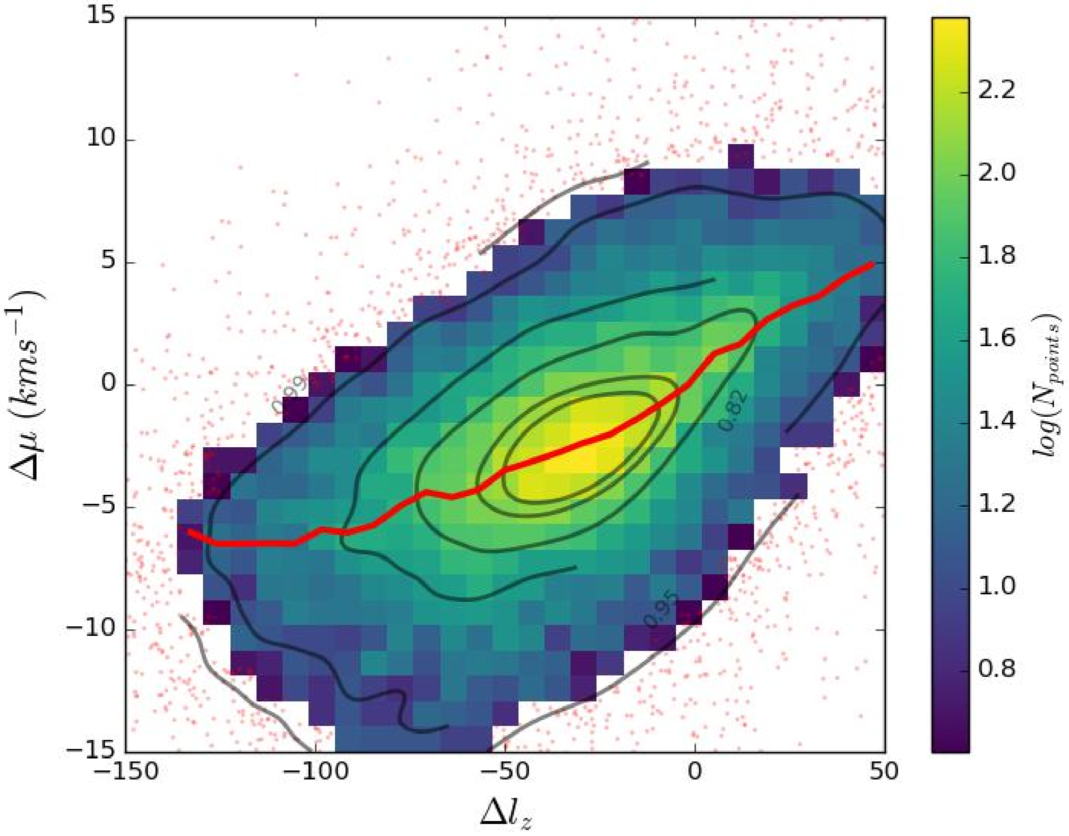

Figure 2.9: The correlation between the median shift and the change in the specific angular momentum of the tracers is an indication that we observe a phenomenon where the inwards motion of gas (negative $\Delta\mu$ values) is associated with a loss of angular momentum (negative Δl_z).

Quantity	R_{corr} with δ	R_{corr} with $\Delta\mu$
z	-0.09	0.07
Σ_{tot}	-0.01	0.18
Σ_{gas}	0.06	0.16
f_{gas}	0.09	-0.07
σ_{tot}	0.25	0.08
σ_r	0.28	0.03
σ_z	0.23	-0.04
$\dot{M}_{acc}$	0.11	0.22
$f_{acc}/\Delta t$	0.24	-0.29
SFR	-0.11	0.14

Table 2.1: Evaluation of the correlation factor, R_{corr}, between the residuals and the quantities of interest. A stronger correlation coefficient is an indication that the particular quantity is more important in influencing the scatter in the $\delta - r$ or $\Delta\mu - r$ plots.

σ_r and $\dot{f}_{acc}$ are shown in Fig. 2.10. We present the residual plots of the quantities that correlate more strongly.

Regarding $\Delta\mu$, Table 2.1 shows that there is a weak but clear anti-correlation with $\dot{f}_{\rm acc}$, followed by a positive correlation with the surface density. This is reasonable, since the primary quantity from which we extract the residuals is the radius, and since $\Delta\mu$ shows no correlation with radius in the disc proper, the direct relation of it with $\dot{f}_{\rm acc}$ is reflected in the residuals. The residual plot for $\Delta\mu$ as a function of $\dot{f}_{\rm acc}$ is shown in Fig. 2.11.

Based on the information from the residuals discussed above, we include the quantities with the strongest residual correlations alongside radius in the final parametrization.

2.4.4 Best fits

The mean evolution of δ with radius can be fit accurately with a power law of ~ 1.1 (Fig. 2.7). The power law fit is slightly preferred over a linear fit in r because it better describes the $\delta - r$ dependence in the innermost parts of the discs. Of all the secondary quantities that we consider, $\dot{f}_{acc}$ and σ_r show the strongest correlations in the residuals around the mean $\delta - r$ curve (see Table 2.1). We normalise the secondary quantities with some characteristic values to always have non-dimensional terms in the right-hand side of the parametrizations.

Our final parametrization is the combination of the power law fit to the radius and a linear fit to the secondary quantity, extracted from the residual information. Consequently, we present two possible parametrizations:

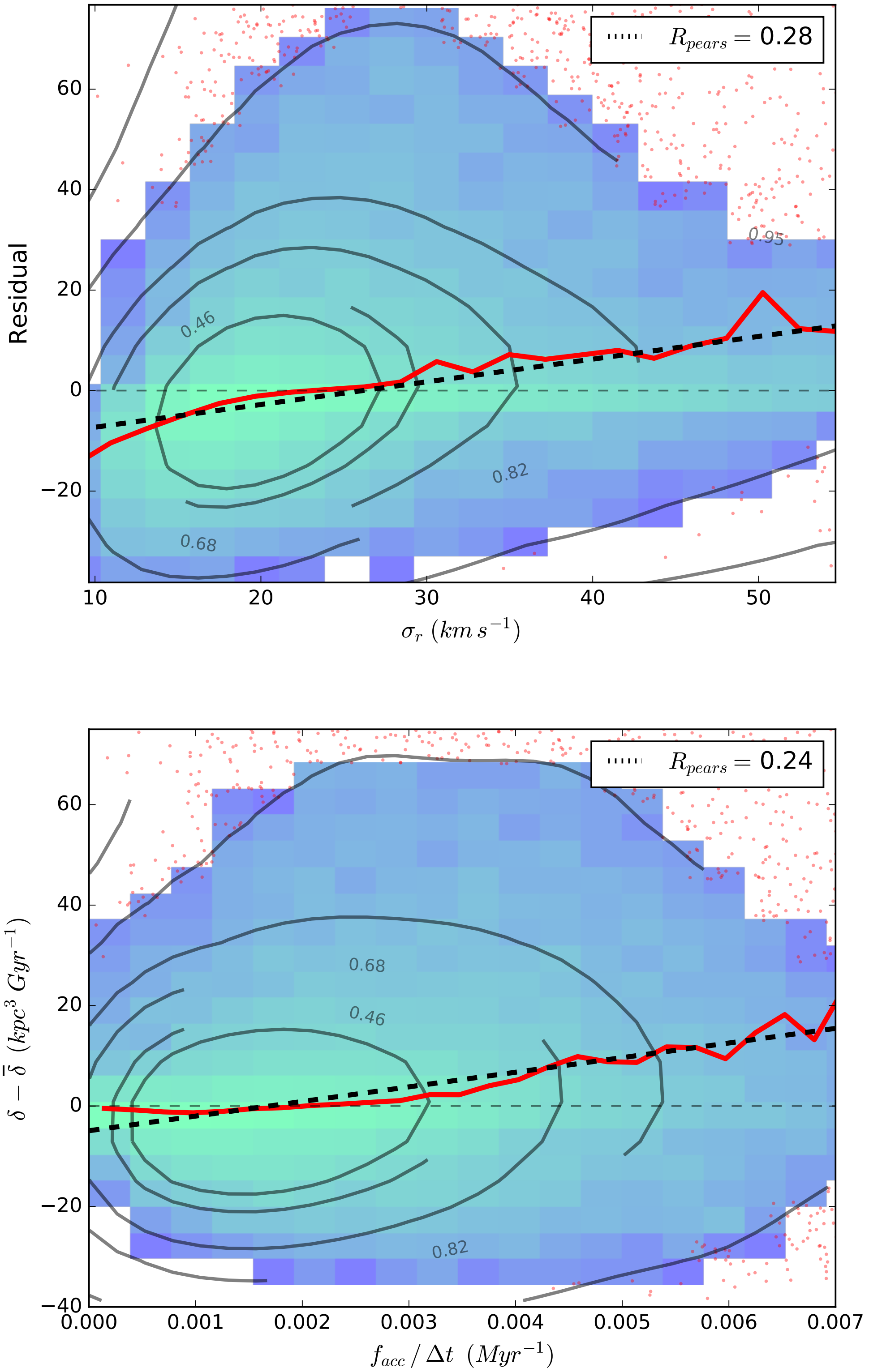

Figure 2.10: The residuals in the around the median in the $\delta - r$ plot correlate with the radial velocity dispersion of the gas. At a given radius, higher velocity dispersion of the material leads to larger values of the spread δ. Positive values for the residuals mean that at the given ring the measured spread is above the median curve of the whole sample.

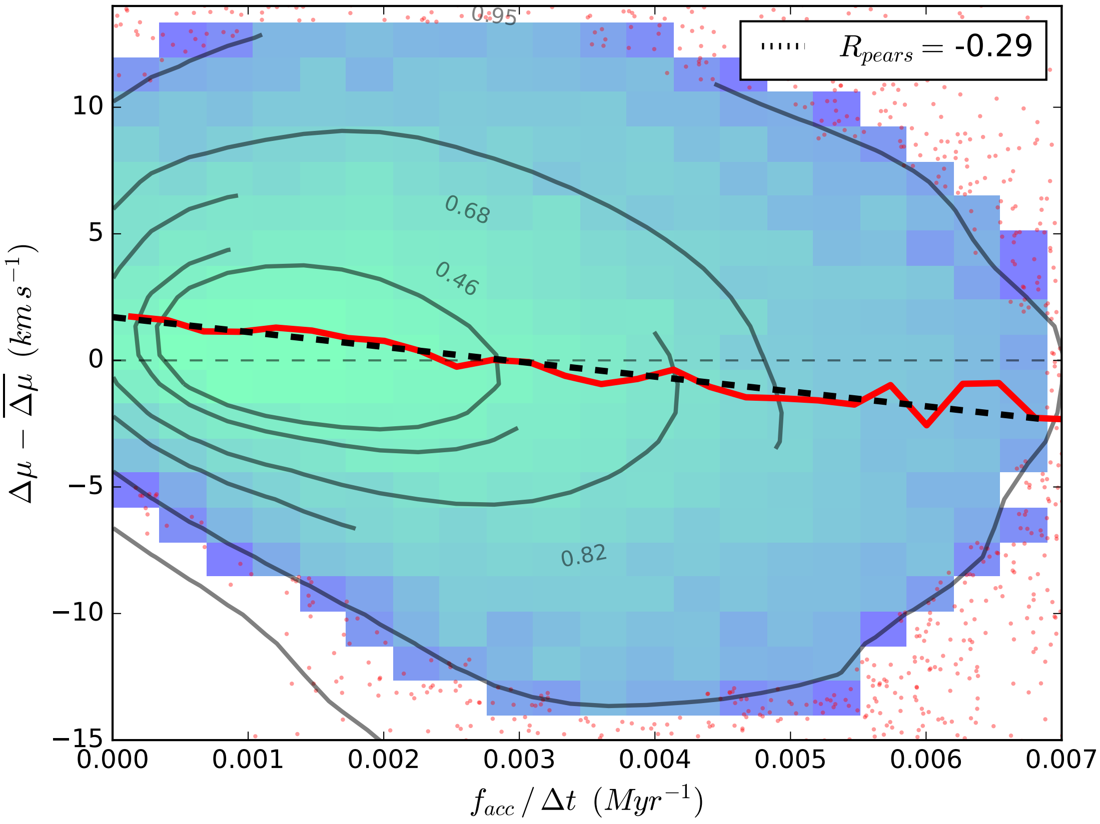

Figure 2.11: There is a weak correlation of the residuals around the mean $\Delta\mu$ with the accreted gas fraction ($\dot{f}_{acc}$), where the more gas is accreted compared to the existing gas in the ring the larger is the inflow speed.

$$\delta \; / \; \mathrm{kpc}^3 \, \mathrm{Gyr}^{-1} = 35.9 \, (r/R_{95})^{1.1} + 21.8 \left(f_{\mathrm{acc}} * \frac{60\mathrm{Myr}}{\Delta t} \right) - 2.8 \tag{2.4}$$

$$\delta \; / \; \mathrm{kpc}^3 \, \mathrm{Gyr}^{-1} = 35.9 \, (r/R_{95})^{1.1} + 14.9 \left(\frac{\sigma_r}{40 \, \mathrm{km \, s}^{-1}} \right) - 9.9 \tag{2.5}$$

In Fig. 2.12, we show the calculated δ using these parametrizations and plot it against the actual value for δ for each ring measured from the data. The median line for the dataset in this $\delta_{\mathrm{meas}} - \delta_{\mathrm{calc}}$ plot lies on the 1-1 relation (dashed black line) out to around $20 \, \mathrm{kpc}^3 \, \mathrm{Gyr}^{-1}$, as expected. The scatter around the 1-1 relation follows from the scatter around the linear fit of the residual plots.

There is a set of points for $\delta \gtrsim 30 \, \mathrm{kpc}^3 \, \mathrm{Gyr}^{-1}$ (or equivalently $w \gtrsim 1.6$) that are not well-described by the parametrization. This is a consequence of how the surface created by the parametrization traces the 3D point distribution of $r - f_{\mathrm{acc}} - \delta$ or $r - \sigma_r - \delta$. Isolating these points and trying to identify if they are caused by some specific process or depend on a given property shows no conclusive results. This is not a big concern, as these points account for less than 20 per cent of the data. They are found mostly in the outer parts of the discs and may be caused by residual merger interactions but also gas accretion.

With regards to a parametrization for $\Delta\mu$, we can fit the inner part of the disc ($r < 0.75 * R_{95}$) with a constant with respect to radius, which from the data is found to be $-2.4 \, \mathrm{km \, s}^{-1}$ and the outer part ($r > 0.75 * R_{95}$) with a linear fit indicating faster inflow speed. The value of 0.75 is found by applying the fit. The scatter around the fit is then given by the residual plots of either Δl_z or $\dot{f}_{\mathrm{acc}}$. However, Δl_z, as mentioned before, is merely a different expression of $\Delta\mu$ in the case of a flat rotation curve, so it is not very informative to build a parametrization of $\Delta\mu$ in terms of it. $\dot{f}_{\mathrm{acc}}$ can be used as a secondary parameter as it is an independently measured quantity of an external process that could potentially be a driver of the bulk flows.

For the purposes of arriving at a parametrization that can be useful in semi-analytic models, we thus arrive to the following equations:

$$\overline{\Delta\mu} \; / \; \mathrm{km \, s}^{-1} = \begin{cases} -2.4 & \text{if } r \leq 0.75 \, R_{95} \\ -15.9 \, (r/R_{95}) + 9.5 & \text{if } r > 0.75 \, R_{95} \end{cases} \tag{2.6}$$

If we further include the parameter $\dot{f}_{acc}$ to describe the scatter alongside the median relation, the above equations are modified to

$$\Delta\mu \; / \; \mathrm{km \, s}^{-1} = \\ = \begin{cases} -1.7 - 6.8 \, (f_{\mathrm{acc}} \, \frac{60\mathrm{Myr}}{\Delta t}) & \text{if } r \leq 0.75 \, R_{95} \\ -15.9 \left(\frac{r}{R_{95}} \right) - 6.8 \, (f_{\mathrm{acc}} \, \frac{60\mathrm{Myr}}{\Delta t}) + 10.2 & \text{if } r > 0.75 \, R_{95} \end{cases} \tag{2.7}$$

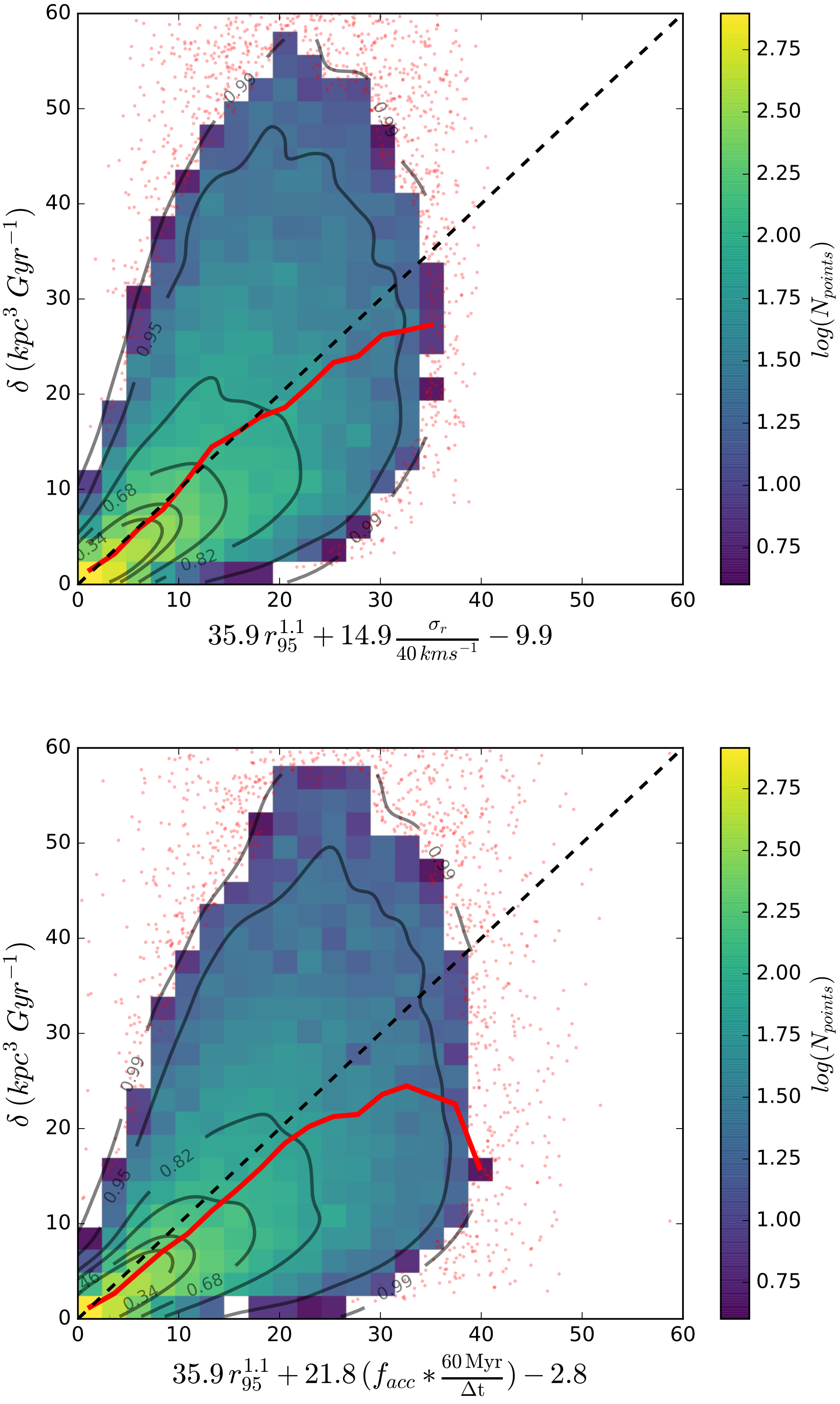

Figure 2.12: The selected parametrizations for the quantity w, using two different sets of parameters, radius - accreted gas fraction (left) and radius - radial velocity dispersion (right). In these plots the data should be lying around the one-to-one relation if the fitting is ideal. This line is plotted for reference (dashed). The red line is the median of the data which for the most part agrees well with the dashed line.

These parametrizations give a most accurate description in the regime of values $-10 < \Delta\mu < 0$, which contain the majority of points, but are not representative for cases with $\Delta\mu > 0$, where we have radial outflow of the material.

2.5 Discussion

We have identified the accreted gas fraction, $\dot{f}_{acc}$, and gas velocity dispersion, σ, as the two main parameters driving variations in gas spread, w (or its timestep-invariant equivalent, δ), with radius in the Auriga simulations. On physical grounds, σ in a given ring is partially a measure of the total internal kinetic energy and the amount of turbulence that is present in the gas. This is the case no matter which mechanism injected the energy into the system, be it for example kinetic heating from some interaction or stellar feedback. Furthermore, as we study radial motions, the radial component of the dispersion, σ_r, is expected to be more dominant. Studies like Forbes et al. (2014) and Yang & Krumholz (2012), modelling the diffusion of metals in the disc, suggest diffusion coefficients scaling with the velocity dispersion of the gas multiplied with the scale height of the disc. We have tested whether such a quantity ($\sigma_g h_g$) shows any relation with the spread measure δ and we find that it yields similar strength of correlation to the residuals to when simply using σ_g as a parameter.

The accretion process is also very relevant to the radial motions, as has also been shown in earlier studies (Pezzulli & Fraternali, 2016). The accretion rate of new gas could also be a candidate parameter but we found that $\dot{f}_{acc}$ correlates better with w and δ. Besides, $\dot{f}_{\rm acc}$ carries more information, as it is a measure of both the material entering the ring and the material already present. We could connect the effect of the accreted gas to the radial motions by considering that larger amounts of accreted material result in more kinetic energy that can be converted into turbulence, leading to larger random radial motions which then translate to the larger values of δ. Especially at the outer, lower-density regions of the disc, turbulence can dominate the energy density, as low-density gas has less inertia and responds more readily to perturbations from the external material.

The fact that w scales as $w \sim \Delta t^{1/3}$ is not straightforward to justify. In a simple diffusive process, where gas diffuses out of the initial ring to lower density regions, we would expect a $w \sim \Delta t^{1/2}$ dependence. The cubic power that we find instead gives a better fit, suggestive of a process slower than pure diffusion. The overall radial spread of the gas in the disc is likely the result of a combination of physical processes, some of which are of diffusive nature, that are active during the disc evolution within the disc plane. On top of this, it must be noted that the cubic power is the average of all the data in the 14 different halos and over the whole redshift range that we use. Thus, we cannot clearly state why $w \sim \Delta t^{1/3}$, but only acknowledge that this time dependence better brings the data from different snapshot spacings in agreement.

The radial dependence of $\Delta\mu$, the bulk flow, as seen in Fig. 2.4, can be explained by two separate regimes in the disc. The regime where we observe a nearly constant radial dependence with inflow a few km s^{-1}, and the one where there is inflow with much larger velocities, increasing as we head in the outer parts of disc. In the first case, we are essentially describing the equilibrium part of the disc where the material has settled in more regular motions and is rotationally supported.

In the second case, we are in a regime where we have significant accretion of new material, coming in as patchy accretion in many cases. These blobs of gas can travel relatively unimpeded until they encounter the comparatively higher densities at the edge of the star forming disc. Fig. 2.13 shows evidence for this statement, as beyond $\sim 0.75R_{95}$ we find higher f_{acc} values and a steeper slope in its radial profile. Goldbaum et al. (2016) have calculated the time-averaged radial gas mass flux in their simulated galaxy, finding a radial profile that points to a net inflow with little radial evolution in the absolute value of the flux, which can be consistent with the radial profile that we find for $\Delta\mu$. Aside from these two regimes, we also attribute the surplus of positive (outflowing) $\Delta\mu$ values at $r \lesssim 0.1$ to AGN feedback, which empties of gas the innermost regions of galaxies with active black holes. This effect appears strongly only in 3 halos in the sample, for specific timespans, so does not significantly alter our conclusions. We must also notice that the constant value that we find in the inner parts for the inflow is representative of the set of the halos that are available in Auriga and is likely limited to the specific mass range. We have no indication that is a value that can be generalised to very different galaxy mass regimes.

The range of values that we find for $\Delta\mu$ are consistent with the observational data from Schmidt et al. (2016) where they find that most of their data points are within ± 15 km s^{-1}. The exact radial flow speed profiles presented in this paper may not necessarily match the average radial profile we show in Fig. 2.4 but this is expected as we present the compilation of all the data for a large number of snapshots. The galaxies used in Schmidt et al. (2016) show an object-to-object variability with strong inflows or outflows at given objects exceeding ± 30 km s^{-1} and at different radii. This is also true in our simulations if we look at specific snapshots where we have instances of extreme inflows or outflows, comparing to the average, with no clear radial trend. Concerning the values of the spread w, it is much harder to test against observations since it is not a directly measurable quantity in observational data.

The $\Delta\mu$ parametrization we provide describes the average behaviour we observe over all halos in the suite. As seen from the data, there are many instances where tracers move on average outwards between two snapshots. This is not captured in the best fit, which gives only a time-averaged representation. The correlation with Δl_z shows us that the gas moves inwards or outwards because its angular momentum has been altered. This indicates the presence of a torque that has driven this loss or gain. However, identifying the source of this torque, and more importantly reliably connecting it with the movement of gas, is a difficult proposition. One possibility is the presence of spiral arms that by interacting with the gas can input or remove angular momentum from it.

Both Krumholz et al. (2018) and Goldbaum et al. (2016) discuss the relevance of the Toomre Q parameter in radial flows, and although we have examined the Q values for our model discs, we found no convincing dependence between them and $\Delta\mu$ or δ but only weak correlations with a lot of scatter and driven by high values of Q. Given that in the Krumholz et al. (2018) model and its variants, Q is often set to a constant value, or subject to a floor value, we should not necessarily expect a correlation but the lack of it means that we cannot use Q in the way we construct the parametrizations. All in all, we do not rule out the importance of gravitational instability as a source of turbulence, but rather suggest that the ring analysis we perform may not capture this effect. Further, the ISM model in the Auriga simulations, which is designed to prevent clump formation and generally yields higher Q values, is not conducive in resolving perturbations from

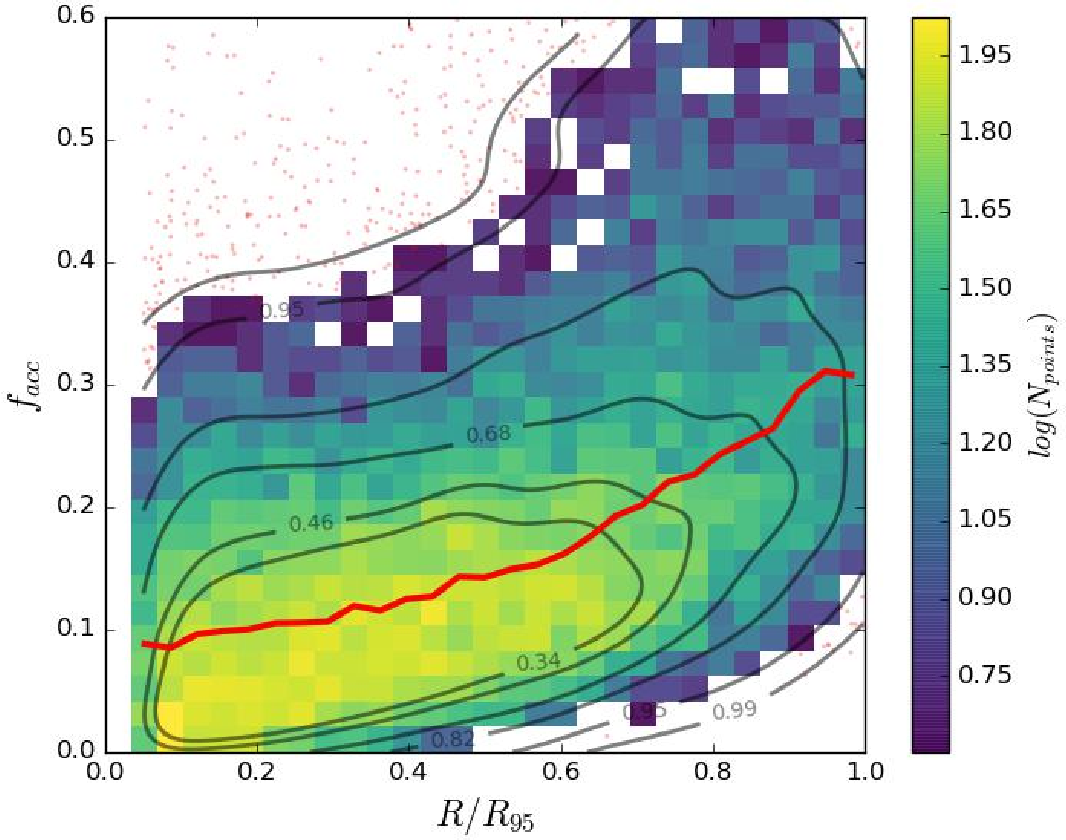

Figure 2.13: Radial dependence of the accreted gas fraction. At the outer parts of the discs, beyond 70% of the disc radius, we have larger contribution from the accreted material.

gas clumps that could be a main physical reason underlying any dependence on Q.

We have tested the resolution dependence on one of our halos that was re-simulated with lower resolution, to evaluate the consistency in the results that we obtain. The results between the two resolution simulations of this single halo are mostly consistent within the error, but the lower resolution simulation shows overall higher values for w (on average 1.3 times higher) with the effect being more pronounced in the very inner radii where also $\Delta\mu$ appears to deviate from the fiducial run. In other words, at lower resolution, with a lower number of tracers (similar number of tracers per cell but lower amount of cells overall), the tracers appear more diffusive. In general, gas flows are less well captured in the lower resolution simulation because of the low number of tracers that sample the cold gas. This is shown in Fig. A.3 in Appendix A.

Further it must be noted that by using ring-like annuli in our analysis we smooth out any azimuthal variation in the two quantities we study. For example, the presence of a strong bar can lead to material funneling to the centre at particular azimuthal angles but being expelled in another direction. This information in a given ring is captured in the spread δ, resulting in a symmetric distribution but the median bulk flow $\Delta\mu$, being the average value of the speeds of inflowing and outflowing material, will be lower than if we look at the speed of material in a particular direction.

We see a small difference in the merger history between the 6 higher-mass $(1-2\times10^{12}M_{\odot})$ and the 8 lower-mass $(0.5-1\times10^{12}M_{\odot})$ halos. In almost half of the lower-mass haloes, there are mergers and encounters even at later stages, whereas the higher-mass ones are relatively quiet. This may indicate that the higher-mass sample is in a slightly different evolutionary stage, but this does not seem to influence the conclusions for the properties that describe the radial flows.

As a final remark, we acknowledge that the simulations do not explicitly model the small-scale turbulence generated by stellar feedback and could impact the radial movement of the tracers on small scales, but that the effective pressure applied by the sub grid model provides some similar effect to the turbulent pressure in star-forming gas. Getting a better understanding of these effects would require simulations that explicitly model the multi-phase ISM, which is beyond the scope of this work.

2.6 Conclusions

We have performed an analysis of the gas kinematics in disc galaxies in the Auriga simulation suite. We have focused only in the ‘quiet’ phases of the disc evolution, excluding the snapshots when the discs have a violent merger. In our method, we examine the disc in a local fashion, by considering a ring of gas at a given radius. We describe the radial flows of gas with two parameters; the median bulk flow, $\Delta\mu$, and radial spread, w, of the gas in each ring. We have identified $\delta = w^3/\Delta t$ as a timestep invariant quantity. As the radius increases, we observe an increase in w and hence δ, indicating that tracers in the outer regions diffuse out of the initial ring more effectively than in the inner regions. This can be attributed to the lower densities (of gas and stars) or the larger accretion rates observed at larger radii. The bulk flows expressed by $\Delta\mu$ have a flat radial dependence in the inner parts of the disc, whereas in the outer parts we observe increased inflow speeds. Both quantities appear to be closely connected to the amount of accreted material in the disc, as expressed by the accreted mass fraction $\dot{f}_{acc}$. We have presented parametrizations of $\Delta\mu$ as a function of radius r and $\dot{f}_{acc}$, differentiating between the inner disc (equilibrium region) and outer disc (accretion-dominant region). For δ, our parametrizations are expressed as functions of radius and a secondary parameter which is either $\dot{f}_{acc}$ or the radial velocity dispersion of the gas σ_r. In combination, these two quantities describe the process of gas mass exchange in different radii inside discs. Since we have not yet tested how the results of this study apply to models, we choose to present several different parametrizations that arise from our data, with a goal of checking their performance in the future.

Chapter 3

Stellar migration in the Auriga simulations

3.1 Introduction

During the lifetime of a star its orbital radius within the galactic plane is subject to changes that can result in the star inhabiting a radius different than the one it was born at, a concept referred as stellar radial migration (e.g. Lynden-Bell & Kalnajs, 1972). There are two terms that are widely discussed in the literature, describing two entirely distinct types of stellar migration, 'churning' and 'blurring' (Schönrich & Binney, 2009).'Churning' refers to the direct change of the guiding centre, the mean radius of the stellar orbit, and relates to permanent changes in the orbital angular momentum without changing the "random" component of its orbital energy (e.g. Grand et al., 2012b). 'Blurring' is associated with temporary changes in the orbital kinetic energy close to peri/apo-centre (thus away from the mean orbital radius), while the angular momentum remains constant. There are several mechanisms that are responsible for inducing these changes in the orbital radii, including non-axisymmetric features in the galactic disc, such as a bar (e.g. Halle et al., 2018), transient spiral arms (e.g. Sellwood & Binney, 2002) and interactions with giant molecular clouds (GMCs). Furthermore, minor mergers with satellite systems have also been explored as drivers of radial migration (e.g. Quillen et al., 2009). However, disentangling all of these mechanisms is a far from trivial task.

Radial migration has been invoked in order to potentially explain many observables in the Milky Way, such as planar dynamical streams (Kawata et al., 2018; Hunt et al., 2018), the large spread of stellar metallicities (e.g. Nordström et al., 2004; Haywood, 2008; Kubryk et al., 2013; Minchev et al., 2013; Grand et al., 2015) and the presence of supersolar metallicity stars (Kordopatis et al., 2015) in the solar neighbourhood as well as the large scatter in the age-metallicity relation (Casagrande et al., 2011), although recent studies (Haywood et al., 2013; Bergemann et al., 2014; Walcher et al., 2016) point to an age-metallicity anti-correlation especially for stars older than $\sim$ 9 Gyr. Additionally, migration is a possible mechanism that may explain disc truncations and the upturn of age gradients observed in the outer regions of galaxies (e.g. Bakos et al., 2008; Roškar et al., 2008; Radburn-Smith et al., 2012; Ruiz-Lara et al., 2017; Herpich et al., 2017) and the bi-modality in the [α/Fe]-[Fe/H] relation in the Milky Way, which has been studied both from an observational (Fuhrmann, 1998; Haywood et al., 2013; Anders et al., 2014;

Nidever et al., 2014; Hayden et al., 2015) and theoretical (Schönrich & Binney, 2009; Brook et al., 2012; Minchev et al., 2014; Grand et al., 2018; Mackereth et al., 2019; Clarke et al., 2019; Buck, 2020; Renaud et al., 2021; Khoperskov et al., 2021) perspective. Radial migration has been linked also to the formation of the geometrically-defined galactic thick disc (Loebman et al., 2011; Solway et al., 2012; Vera-Ciro et al., 2014) and shaping vertically "flared" distributions of coeval stellar populations (e.g. Minchev et al., 2015). However, there is also contrasting evidence that stellar migration is ineffective in thick disc formation and rather contributes to cooling the disc in the cosmological context (Minchev et al., 2012b, 2014; Grand et al., 2016; Ma et al., 2017). Observational studies of the migration process are non trivial, since it is not possible to get direct information about the initial (birth) conditions of a single star's orbit. Rather, migration can be inferred indirectly from measuring metallicity and age gradients and identifying different regions in the age-metallicity plane. One useful tracer of stellar migration in the Milky Way are stellar clusters. Netopil et al. (2022) used the ages and metallicities of a number of open clusters to measure metallicity gradients and inferred a mean migration rate of $1\,\mathrm{kpc/Gyr}^{-1}$ for younger objects and half of this value for older objects.

Radial migration has been consistently studied in chemodynamical models of disc galaxies that aim to reproduce the observed age-metallicity relations and the radial gradients of these quantities in the solar neighbourhood. In models such as Sellwood & Binney (2002) and Minchev et al. (2014), radial migration is treated using self-consistent angular momentum redistribution from an N-body disc, whereas Schönrich & Binney (2009) and Kubryk et al. (2013, 2015) add prescriptions that describe separately the churning and blurring processes. In their chemodynamical model, Frankel et al. (2018) introduce an analytic formulation for stellar migration that follows a Gaussian diffusion process where older stars spread to increasingly larger radii from their birth radius. In their formulation, the overall shape of the Gaussian function is regulated by a single migration strength parameter. APOGEE data was used to fit the best parameters for their model (Majewski et al., 2017). In a later study (Frankel et al., 2020), their model was expanded to study the effect of churning and blurring separately, concluding that churning has an order of magnitude stronger effect than blurring. Johnson et al. (2021) use data from a numerical simulation and test different prescriptions for their chemodynamical model to study the migration process, in a similar way to Minchev et al. (2013).

Similarly, several studies have been carried out using numerical simulations to study the presence and strength of the migration process in simulated disc galaxies. These studies can be split between those of relying on isolated disc systems (e.g Di Matteo et al. 2013; Aumer et al. 2016; Halle et al. 2018; Mikkola et al. 2020) and those that analyse discs embedded in a cosmological environment using zoom-in simulations (e.g Martig et al. 2014; Grand et al. 2016; Buck 2020). The advantage of the former is that they can isolate and study in a controlled setup the effect of non-axisymmetries forming during the lifetime of the disc have on the stellar orbits. The latter, though, create a more realistic analogue of a real galaxy where the deviation of the positions of stars from their birth radii is the cumulative result of not only all the angular momentum changes induced by bars or spiral arms but also by any merger events that may have happened to the particular system.

Minchev & Famaey (2010) explored the combined effect arising from overlapping resonances when both a bar and spiral arms are present in a simulated disc. Minchev et al. (2012a) concluded from their numerical simulations that the effect of bars is dominant with regards to stellar migration compared to the effect of transient spiral arms, and also confirm the importance of migration for the flattening and reversal of age gradients in the disc outskirts which are found to be populated by stars that have transferred outwards from the inner parts of the disc. Similarly, Agertz et al. (2021) confirmed that metal rich stars preferentially migrate from inner to outer regions in their simulated Milky Way galaxy, affecting the metallicity distribution function around the solar neighbourhood. Finally, Verma et al. (2021) applied sophisticated forward-modelling techniques to halos from the Auriga cosmological simulations to put constraints on the strength of migration based on measures of the metallicity dispersion at the Solar cylinder.

In this project, we study the process of radial migration of stars in a number of different Milky Way-mass halos from the high-resolution cosmological zoom-in simulation suite Auriga (Grand et al., 2017), which includes environmental effects such as mergers and gas accretion. We study the total migration of the stars over their lifetime, measure the migration strength in each galaxy model, and also compare the simulated profiles of age and metallicity with fictitious profiles that would result if there was no evolution in the positions of the stellar particles. In a separate analysis we look at the migration of stars between different output snapshots of the simulations, and we arrive at a simple parametrization for the stellar radial migration in Auriga that can be easily incorporated into (semi-)analytic models of galaxy evolution.

This chapter is structured as follows. In Section 3.2, we briefly review the simulation suite we use for this study. In Section 3.3 we analyze the strength of migration from the perspective of the birth radius of stars, while in Section 3.4 we focus on the rate of migration by comparing stellar positions in subsequent simulation outputs. Finally, we give a discussion or our results and summarize our conclusions in Section 3.5.

3.2 Simulations

We make use of the Auriga suite of high-resolution, magneto-hydrodynamical cosmological "zoom-in" simulations (Grand et al., 2017) which are designed to reproduce Milky-Way analogue disc galaxies in the concordance ΛCDM cosmology. We select a total of 17 Auriga halos; 9 halos from the original runs of the project with a halo mass[1] ranging between $1-2\times10^{12}\,\mathrm{M}_\odot$, and 8 halos of a recent lower mass extension in the range $0.5-1\times10^{12}\,\mathrm{M}_\odot$ (Grand et al., 2019).

These halos were originally selected based on a mild isolation criterion in the $z=0$ snapshot of the dark matter-only counterpart to the cosmological EAGLE simulation of co-moving side length $67.8\,h^{-1}$cMpc (L100N1504) presented in Schaye et al. (2015). The values of the cosmological parameters for these simulations are $\Omega_m=0.307$, $\Omega_b=0.048$, $\Omega_\Lambda=0.693$, $H_0=100\,h\,\mathrm{km\,s^{-1}\,Mpc^{-1}}$ and $h=0.667$, taken from Planck Collaboration (2014).

The zoom simulations are initialized at redshift $z=127$ with the high-resolution regions having a mass resolution of $\sim5\times10^4\,\mathrm{M}_\odot$ per baryonic element and a comoving softening length of $500\,h^{-1}$pc. The physical softening length grows until $z=1$, after which time it is kept fixed.

---

[1] Defined to be the mass inside a sphere in which the mean matter density is 200 times the critical density of the Universe, $\rho_\mathrm{crit}=3H^2(z)/(8\pi G)$.

The physical softening value for the gas cells is scaled by the gas cell radius (assuming a spherical cell shape given the volume), with a minimum softening set to that of the collisionless particles.

Unlike in EAGLE, the time evolution in Auriga is carried out with the quasi-Lagrangian magneto-hydrodynamics simulation code AREPO (Springel, 2010; Pakmor et al., 2016; Weinberger et al., 2020), using the galaxy formation model outlined in Grand et al. (2017) that accounts for the most important physical processes relevant for galaxy formation and evolution. In AREPO, gas cells are modelled with an unstructured mesh in which gas cells move with the local bulk flow. This numerical approach combines the accuracy of a mesh-based representation of hydrodynamics with the geometrical flexibility and low advection errors of a Lagrangian treatment.

3.2.1 Included galaxy formation physics

The physical processes incorporated into Auriga's galaxy formation model include primordial and metal-line cooling (Vogelsberger et al., 2013), as well as an externally imposed spatially uniform UV background for modelling cosmic reionization. The star-forming interstellar medium (ISM) comprises gas that has become denser than 0.11 atoms cm^{-3} and is modelled by a subgrid model that describes a two phase medium of cold clouds embedded in a hot volume filling phase (Springel & Hernquist, 2003) assumed to be in pressure equilibrium.

Stellar particles are spawned stochastically from the gas using a Schmidt-type star formation prescription with a gas consumption timescale calibrated to observed star formation densities. Each particle represents a Simple Stellar Population (SSP) characterised by properties such as its age, mass and metallicity. The stellar evolution model applied to each SSP follows type Ia supernovae (SNe-Ia) and winds from Asymptotic Giant Branch (AGB) stars that return mass and metals (9 elements are tracked: H, He, C, O, N, Ne, Mg, Si and Fe) to the surrounding gas. Supernovae type II (SNe-II) are also assumed to return mass and metals, but are treated with an instantaneous recycling approximation.

Galactic winds from SNe-II are modelled by a wind particle scheme mediating non-local kinetic feedback (Vogelsberger et al., 2013), which effectively models the removal of mass from star-forming regions and deposits mass, momentum and energy into adjacent gas in the circumgalactic medium with density lower than 5% of the density of star-forming gas. These winds are an important feedback channel for regulating the total stellar mass forming in the galaxies.

In addition, there are prescriptions in the model accounting for the accretion of matter onto black holes and energetic feedback from Active Galactic Nuclei (as described in Grand et al., 2017). Also, magnetic fields are seeded at $z = 127$ with a co-moving field strength of 10^{-14} cG (Pakmor et al., 2014), and are subsequently amplified by small-scale dynamo processes during the simulations. While several studies have shown that the resulting magnetic field strength evolution and radial profile in Milky Way-like halos are in good agreement between Auriga and observational findings (e.g Pakmor et al., 2017, 2018, 2020), they play only a minor role for the regulation of star formation in Auriga, and thus are probably of negligible influence on the stellar migration rates. Similarly, the impact of central supermassive black holes is probably minor, at least in the outer part of discs, whereas their feedback can indirectly have an impact in the inner regions through influencing the mass of the stellar bulge and bar properties (see Irodotou et al., 2022).

In our runs, we have 252 time-slice outputs (‘snapshots’) down to redshift $z = 0$, with a median time resolution of ~ 60 Myr between two consecutive snapshots (the time interval ranges between 45-75 Myr). Between the different simulated galaxies, we observe a variety of structural properties, with nearly half of them developing a bar at some point in their evolution. In addition, the discs have varying merger histories, with the lower-mass halos experiencing more significant merger events at lower redshift, whereas the higher-mass ones have no significant mergers in the last 3 Gyr of the simulation.

3.2.2 Galactic properties

In Table 3.1, we summarize some of the $z = 0$ properties of the 17 simulated galaxy discs which we consider relevant in this study. Halos belonging to the lower halo mass simulations are named with prefix ’L’. The stellar masses in the Table refer to the mass enclosed within 2 kpc of the disc plane and within 20 kpc in galactocentric radius and ranges between $10 < \log(M_*/\mathrm{M}_\odot) < 11$. We also report the radii which enclose 50 per cent (R_{50}) and 90 per cent (R_{90}) of the disc stellar mass. Because our discs have a variety of sizes, we use scaled radii in the presentation of many results in the next sections. We have tested three options for the scaling, (1) the disc scale length taken from the slope in a power law fit of the stellar density, (2) R_{90} and (3) R_{50}. R_{90} and R_{50} have the advantage that they do not require a fitting, which can come with an error, so are more trustworthy in using them as scaling factors of the radii. R_{90} has slightly more stable time evolution but all the results are qualitatively equivalent if we use R_{50} instead.

Additional quantities include the mean stellar age at $z = 0$, and information about the stellar kinematics such as the mean stellar velocity and velocity dispersion. We also measure the A2(r) coefficient of the Fourier decomposition of the planar (x-y) stellar surface density (its maximum value at $z = 0$ reported in Table 3.1). This is a measure of the strength of the non-axisymmetry at any given radius, and its peak value is usually taken as the strength of the bar in the galaxy. In Fig. 3.2, we show in more detail the radial profiles of the A2 coefficient for each halo at different selected lookback times. Some of our halos have a very strong bar for most of their lifetime with values of A2 > 0.3.

On top of the global disc properties, we also track the properties of individual stellar particles at any given snapshot which include their masses, positions, velocities, ages and metal content and we also have information about the birth radius of each star which is a useful quantity in this study.

In Fig. 3.1 we present stellar projections at $z = 0$ where the radial extent of each disc, the presence or not of the bar and the presence of spiral arms can be visually examined. The colours are composites of the g,r and i filters.

Name	$\log(M_*/\mathrm{M}_\odot)$	R_{50} (kpc)	R_{90} (kpc)	$\mathrm{A2}_{max}$	$\langle t_{*,\mathrm{age}} \rangle$ (Gyr)	$v_{rot,max}$ (km s^{-1})	$\langle v_* \rangle$ (km s^{-1})	σ_* (km s^{-1})	$\langle v_* \rangle / \sigma_*$
halo_5	10.81	3.31	11.46	0.421	5.4	265.4	231.2	74.4	3.11
halo_6	10.63	6.42	14.65	0.18	6.3	209.7	187.2	55.5	3.37
halo_9	10.81	2.83	8.4	0.449	6.3	276.3	241.9	81.5	2.97
halo_13	10.66	3.11	7.8	0.208	4.4	245.2	218.5	72.3	3.02
halo_17	10.88	1.71	9.24	0.498	6.8	345.1	275.2	98.3	2.8
halo_23	10.87	6.52	15.02	0.198	6.3	256.7	229.8	71.2	3.23
halo_24	10.79	4.59	15.71	0.503	7.0	246.0	212.8	70.7	3.01
halo_26	10.95	4.21	12.42	0.501	5.9	288.5	256.6	82.1	3.13
halo_28	10.93	3.25	8.58	0.301	4.5	299.8	270.3	90.0	3.0
halo_L1	10.05	5.07	13.88	0.097	4.4	150.8	125.6	47.1	2.67
halo_L2	10.20	3.85	13.46	0.319	5.1	161.7	145.9	62.3	2.34
halo_L3	10.45	4.05	12.32	0.308	6.2	200.5	177.8	69.5	2.56
halo_L5	10.13	4.31	12.0	0.157	5.6	167.5	139.4	55.5	2.51
halo_L7	10.36	3.95	13.9	0.089	5.2	172.6	153.8	47.4	3.24
halo_L8	10.59	4.55	11.28	0.307	5.2	210.8	185.8	60.2	3.09
halo_L9	10.32	3.77	10.88	0.311	7.0	168.8	149.1	44.3	3.37
halo_L10	10.42	3.75	12.56	0.254	7.1	189.7	168.1	65.5	2.57

Table 3.1: Properties of the different galactic discs at $z = 0$. We show in order the stellar mass enclosed within 2 kpc from the plane and 20 kpc in radius (M_*), characteristic radii of 50% and 90% of the stellar mass (R_{50}, R_{90}), the maximum A2 coefficient, mean stellar age ($\langle t_{*,\mathrm{age}} \rangle$), maximum rotational velocity ($v_{rot,max}$), mean stellar velocity ($\langle v_* \rangle$), stellar velocity dispersion (σ_*), and the ratio of the velocity to the velocity dispersion.

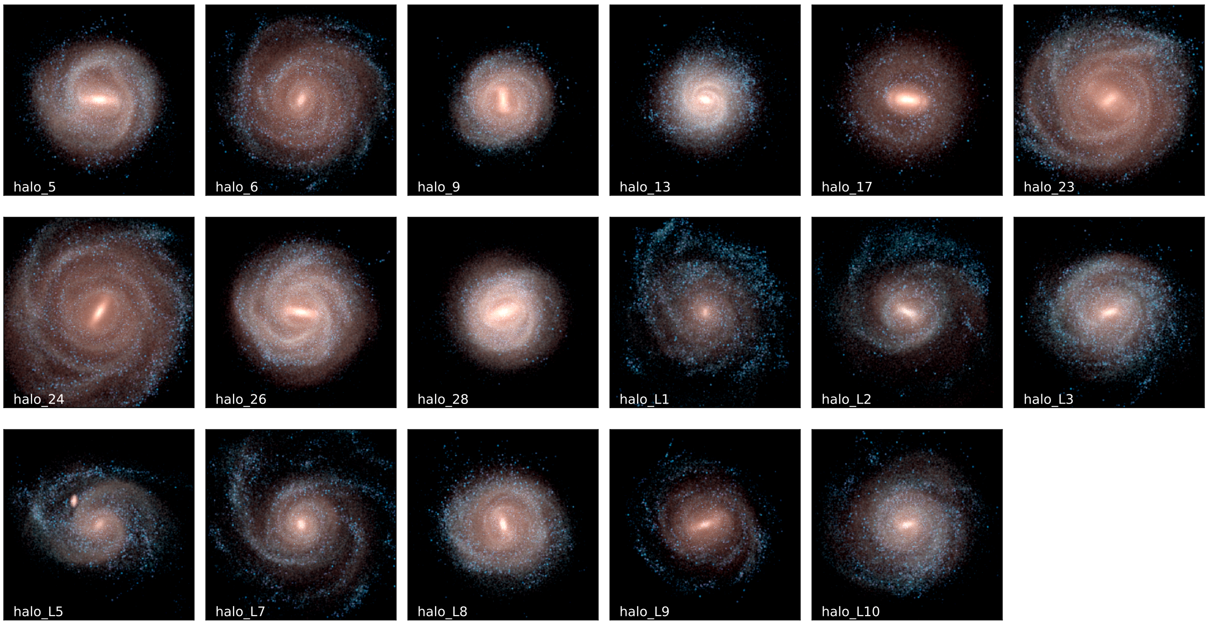

Figure 3.1: Stellar projections at $z = 0$. The images are composites of the r, g , and i filters, and are rotated into the x-y plane of the disc. The extent of all panels is 25×25 kpc.

3.3 Migration from the birth radius

Similar to previous stellar migration studies, we look at the change in the galactocentric radius of stars between their birth time and the final snapshot of the simulation at $z = 0$. We select all the stars in the disc at $z = 0$, under the condition that they (a) have a circularity parameter of $\epsilon > 0.7$, to probe the cold stellar disc and exclude the bulge component, (b) are within 2 kpc of the galactic plane, and (c) are within 20 kpc from the centre of the galaxy. Furthermore, we only include stars that have been born in the main halo and not those that are accreted from other systems.

3.3.1 Overall changes in radius

A first direct measurement from the simulation data is the computation of the overall change in radius, $\Delta R = R_{z=0} - R_{\mathrm{birth}}$, for each star. Fig. 3.3 shows that, if we take the average of this value, $\langle \Delta R \rangle$, for all the stars selected as part of the disc, we find that in all our systems we get values that are very close to 0. In the same figure, we show the average of the *absolute* value of ΔR, $\langle |\Delta R| \rangle$, which for all our systems has values of around 1-3 kpc. In contrast to our findings, El-Badry et al. (2016) find consistently positive values for $\langle \Delta R \rangle$ as well as higher values for $\langle |\Delta R| \rangle$ in similar plots. It should be noted however that they probe a very different mass range in their study and a different mechanism of migration due to stellar feedback.

In Fig. 3.4 we compute the same average but instead selecting only stars that at $z = 0$ are either inside or outside the half mass radius of the galaxy. We find that stars that are in the outer

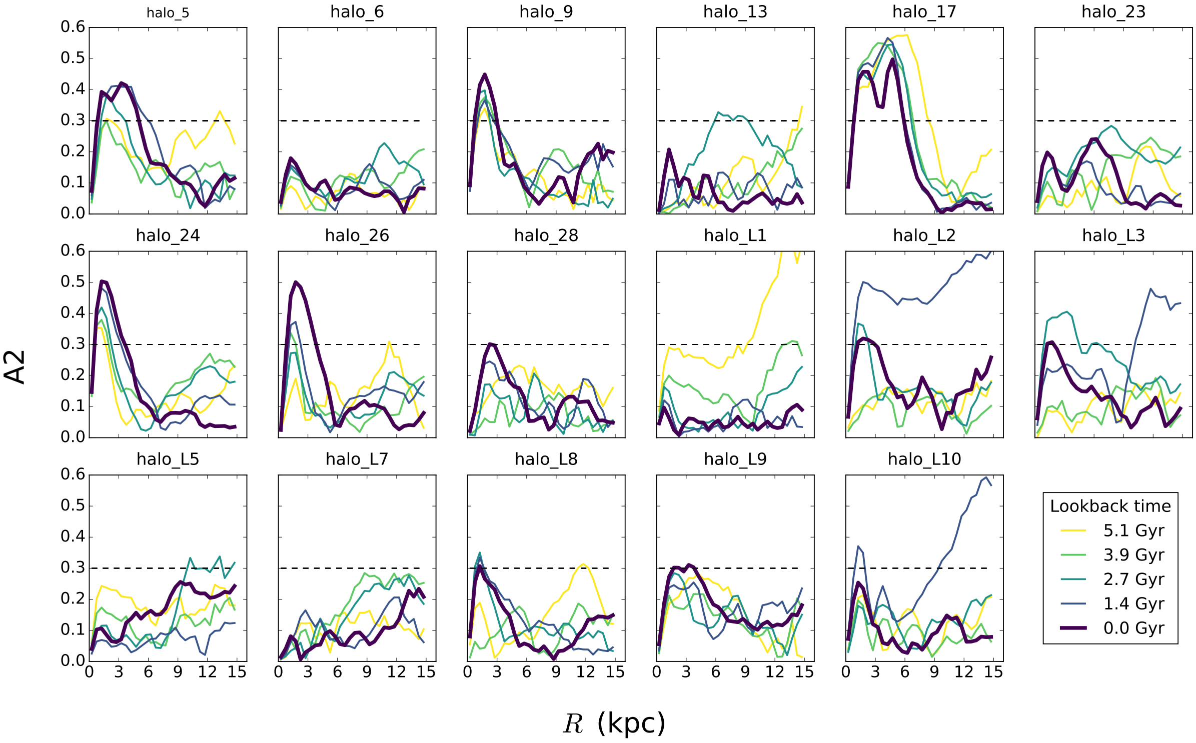

Figure 3.2: Measurements of the A2 coefficient in different radii as an indicator of bar strength for our systems at several different lookback times (shown with the different color curves). The bold purple line is the measured at $z = 0$. A strong bar is considered to be present when A2 has values above 0.3 in the inner radii.

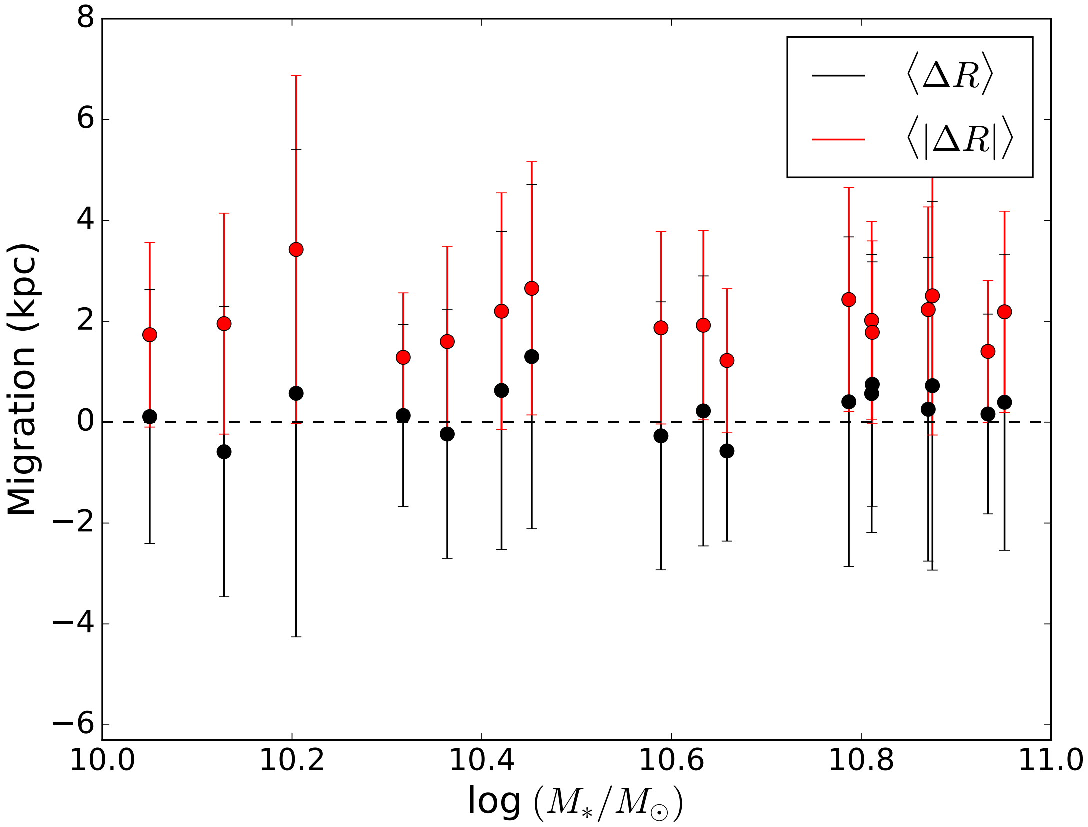

Figure 3.3: Mean change between the birth radius and the galactocentric radius at $z = 0$, $\Delta R = R_{z=0} - R_{\rm birth}$, for all disc stars and for all the systems in our sample plotted against the stellar mass at $z = 0$. The black points show the average of the difference and the red the absolute value of the same quantity. The mean migration is very close to zero for all the systems.

radii at $z = 0$ have on average positive ΔR, meaning that they have migrated outwards during their lifetime. The opposite is true for the stars that are within R_{50} by $z = 0$, which have a mean inwards migration.

Figs. 3.3 and 3.4 illustrate the combined effect of stars migrating both inwards and outwards within the disc, with a mean absolute migration scale in the range of a few kpc. This indicates significant mixing of material with different properties from the exchange of stars from inner and outer regions. We also see that there are no variations with the stellar mass of the system in our narrow mass range.

We further look into the differences between the birth and final radii of stars by comparing directly the birth and final radii for stellar particles in each of our discs separately. In Fig. 3.5 we plot these two quantities against each other for the 17 indivdual systems. We find that most of the distributions are reasonably symmetric around the one-to-one lines, confirming the presence of both inwards and outwards moving migrators in roughly equal numbers, as also confirmed

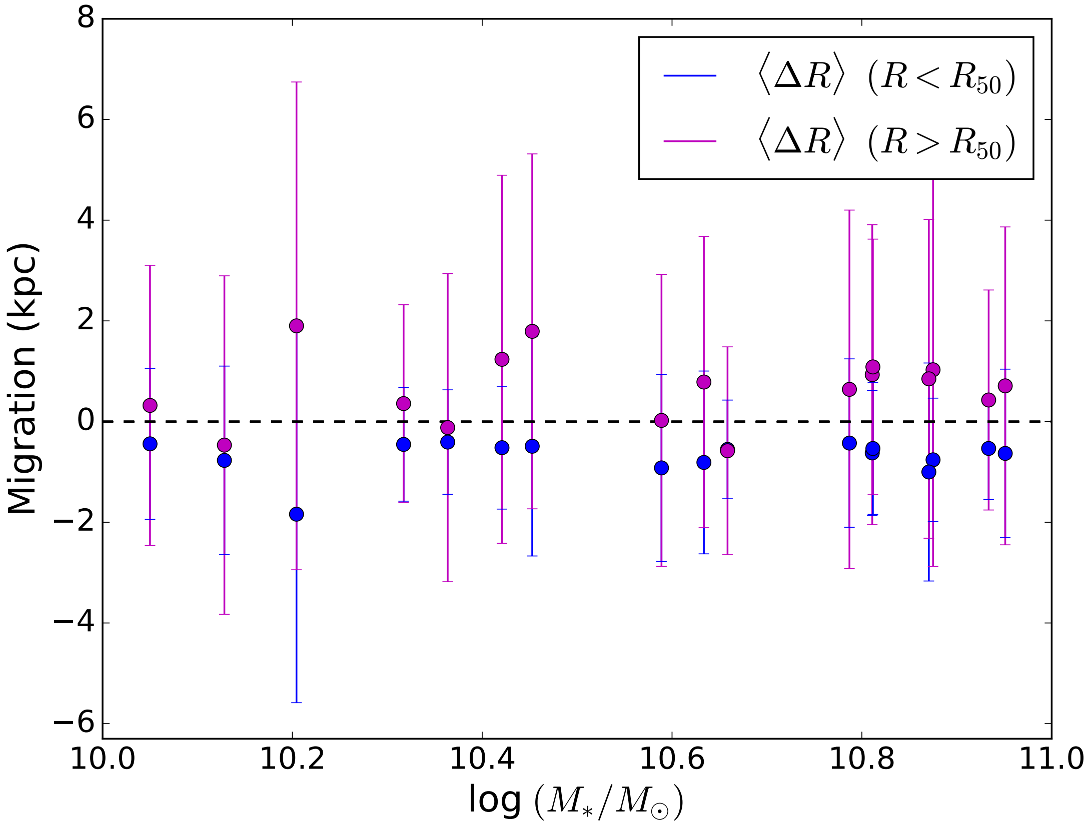

Figure 3.4: As Fig. 3.3, but for the mean migration for the stars within (blue) or outside (magenta) the half mass radius of the galaxy at redshift $z = 0$. The former show on average negative values for most systems, indicating that their birth radius was in an outer region, whereas the latter have the opposite trend.

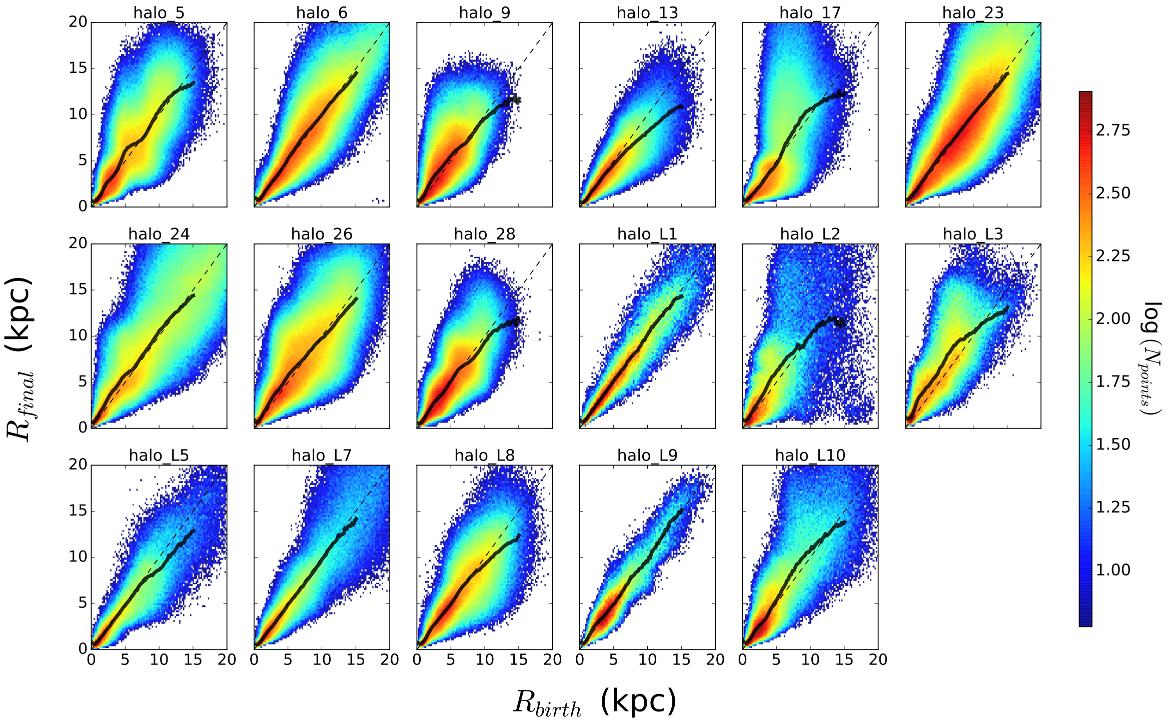

Figure 3.5: Birth radius versus final radius at $z = 0$ for all the stellar particles with circular orbits in the simulated discs. The solid line represent the median R_{final} in bins of R_{birth} and the dashed line is the one-to-one line where $R_{\text{final}} = R_{\text{birth}}$. Most distributions appear symmetric around the one-to-one line but there are also cases like 'halo_17' (5th top row) or 'halo_9' (3rd top row), where there are several stars above the one-to-one line, born between 5-10 kpc but having migrated outwards to 10-15 kpc.

by the median line. However, some systems, such as ‘halo_5’, ‘halo_9’, and ‘halo_17’, show an excess of positive migrators (above the one to one line) for stars that have been born between 5-15 kpc. These can be identified as systems that have a strong bar in their centres which drives more significant migration. The other systems in our sample which exhibit a strong bar at $z = 0$, such as ‘halo_24’ and ‘halo_26’ (see Fig. 3.2), also show evidence of a ‘bump’ in their distribution in Fig. 3.5 out to higher R_{final}.

We can decompose the information in Fig. 3.5 further by looking at the differences between birth and final radii in different radial bins and also for stars of different ages. To do this, we select stars in broad bins of birth radius and measure the distributions of their redshift zero radii. In addition, within each radial bin we split the stars based on their age at $z = 0$, so that we can examine the strength of the migration for different stellar ages. We can compare our resulting distributions with the predictions from the study by Frankel et al. (2018), which models stellar migration around the solar radius as a diffusion process following a Gaussian function depending on one ‘migration strength’ free parameter and the time τ after the birth of a star with a dependence that varies with the square root of τ.

In Fig. 3.6, we show an application of this method for four distinct radial bins in one of our systems, ‘halo_6’, which is a typical Milky-Way-like disc with a quiet merger history and no strong bar in the centre. The resulting distributions are fairly symmetric and we find that their peaks can be fit reasonably well with a Gaussian function. However, the wings of the distributions, particularly in the inner part of the galaxy, are not fully described by a simple Gaussian distribution. Older stars appear to have diffused more from their birth radius, resulting in broader distributions, and additionally they show a larger shift away from the centre of their initial radial bin. In this particular case the shifts are inwards, as seen mainly in the two rightmost panels, but this is not the case for all systems and depends on the selection of the radial bin. Qualitatively this figure agrees with the similar Fig. 1 from Johnson et al. (2021) both in terms of the widening of the histograms with age and the largest shift of the peak occurring for older populations.

In addition, this representative example agrees quite well with the Frankel et al. (2018, 2020) model at radii around the middle of the stellar disc (i.e. $\sim 5.4 - 13.8$ kpc), in terms of the predicted spread of the histograms.This is encouraging because the Frankel models were fit to APOGEE DR12 data of Milky Way stars between galactocentric radii of 5 and 14 kpc. Although, we note that the small median shift we find in Auriga is not included in their functional form of migration. In order to present an average picture of what we observe in our whole sample, we measure the widths of these histograms in all cases for four stellar ages and four radial bins. We have checked that measuring either the 16-84 percentile or getting the variance of a Gaussian fit gives consistent results and we select the former to quantify the width of the histograms. We define this quantity, σ_{migr}, to be a measure of the migration strength.

In Fig. 3.7, we show the average values for σ_{migr} as a function of the stellar age, for each of the radial bins. We show the exact datapoints that were used to construct these curves in the Appendix B Fig. B.1. For this figure, we have selected the radial bins to be normalised by the half-mass radius of each disc, thus accounting for the variation in disc size across the sample. We consider the centres of the four bins as the radii at 0.5, 1 , 1.5 and 2 times R_{50} and select all the stars which have been born within 1 kpc of these radii. We obtain the mean age dependence

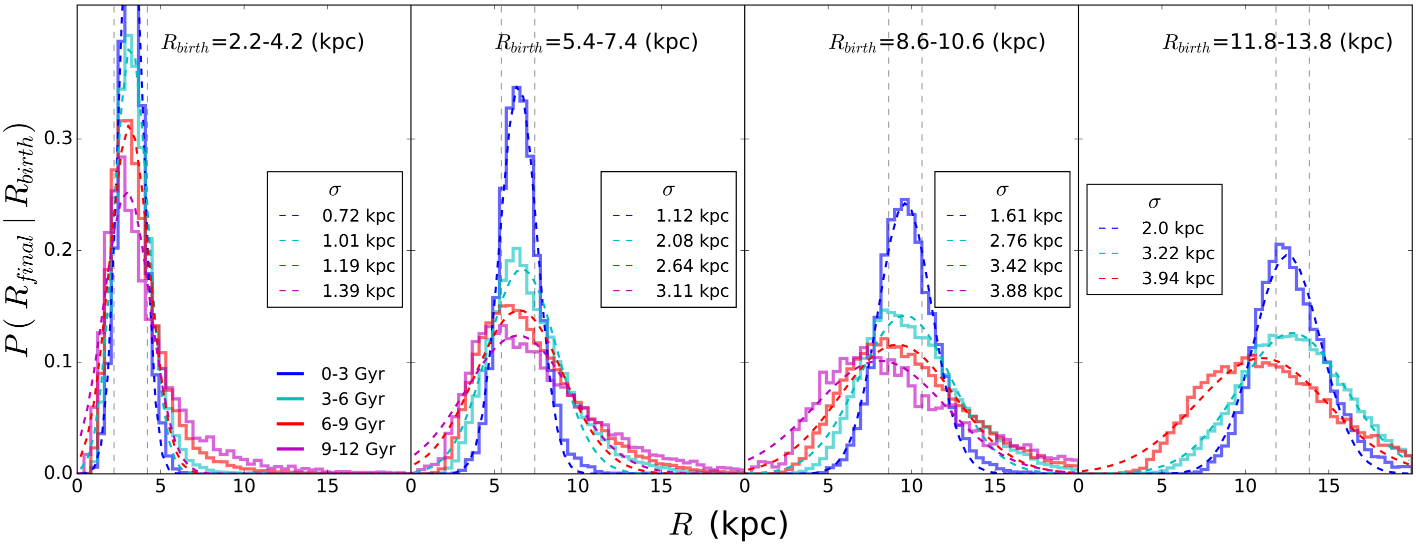

Figure 3.6: Probability distributions of final galactocentric radii for given birth radii bins, split by stellar age at $z = 0$ for 'halo_6'. We overplot with the dashed lines the Gaussian fit to each histogram and in the legends we quote the 16-84 percentile of the histograms. We observe that the distributions become more extended with increasing stellar age as well as for stars that have been born in larger radii. The distributions are fairly symmetric and the peak is shifted from the centre of the selection region especially for the older populations. We stress that these Gaussian fits are meant to guide the eye, and are not used to quantify migration, which is instead measured by the 16-84 percentile range.

for these four radial bins, and compare these to the radially-independent models by Frankel et al. (2018, 2020) which we overplot. The median age dependence appears shallower in Auriga (for each of the radial bins) than in the Frankel models. However, the range of σ_{migr} values found for our radial bins with $R \gtrsim 1\ R_{50}$ is roughly consistent with the model of Frankel et al. (2020), which is tuned to Milky Way stars at similar radii. The slope predicted by the Frankel et al. models is noticeably steeper than our curves at the three outer radial rings. In particular a power law fit to the σ_{migr}-age curves gives us values of 0.4 (cyan), 0.28 (green), 0.25 (yellow), compared to the square root age dependence of 0.5 employed in the models. The median values that we find for $\sigma_{\rm migr}$ are in the range of 1-4 kpc depending on the radial bin and the age of the stars, which connects well to the values of $\langle \Delta R \rangle$ from Fig. 3.3 for the whole population of stars. This is also broadly consistent with the values reported by Verma et al. (2021) derived from the stellar metallicity dispersion of forward-modelled mock data for cross-matched *Gaia*, APOGEE, and *Kepler* observations.

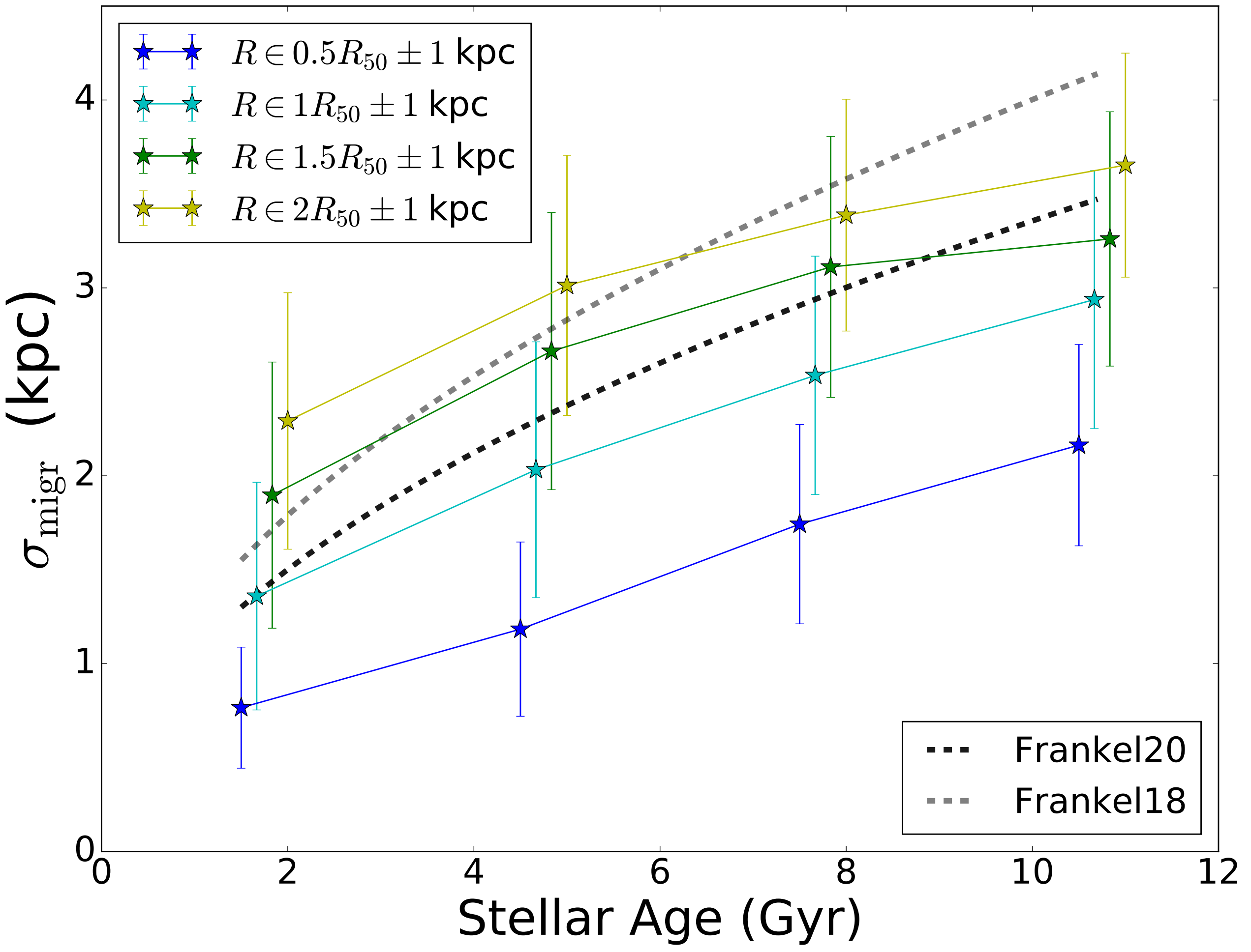

Figure 3.7: Median values for the spread in stars from their initial positions (i.e. migration strength) measured as the 16-84 percentile of the histograms in Fig. 3.6, as a function of their age at $z = 0$. The solid curves show the median from all the halos in four radial bins of width 2 kpc centered on multiples of the stellar half mass radius, R_{50}. The dashed grey and black curves show two radially-independent models by Frankel et al. (2018, 2020), for comparison.

3.3.2 Effect of migration on radial profiles of age and metallicity

As a further step, we would like to investigate the effect of stellar migration on the metallicity and age profiles in Auriga. To do this, we plot the mean age and metallicity radial profiles for the stars in each of our simulated galaxies at $z = 0$ in Figs. 3.8 and 3.9 (solid lines). We use the $z = 0$ galactocentric radii of the stars, normalised to R_{90}, which gives us the true profile observed in the simulation. The profiles are computing by averaging over the metallicities and ages of all stellar particles at a given bin of R_{90}. Additionally, we calculate the same profiles but assuming the birth radius of each star as its final radius, in other words simulating a scenario without any stellar migration (dashed lines in Fig. 3.8, 3.9). We then compare in each case the solid and dashed curves to evaluate the effect of stellar migration.

In the case of the mean age profiles (Fig. 3.8), we find differing results, depending on the halo, when comparing profiles with or without migration. In a number of halos, such as 'halo_9', 'halo_23' or 'halo_L3', migration of stars leads to the flattening of the profiles at outer radii, meaning that older stars have migrated outwards, increasing the mean age in those regions by $z = 0$. On the other hand, there are cases such as 'halo_L7' or 'halo_13' where there is minimal difference between the two profiles, hinting towards very little stellar migration in these systems. There is no evident change in the overall scatter around the median. We already find an inherent scatter in the ages within each radial bin, suggesting that stars have formed at varying times at all radii, and migration does very little in further amplifying this spread.

In the case of the mean metallicity profiles (Fig. 3.9), we choose to plot the solar-normalised iron abundance (in Auriga solar iron abundance is taken from Asplund et al. (2009)), [Fe/H], which is a common indicator of a stellar population's metallicity. We calculate the total radial [Fe/H] profile for (a) all stars, and (b) stars that belong to different age bins. These are shown in Fig. 3.9. Strikingly, we observe that the effect of migration appears not to be evident at all in the total profile, and barely noticeable for the younger stars in all the cases. However, for the older stars, in most cases, there is a flattening of the metallicity profile, due to more chemically enriched stars migrating to larger radii over cosmic time. This suggests that the lack of evolution in overall metallicity profiles is due to the outer disc being dominated by younger stars, which have not migrated as strongly as older populations.

To make a quantitative statement of this flattening, we fit both the true and the 'birth-radii' profiles, excluding their core (i.e. only for $R/R_{90} > 0.2$), with a linear fit that gives a slope α. We then measure the change in α between the true profile and the one without stellar migration, $\Delta\alpha = \alpha_{z=0} - \alpha_{\mathrm{birth}}$. Fig. 3.10 shows the change in this outer slope for each different profile, plotted against the maximum A2 coefficient for the given disc (left panel) and its stellar mass (right panel). We examine the strength of the correlation between the change in the slope and these two quantities by calculating the Pearson correlation coefficient for each of the age sub-samples. A correlation is present with respect to both the stellar mass and the A2 coefficient despite the two quantities not being strongly correlated with each other.

The normalization of the best fit lines changes with the stellar age in the fashion we expect, with older stars showing higher $\Delta\alpha$ values. This reflects the clear flattening over time of metallicity profiles for older stellar populations. Nonetheless, there is also a shallower trend of increasing flattening with increasing bar strength and/or stellar mass for younger stellar populations. Indeed,

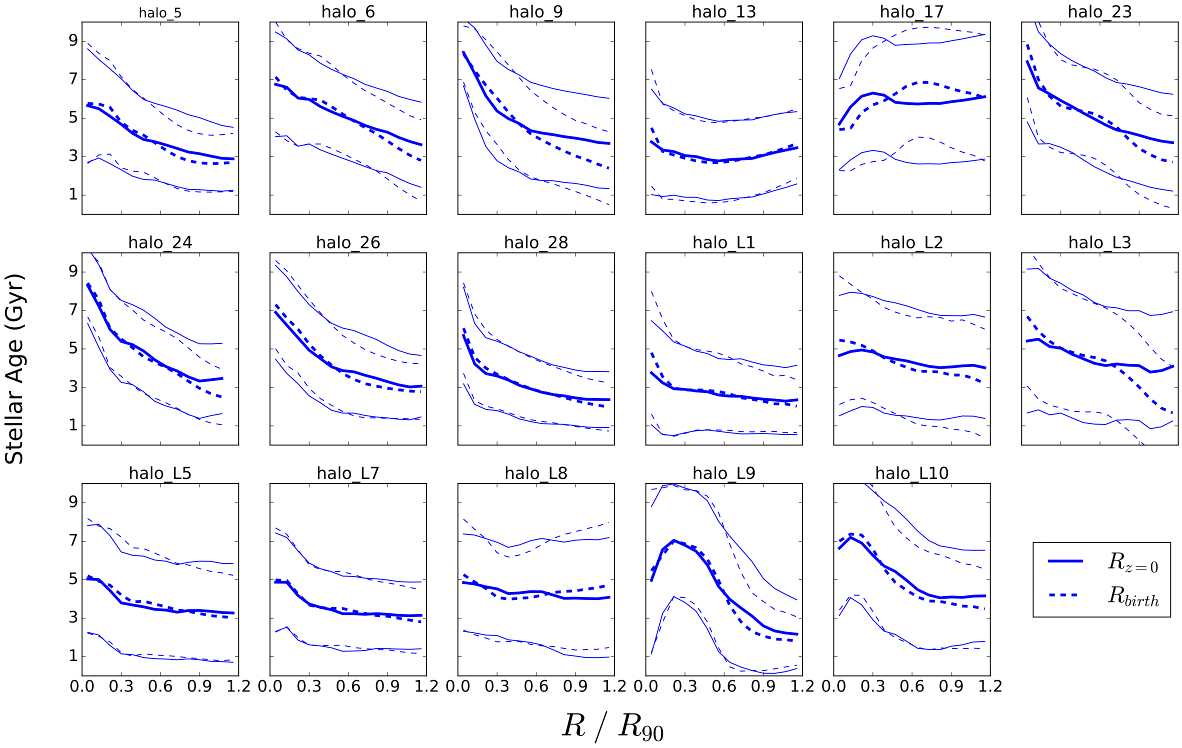

Figure 3.8: Mean stellar age profiles for the 17 halos in the simulation suite. The solid bold lines represent the true $z = 0$ profiles whereas the dashed lines are the profiles that would have been obtained if the stars were located at their birth radii instead. With the thinner lines we show the variance of stellar ages around the mean.

the correlation appears stronger for the younger stars despite the small values of $\Delta\alpha$. But in all cases, the two-tailed p-values are sufficiently small to guarantee that the measured Pearson coefficients could not be drawn by a random uncorrelated sample. This demonstrates that migration is a more significant effect in (a) barred and (b) more massive Milky-Way-like galaxies in Auriga.

The results of this section highlight the advantage of studying a number of disc galaxies with different properties since the importance of stellar migration is not uniform for all the systems and diverging conclusions could be drawn if each system was to be studied individually. Furthermore, the decomposition of the metallicity profiles into age bins shows that migration does not leave the same imprint for stars of different age, and computing only the change in the *overall* metallicity profile would hide the fact that stellar migration is occurring.

3.4 Snapshot-to-snapshot migration

The analysis carried-out above gives us a view of the total migration that has happened over the whole lifetime of the disc, but does not necessarily show us how migration evolves on shorter

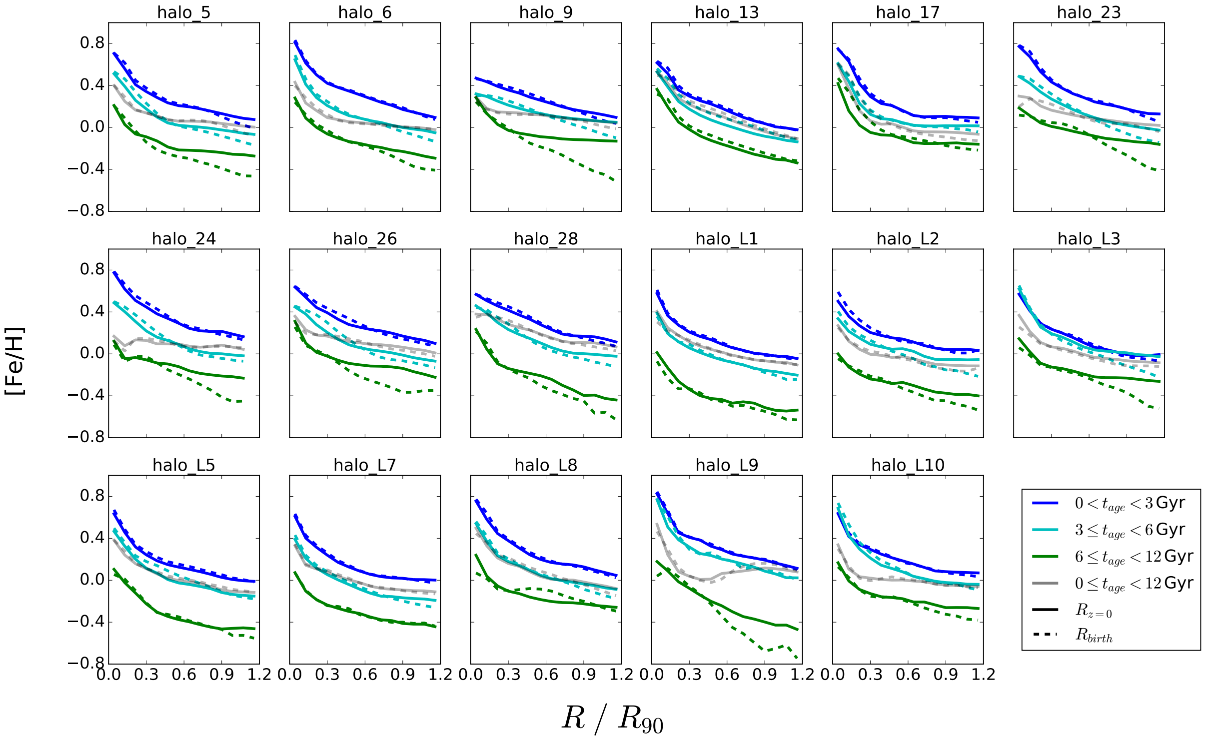

Figure 3.9: Radial metallicity profiles for the 17 halos in the simulation suite in three different stellar age bins. The solid lines represent the true $z = 0$ profiles whereas the dashed lines give the profiles that would have been obtained if the stars were located at their birth radii instead. In many cases, for the older populations, there is considerable flattening of the true metallicity profile compared to what would be produced if there was no migration. This is similar to what is presented in Minchev et al. (2013).

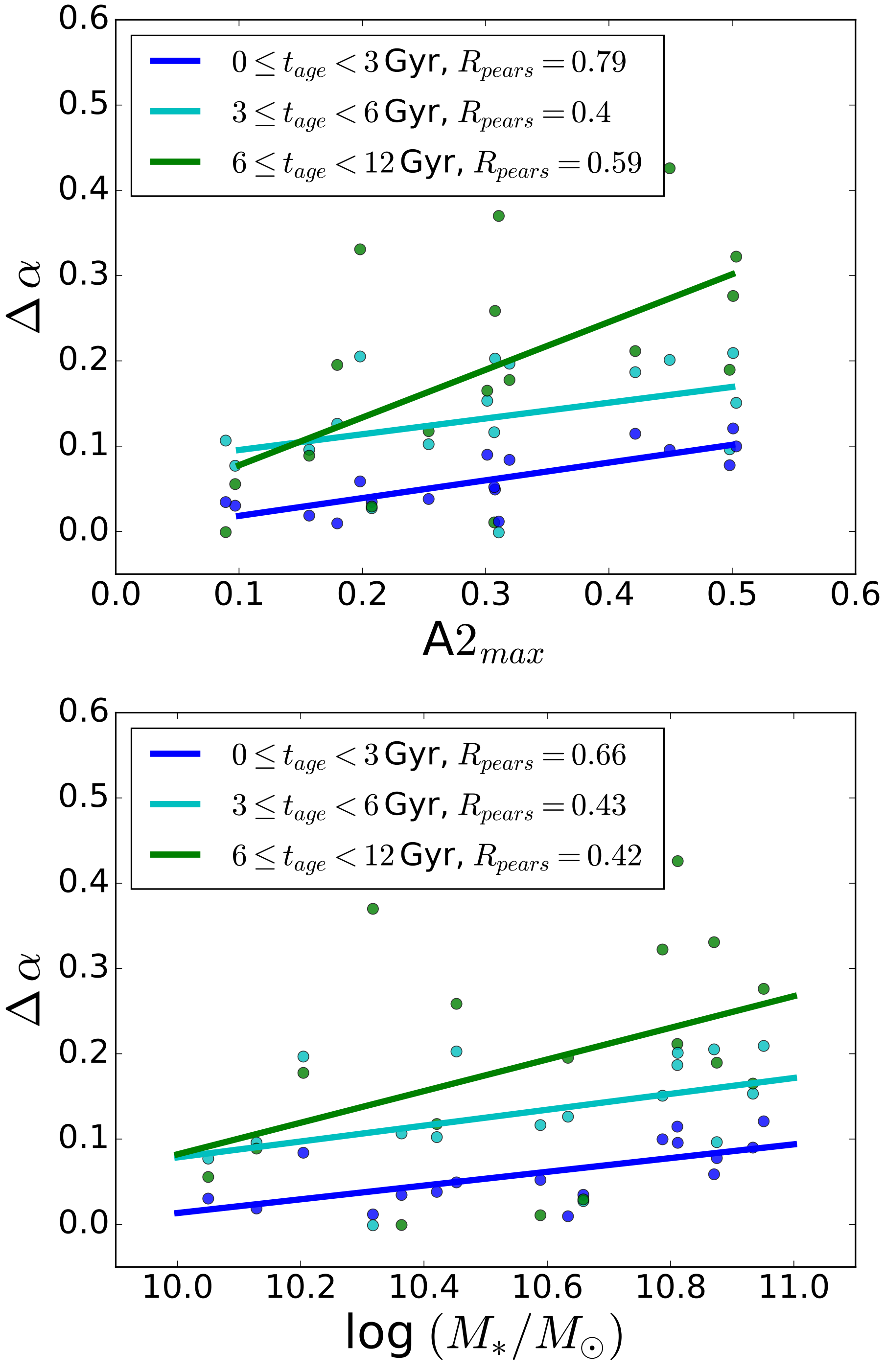

Figure 3.10: Change in the slope of the metallicity profiles ($\Delta\alpha$) presented in Fig. 3.9 measured for radii $R/R_{90} > 0.2$. We show the same three stellar age bins and we plot the $\Delta\alpha$ against the maximum A2 coefficient (top) and stellar mass in the disc (bottom) at $z = 0$. The lines are the linear fits to each data set, and we quote in the legend the Pearson correlation coefficient. There is a clear evolution with stellar age in the values of $\Delta\alpha$, and loose correlations of $\Delta\alpha$ with both A2 and the stellar mass are present.

timescales. We are interested in this information as we are looking for an implementation of stellar migration for semi-analytic models of galaxy evolution where the model is updated on timesteps with a typical length of order 10 Myr. Therefore, in this section we analyze the changes in the position of stars that happen between two consecutive simulation snapshots.

For each stellar particle we compute both the galactocentric radius and the guiding centre so that we can analyse the effect of each on the 'churning' and 'blurring' processes. A change in the galactocentric radius can result from both mechanisms but the changes in the guiding centres are solely due to torques exerted on the stars and directly relate to the 'churning' process. The galactocentric radii are inferred directly from the simulation output as the distance between the position of a star and the centre of the disc. The guiding centres are computed using the information of the orbital angular momentum of a star, $l_{z,c} = RV_c$, and interpolating this value to the rotation curve of the galaxy. From now on we refer to any quantity associated with guiding centres with a subscript 'g'. Similar to the $R_{z=0} - R_{birth}$ calculations, we can look at initial, R_i (or $R_{g,i}$), and final R_f (or $R_{g,f}$), radii for the stellar particles, but in the subsequent analysis they are referring to any two snapshots in the simulation.

Firstly, we directly estimate the difference between the initial and final radii (guiding or galactocentric) for our different halos and at a pair of snapshots. In Fig. 3.11 we plot this difference in galactocentric radii $\Delta R = R_f - R_i$ against the initial galactocentric radius R_i, and similarly in Fig. 3.12 the difference in guiding centres $\Delta R = R_{g,f} - R_{g,i}$ against the initial guiding centre $R_{g,i}$. These figures are analogous to similar plots shown in previous studies such as (Minchev et al., 2012a; Minchev & Famaey, 2010) (showing change in angular momentum ΔL in the y-axis) or Halle et al. (2018) (showing both ΔR and ΔR_g). We present examples of two characteristic halos from our sample; one develops a strong bar during its lifetime ('halo_5') and the other does not at any point in time ('halo_6'). We show in both of these figures three different time intervals between the two snapshots, where the initial snapshot is always the same, at lookback time of 1 Gyr, and the final differs by the given Δt, in this case with values of 200 Myr, 800 Myr and 1.4 Gyr.

In the case of the galactocentric radii (Fig. 3.11), the resulting patterns may not be identical between the two halos but they show similarities in the overall spread of amplitudes in the y-axis as well as little evolution with increasing Δt. The particular halo that we choose, 'halo_6', has a well-developed spiral arm pattern, which manifests in the $\Delta R - R_i$ plot as a series of diagonal regions of stronger migration around the location of the over-densities. It is interesting to observe that this effect becomes less pronounced if we look at snapshots that are separated by a longer timestep as it is most likely smoothed out by the longer time averaging and the transient nature of spiral arms (Sellwood & Binney, 2002; Grand et al., 2012b,a; Baba et al., 2013).

Regarding the guiding centres (Fig. 3.12), there is a clear distinction between the two galaxies. In the case of the barred galaxy ('halo_5'), there is an extended ridge of more strongly migrated (inwards and outwards) stars, the location of which matches with the co-rotation radius of the bar. Stars in this region have migrated up to 5 kpc outwards or inwards whereas in the other radii they are constrained within 2 kpc. The same pattern for a system without a bar ('halo_6') has no distinct features, and we can only observe that the values for the migration are slightly larger in outer radii compared to the inner ones, although overall most stars appear to migrate less than 1 kpc. What is common in both halos is the widening of the patterns in the y-axis as we allow

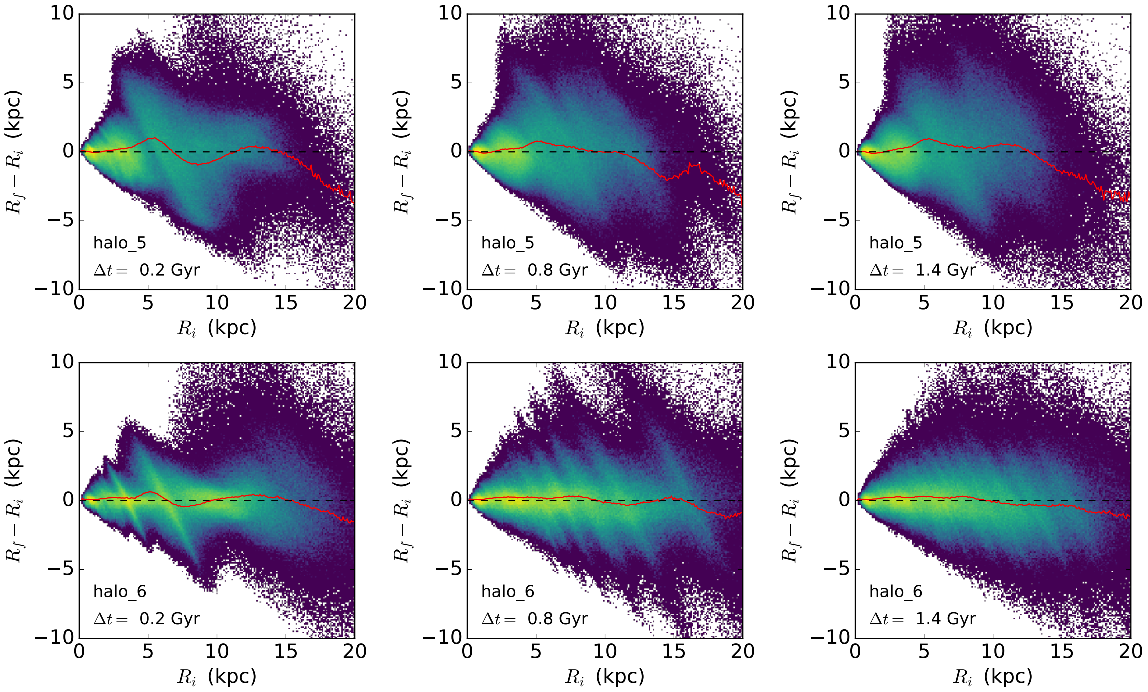

Figure 3.11: Change in galactocentric radius of the stars indentified in two snapshots plotted against their initial radius. The top row is an example of a galaxy in our suite which has a strong bar (‘halo_5’) for most of its lifetime, whereas in the bottom row the galaxy has developed no bar (‘halo_6’). From left to right, we show three cases where the initial snapshot is the same but a different final snapshot separated by Δt is chosen each time. Despite the galaxy specific differences in both discs we find that most stars have changes in their galactocentric radii between -5 to 5 kpc no matter how how large Δt is.

more time between the snapshots, indicating a process that is time (or timestep) dependent.

These examples are representative of the behaviour that systems with or without a bar develop. Each halo in our sample could be studied on its own to get a much deeper understanding of each individual object, but we are more interested in this work in an average description of what we observe in our 17 systems. Thus, we would like to arrive at a formulation that describes, as generally as possible, the variations that we see in the y-axis of these plots for the galactocentric radii and the guiding centres.

3.4.1 Stellar migration at different radii

Our aim is to describe the effect of stellar migration at different radii and for this reason we perform a radial ring analysis. We split each galactic disc into a series of concentric annuli (rings) in the x-y spatial plane extending out to 15 kpc in radius and 2 kpc above and below the disc plane in the z-direction. For the vast majority of snapshots, this radial extent is sufficient

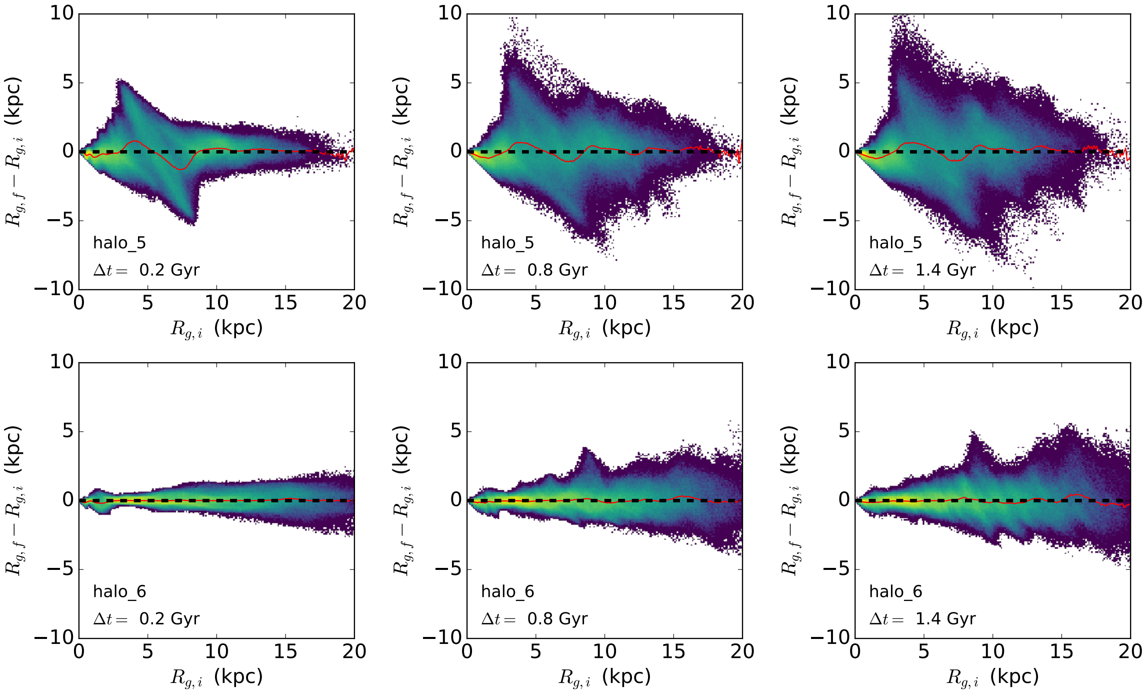

Figure 3.12: Similar as in Fig. 3.11 but for the guiding centres of the stars. The same two galaxies are shown for the same snapshots. Here the difference between the barred and unbarred system is evident with the former having more extreme stellar migration, especially for stars located between 5-10 kpc. We also observe a widening of the migration pattern with time (from left to right).

to enclose the entire stellar content of the disc. We choose a number of 20 rings, based on the radius R, that are of equal width and are linearly spaced in order to have a statistically reasonable number of stellar particles for each ring. We have tested for different height cuts and find that as long as we use a cut more than 1 kpc we obtain convergent and robust results.

Each stellar particle falls in a given ring based on its galactocentric radius. At the initial snapshot, n, we record both its radius and compute its guiding centre. We then look for the same quantities at a subsequent snapshot, $n + m$. The selected stars have associated individual IDs which can be used to identify them at a later snapshot times in Auriga. Similarly to the analysis of birth-final radii above, we also impose a cut of $\epsilon > 0.7$ in the circularity parameter.

For each star, we compute the change in galactocentric radius as $\Delta R = R_{n+m} - R_n$, and the change in the guiding centre as $\Delta R_g = R_{\mathrm{g},n+m} - R_{\mathrm{g},n}$. We then create distributions of ΔR or ΔR_g, associated with each ring, for a given halo and at a given initial snapshot n. We show in Fig. B.2 examples of these histograms at two different radii for a particular halo. For a number of cases, the histograms can be approximately fit with a Gaussian function with the peak shifted from zero either to the negative (median inwards migration) or to the positive (median outwards migration), and are mostly symmetric around the median. However, since there are instances of heavily skewed distributions or distributions with broadened wings (as seen, for example, for 'halo_6' in Fig. B.2), we refrain from universally fitting a Gaussian to extract the properties of each histogram. Instead, similar to the analysis of radial gas flows in Auriga presented in Okalidis et al. (2021), we quantify the resulting distribution by (a) its median, $\overline{\Delta r}$ and $\overline{\Delta r_g}$, and (b) its width (i.e radial spread), w and w_g. We choose to measure the width as the value of the 16-84th percentile of the distribution divided by 2 that corresponds to 1σ of a normal distribution. We carry out this process for different values of the initial snapshot n, starting from $n = 150$, which corresponds to a lookback time of $t_{look} \sim 6$ Gyr in our simulations, up to the last available snapshot based on the value of m. We do not look further back in time because we are interested in the regimes when our halos have formed a well-developed rotationally supported stellar disc, which may not be the case in some of our systems at earlier redshifts.

We repeat this analysis varying the value of m, namely we use $m = 1, 3, 5, 7, 10$, and 15, to constrain the evolution of w, w_g and $\overline{\Delta r}$, $\overline{\Delta r_g}$ with increasing snapshot spacing. The option of $m = 1$ equates to about 60 Myr in our simulations and $m = 15$ to a timespan of 1 Gyr. For the presentation of some results in the next sections we choose as a default the value of $m = 10$, which corresponds to $\Delta t = 600 - 700$ Myr between two snapshots which is approximately 3 dynamical times at the Solar radius. We believe this is a sufficient period of time to approximate migration as a diffusive process. To summarize, we obtain data points for the four w, w_g, $\overline{\Delta r}$, and $\overline{\Delta r_g}$ quantities which are associated with a set of variables, the centre of the ring, the initial and final snapshot times and their difference and the specific halo that the ring belongs to ($R_{ring,j}$, t_n ; $\Delta t = t_m - t_n$, halo$_k$).

Furthermore, for a given choice of m, we analyse how migration depends on stellar age by binning stars into groups of 0-1 Gyr, 1-3 Gyr, 3-5 Gyr, and 5-8 Gyr based on their ages at the initial snapshot of selection, and applying the same analysis as above.

3.4.2 Radial Profiles

In this section we analyze how w, w_g, $\overline{\Delta r}$, and $\overline{\Delta r_g}$ vary according to radius. For each ring, we get a normalised value for the ring's mid-radius, $R_{sc} = R_{mid}/R_{90}$, where R_{90} refers to the 90% mass radius at the initial snapshot n. In Fig. 3.13 we show the normalised radial profiles for our four quantities that result from averaging the data from all our systems. In each panel the curves represent a different value of Δt between the initial and final snapshot.

The first important result to take away from Fig. 3.13 is that there are qualitative and quantitative differences in the radial profiles when using the galactocentric radii or the guiding centres as indicators of migration. In general, the values for w and $\overline{\Delta r}$ are larger than the corresponding values for w_g and $\overline{\Delta r_g}$ for the same time difference. In both cases, the width of the distributions increase as we move towards the outer rings, but in the case of the median shifts we find higher negative values (inflow) for $\overline{\Delta r}$ as we move outwards in the disc than we do for $\overline{\Delta r_g}$. It is worth noticing that $\overline{\Delta r_g}$ and $\overline{\Delta r}$ have almost exclusively negative values at all radii which corresponds to stars moving inwards on average in the given ring. That is simply the median of the histograms that comes out negative in most cases, but there is always a significant number of stars that have migrated outwards. This information is better captured in the values of w and w_g.

3.4.3 Time interval dependence

Concerning the dependence of the median shift and the spread on the snapshot spacing, we see a clear evolution in the radial profiles over all radii for w_g and $\overline{\Delta r_g}$. As expected, if we allow more time between the two selected snapshots the width of the histograms is larger, that is to say stars appear to have diffused more strongly out from their initial positions. The respective evolution for w is much more obscure and in particular the curve for the case where we allow our minimum timestep $(n + 1)$ does not follow the same trend as the other choices of Δt. Moreover, in the case of $\overline{\Delta r}$ it can be argued that there is no clear timestep dependence at all as the several mean curves for the different timesteps overlap significantly.

If we assume that migration, as the change of the guiding centres, was a pure diffusion process, we would expect to recover a $w_g \sim \Delta t^{0.5}$ dependence. Therefore, following the approach used by Okalidis et al. (2021), we assume that there is a more general time dependence of the form $w \sim \Delta t^{a}$ and construct logarithmic plots of w and w_g, with the aim to extract the slope, thus giving us a measurement of the actually realized exponent a. From Fig. 3.13, it is already evident that this time dependence is not the same in different radial scales. Thus, we split the data into three broad bins of normalised radius to determine if there is also a radial dependence of a.

This is shown in Fig. 3.14 for the $w_g - \Delta t$ relation for the combined data for all the halos. In this case, we do not recover the $a = 0.5$ exponent expected for pure diffusion in any radial bin, but there is a radius evolution that approaches this theoretical value at larger radii. We should not necessarily expect to get the theoretical slope for the average of all the halos, which may have significantly different evolutionary history and structural properties. So, we further calculate the exponents in each individual system. This is shown in the Appendix B Fig. B.3, from which it immediately becomes evident that there is a range of values for a obtained for the different halos. Overall, in the innermost radial bin, the slope is significantly flatter in all cases.

This appears reasonable because these central regions are often dominated by a bulge or a bar rather than featuring a very flat rotation dominated stellar disc and indeed there is a correlation in that strongly barred systems have a lower exponent for the inner ring. In contrast, at large radii, there are cases where the values of a are reasonably close to the diffusion case (for example, in 'halo_6') and we do not see a strong correlation between the bar strength and the slope.

The same figure, Fig. 3.15, for the $w - \Delta t$ confirms what was found before, that the shortest timestep does not follow the same linear trend in the log-log plot resulting in a bad fit which yields a very low value for the exponent a. On top of that, a varies significantly if we calculate it individually for each halo and is in most cases much flatter than the diffusion value of 0.5. It must also be noted that although it looks like in the combined dataset that the rest of the points follow a linear trend, this does not appear in many of the individual systems. Therefore, from our data, we cannot conclude the presence of a robust time dependence such as we found in the case of guiding centre quantities.

There is also a clear timestep dependence in the median shift in guiding centre radius, $\overline{\Delta r_g}$. Although it can also be quantified at the different radial bins, we find that it varies much more significantly from halo to halo, and in many individual cases there is no discernible time interval dependence at all.

All in all we cannot safely suggest that the migration process is purely diffusive in the average of our sampled discs, however it can be described as such in certain individual systems. Moreover, it is only when we compute the changes in the guiding centres that we can retrieve a timestep dependence that is similar to a diffusive process, since the changes in galactocentric radii seem to be following a much flatter time evolution both in the average and the individual systems.

3.4.4 Bar and age dependence

In Fig. 3.16, we plot the radial profiles for one fixed value of Δt ($n + 10$), in order to study the effect of the presence of a bar in the disc, as well as any differences between stars of different ages. We split our sample in two sub-samples of strongly-barred and weakly-barred systems, based on the maximum A2 value at redshift zero, with each sub-sample then having 10 and 7 galaxies, respectively, if we take 0.3 as the separating value.

We find that, in the case of the galactocentric-radii-based quantities $\overline{\Delta r}$ and w, on average, the radial profiles are consistent with each other between the strongly-barred and weakly-barred galaxies, suggesting that the information conveyed by these two quantities cannot be directly associated with the presence or absence of a bar. This is reasonable as (1) Δr is largely influenced by the exact position the star particle is captured at the particular snapshot time during its orbit, and (2) there are additional factors that can alter the galactocentric radius of a stellar particle.

There is a greater distinction in the radial profiles for guiding-centre-based quantities. The barred galaxies have on average higher values of w_g at all radii, with the difference being maximised at the central part of the disc around the co-rotation radius of the bar. This is more evident if we study the radial profiles for individual galaxies. It is not very pronounced when averaging all the barred systems because of the different strengths and radii of the bars so that we can have a partial cancelling of the bar effect by averaging a region which is dominated by the bar co-rotation in one halo and a region that is further in or out of the co-rotation radius in

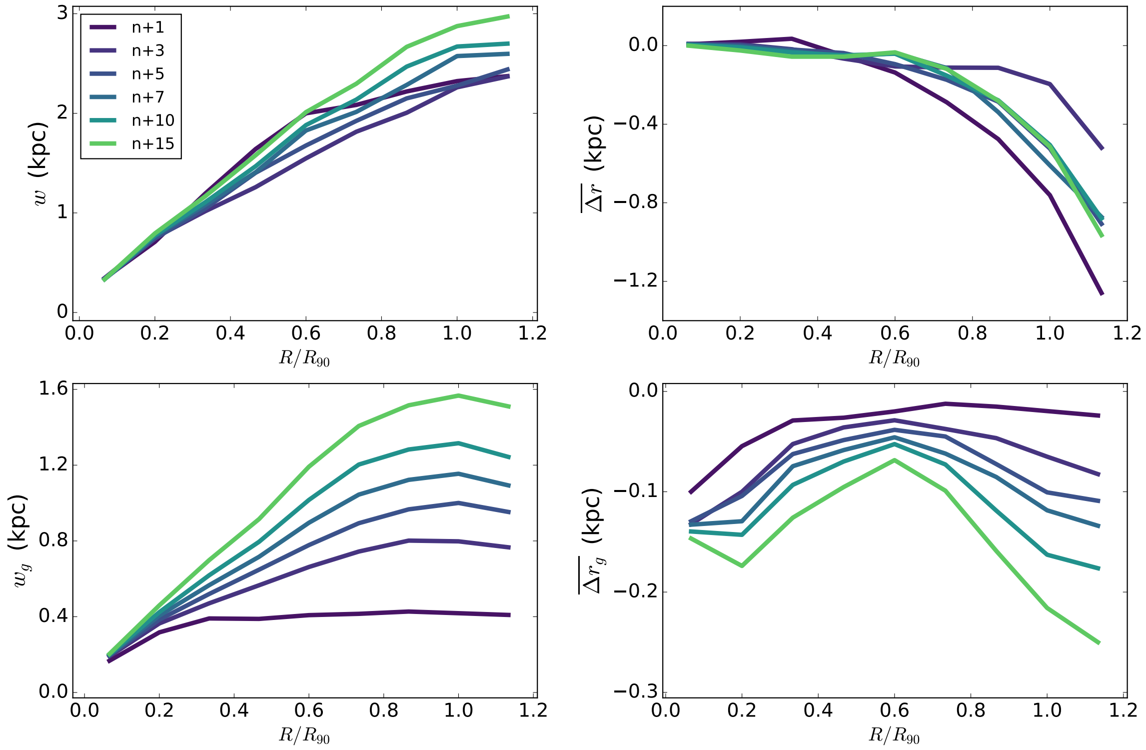

Figure 3.13: Mean radial profiles of the quantities that describe the distributions of Δr and Δr_g plotted in terms of the normalised ring radii. In the left panels we plot the spread of the histograms and in the right the median. The top panels are for galactocentric radii and the bottom ones for the guiding centres. Here we plot these profiles for different selections of snapshot spacings between the initial and final positions to show the evolution with Δt. The latter appears to be more pronounced and more clearly defined when changes in guiding centres are considered.

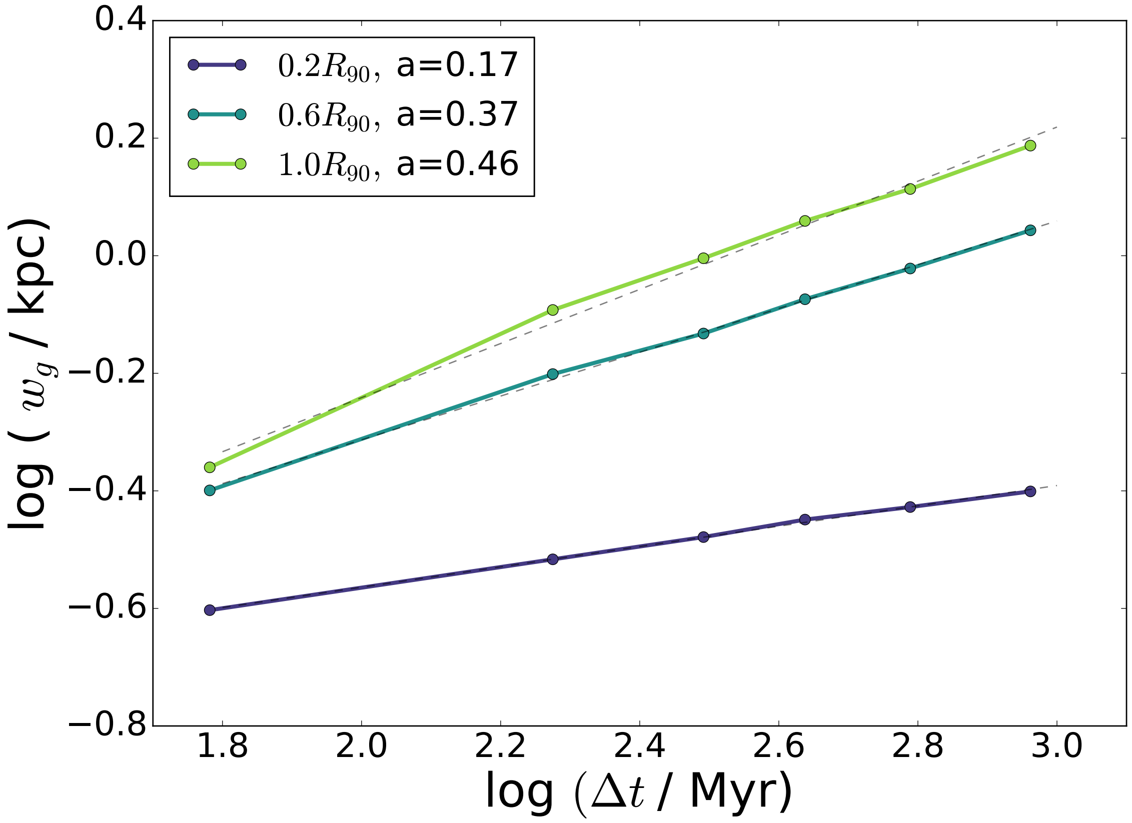

Figure 3.14: Logarithmic plot of the spread w_g against the time interval Δt based on the average of the combined data for all the halos. We show the trend in three different radial bins and observe a variation of the time interval dependence with radius, with a stronger effect being found in the outer radii.

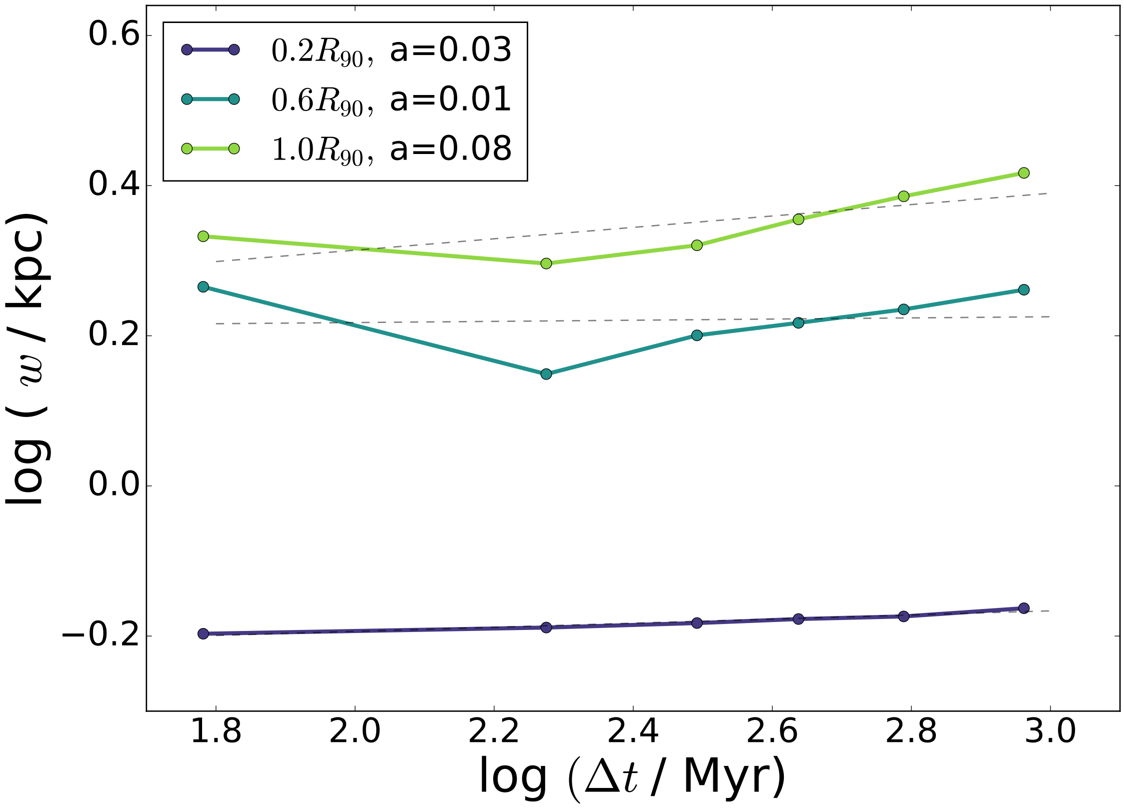

Figure 3.15: Logarithmic plot of the spread w against the time interval Δt based on the average of the combined data for all the halos. We show the trend in three different radial bins.

another. These profiles reflect what we observe, plotted in a different manner, in the $\Delta R_g - R_{g,i}$ (Fig. 3.12) and $\Delta R - R_i$ (Fig. 3.11) plots.

Concerning $\overline{\Delta r_g}$, there is significantly increased inward migration in the innermost regions of strongly-barred systems compared to weakly-barred systems, as shown in Fig. 3.16. This feature appears in both the average profiles and each individual barred halo. The weakly-barred systems have very flat profiles for radii $\sim 0.6\,R_{90}$ with less inward migration.

In Fig. 3.16, we also explore the stellar age dependence of each of the quantities w, w_g, Δr, and Δr_g by showing four different age bins. When measuring the total migration in the previous sections, there is a hint of an age dependence, with older stars experiencing larger migration (Fig. 3.6, 3.7). This is not immediately reflected in the values of our measured quantities in the different age bins. The spread w shows no evidence of a consistent age dependence with the different curves overlapping with each other. The corresponding spread w_g has a clear age dependence with up to a 30 per cent difference between the youngest and oldest bin. This dependence is the opposite to what was found before for the total migration – stars in the earlier stages of their lives appear to be more diffusive in terms of the changes in their guiding centres. We must stress though, that the age definitions in this and the previous sections are not identical since in section 3.3 we refer to the age of the star at $z = 0$ whereas in this section it is the age of the star at a given snapshot. The effect itself can be explained on the basis that younger stars, having lower velocity dispersion, are more prone to be impacted by angular momentum exchanges that can happen in the disc (e.g. Vera-Ciro et al., 2014). The overall larger effect for the older stars when looking only at the difference between $z = 0$ and the star's birth radius is merely due to the fact that the small instantaneous changes are adding up for a longer time. The median shifts, $\overline{\Delta r_g}$ and $\overline{\Delta r}$, show a similar age dependence, with older stars having more negative values, meaning that they are on average shifted more strongly inwards although the trend reverses in the outer rings for $\overline{\Delta r_g}$.

3.4.5 Parametrization of stellar migration in Auriga

Our goal in this section is to present a simple parametrization of the strength of radial migration in Auriga, which we have so far described either by w and $\overline{\Delta r}$ (for changes in galactocentric radii) or w_g and $\overline{\Delta r_g}$ (for changes in guiding centre radius). In the case of the galactocentric radii, as we saw in the previous sections, there are weak but quantifiable trends with the size of the timestep interval between the analyzed snapshots. However, there are no trends with respect to the presence or absence of a bar, and a dependence on the different stellar ages only for the quantity $\overline{\Delta r}$. For the guiding centre radii, the difference in the median shift radial profiles for the barred and unbarred populations, seen in Fig. 3.16, suggests that separate parametrizations for them may be needed. Indeed, we do not recover the exact same timestep dependence for weakly and strongly barred galaxies, but for sake of simplicity in the parametrization and to increase the number statistics we opt to focus on the average of all the 17 halos. The dependence of some of the fit parameters in the presence of a bar is stated later in the text. In the previous section we presented variations of the time dependence that exist at different radii but for the purposes of a global parametrization we want to collectively describe the curves that we extract for the radial

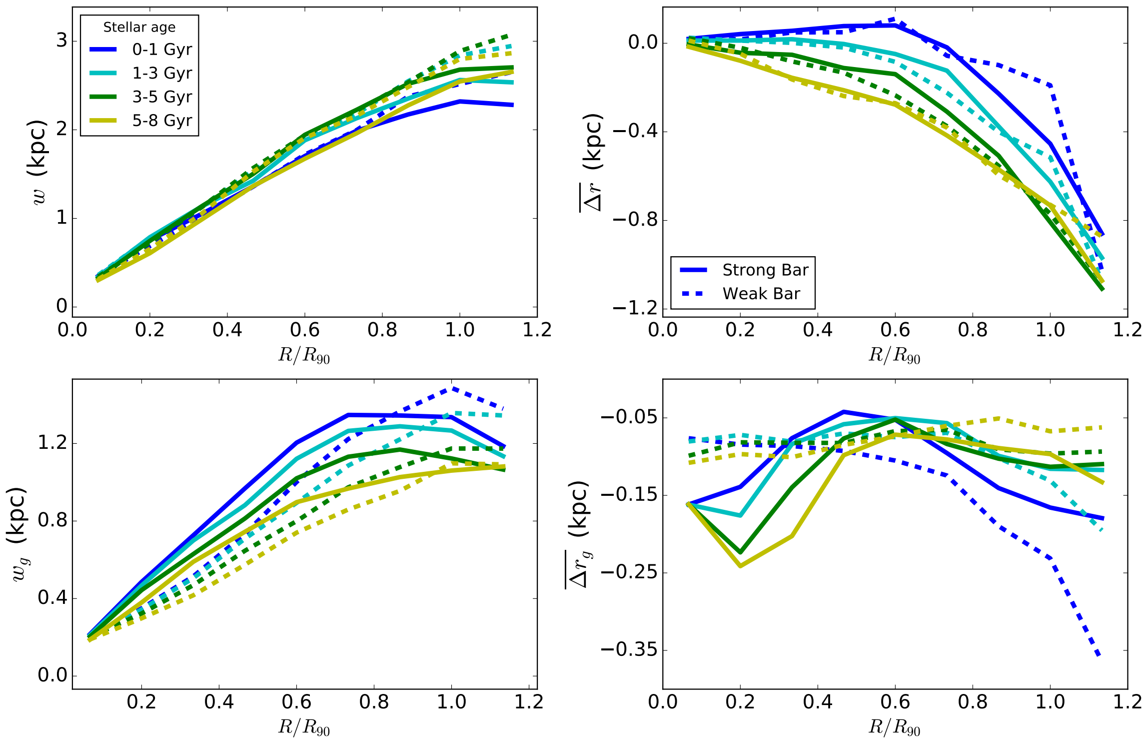

Figure 3.16: Similar profiles as in Fig. 3.13 for a fixed snapshot spacing of $n+10$, corresponding to 600-700 Myr. We split the sample between the halos that develop a strong bar, $A_{2,z=0} > 0.3$, for most of their evolutionary history (solid lines) and those that have a weaker or no bar, $A_{2,z=0} < 0.3$, (dashed). The different colored curves in each panel show the quantities as obtained by using only stars belonging to different age bins (legend in top left panel) selected based on their age at the initial snapshot n.

profiles using a single functional form to capture the average effect.

We fit the radial profiles of w and w_g with power law fits of the form given by Eq. 3.1 below, with the time interval dependence entering both in the exponent and the normalization of the power law.

$$w; w_g = A(\Delta t) R_{sc}^{b(\Delta t)}, \tag{3.1}$$

where $A(\Delta t) = \Delta t^{a}/C_1$ and $b(\Delta t) = \Delta t^{\beta}/C_2$. In Fig. 3.17 we show fits for the 5 selections of time intervals, and how the exponents and normalization constants vary with increasing time interval. We find that both the coefficient A and the exponents of the power laws in radius vary with the selected time interval Δt in a linear fashion when plotted in a logarithmic plot. So each has a power law like dependence on Δt.

We note that we have excluded the $n + 1$ case from these fits because it significantly deviates from the trend that the rest of the cases follow. We argue that this is because the timespan of only ~ 60 Myr is not long enough to robustly measure the diffusion of star particles driven by radial migration, as it is shorter than one rotational period of the stars at most radii. Once we move to time intervals with widths of a few hundred Myr, we find a time evolution that can be expressed accurately with the same power law fit.

The equations that then express w and w_g are:

$$w_g/\mathrm{kpc} = \frac{(\Delta t/\mathrm{Myr})^{0.45}}{12.2} R_{sc}^{((\Delta t/\mathrm{Myr})^{0.27}\,/\,6.9)} \tag{3.2}$$

$$w/\mathrm{kpc} = \frac{(\Delta t/\mathrm{Myr})^{0.18}}{1.2} R_{sc}^{((\Delta t/\mathrm{Myr})^{0.1}\,/\,2.3)} \tag{3.3}$$

where $R_{sc} = R/R_{90}$.

As mentioned before we must caution that the exact coefficients and exponents in these equations strictly describe the average of a diverse set of galactic discs and they would be different if we had only considered a particular type of systems such as those with a strong bar. In particular we find that regarding the quantity w_g the best fit exponent β in the radial term has the same value for both the subsamples of weakly and strongly barred galaxies in our simulations. However, the exponent α that regulates the timestep dependence in the term $w_g \sim \Delta t^{\alpha}$ has a value of 0.38 for the strongly barred subsample and 0.5 for the weakly barred one, these values being on either side of the value of 0.45 for the whole sample. Hence, we can conclude that the presence of the bar does not influence significantly the shape the radial profile of w_g , regulated by the term $b(\Delta t)$, however it has an effect on how the normalization term $A(\Delta t)$ increases with the timestep and in particular leads to slower-than-diffusion behaviour. Regarding the quantity w we recover the same exponent in the dependence $w \sim \Delta t^{\alpha}$ for either subsample as well as for the whole sample.

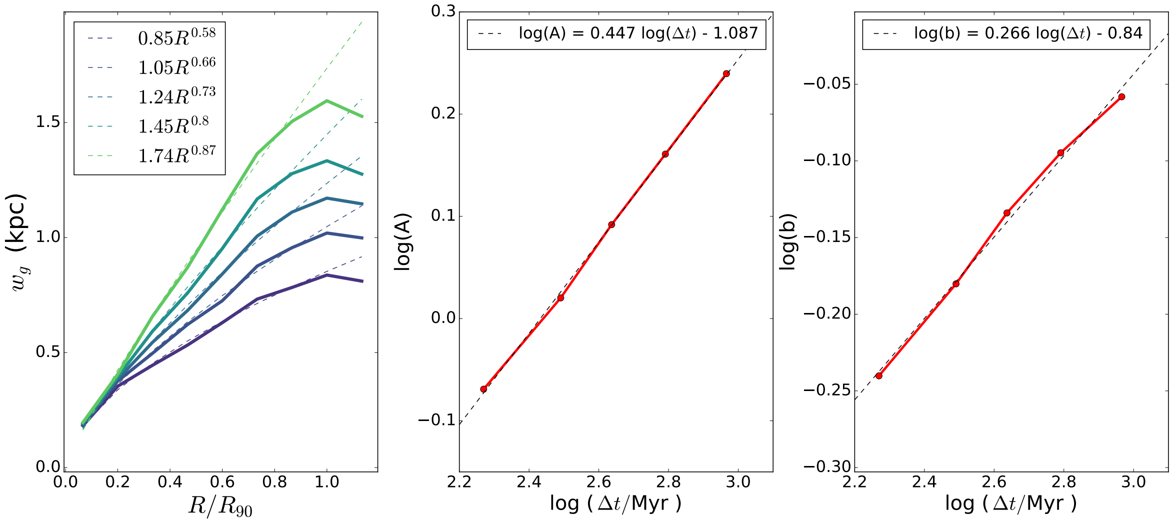

Figure 3.17: Left panel: Power law fits to the radial profiles of the spread w_g, referring to the spread of the ΔR_g histograms, each curve showing a different timestep identical to Figure 3.13. We show the exact values for the fit in the legend. Middle and right panels: We show the logarithmic plots of the coefficient (middle) and exponent (right) of the power law against the time interval Δt as well as the best fit line through the data points with its functional form stated in the legend.

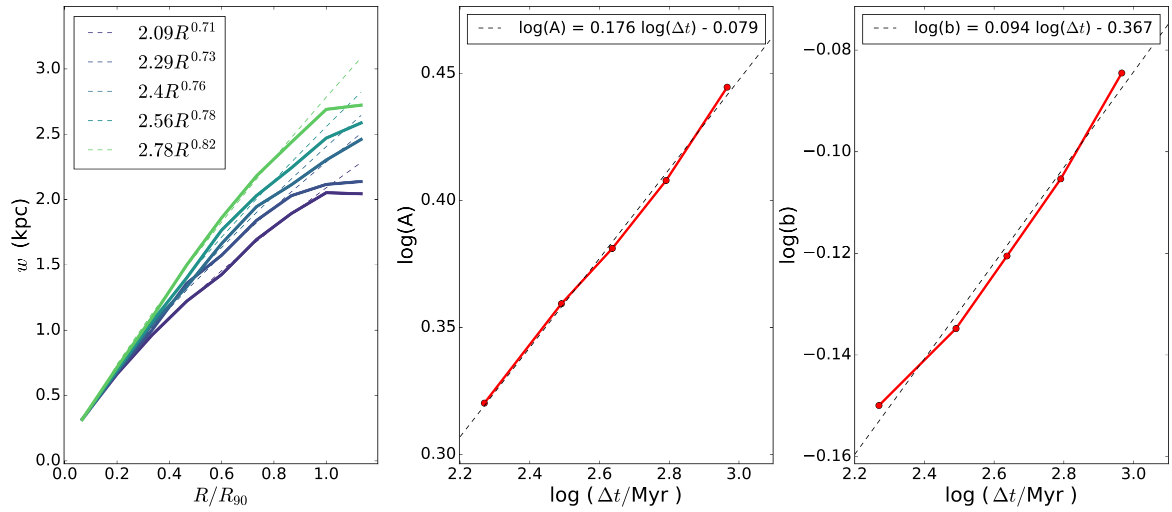

Figure 3.18: Similar to Fig. 3.17, but for the quantity w which refers to the spread of ΔR histograms.

3.5 Discussion and Conclusions

We have investigated the effect of stellar radial migration in 17 disc galaxies from the Auriga simulations. We consider a narrow sample of disc stellar mass, $10 < \log(M_*/M_\odot) < 11$, but with diverse properties in disc kinematics, radii and bar strengths, as well as different evolutionary histories in terms of merger events.

We have measured the amount of radial migration in our simulations by (1) comparing the radii of disc stars at $z = 0$ with their birth radii, and (2) comparing changes in galactocentric radii and orbital guiding centres between pairs of snapshots spanning varying periods of time. The former study allows us to make conclusions about the cumulative effect of migration in the observable quantities of the disc. We note that naively averaging over the difference between birth and present day radius yields values close to zero but in further analysis we see that this is due to the net effect of stars moving both inwards and outwards from their birth positions. In systems with strong bars, we find an excess of “positive migrators” (Fig. 3.5), indicating stars that have been ‘pushed’ to the outer disc because of the interaction with the bar. This feature is similar to that shown in Roškar et al. (2008) (although their simulated disc does not develop a bar). Minchev et al. (2014) also presents a similar result for the guiding radii of the stars. We have reproduced our Fig. 3.5 in terms of guiding radii instead of galactocentric radii but the differences are negligible.

We have also probed into the relation of the age of the stars at redshift zero to the amount that they have migrated using the histograms of $\Delta R = R_{z=0} - R_{birth}$ in different age and radius bins, quantifying the migration as the width of these distributions. For some systems (e.g those with quieter merger histories), we find that these histograms can be reasonably fit with a Gaussian function. However, for other systems, we find deviations in the wings of the distributions (especially in the inner regions of our simulated discs) which are not conducive to a simple Gaussian fit. Nevertheless, the histograms widen with both increasing stellar age and larger radius for all rings in the studied galaxies. We found average values of the age-$\sigma_{\rm migr}$ dependence that are consistent with the model proposed by Frankel et al. (2020); the predicted range of values of this model lie within the scatter of our simulated relations, albeit with a slightly steeper slope compared to our median relation.

We further identify that there is a radial dependence in the normalization and position of the peak of the distributions with respect to the centre of the initial ring of selection. Verma et al. (2021), using some of the same Auriga halos in their study, find upper limits for the radial migration of 2.21 kpc for stars with age less than 4 Gyr and 3.7 kpc for stars with ages between 4-8 Gyr in the solar neighbourhood. Although we do not use the same age bins we find that for younger stars (<3 Gyr) the mean migration strength varies between 1-2.5 kpc depending on the radial bin.

In Auriga, the stellar age radial profiles are not significantly affected by migration in a considerable number of the cases. However, we do observe in a subset of the systems a flattening of the age gradients at larger radii.

In terms of the metallicity gradients (Fig. 3.9), we observe a dependence similar to Minchev et al. (2013) (Fig. 5 of that paper) where the gradients for the younger stellar populations are at most marginally affected by migration but for the older stars there is a more significant flattening in the majority of cases. This age effect is clearly shown in our simulations and we further present possible correlations of the amount of flattening with the stellar mass and the strength of the bar in the disc. However, overall metallicity profiles (i.e. accounting for stars of all ages) do not appear to evolve strongly with cosmic time in Auriga.

In the second part of our analysis, we focused on pairs of snapshots spaced by a time difference Δt, so that we can extract information about how the migration process proceeds in given time intervals. We allow the Δt to vary between 60 Myr and 1 Gyr. The two measures that we use to describe the histograms, the median shift ($\overline{\Delta r}$ or $\overline{\Delta r_g}$) and the spread (w or w_g), can be used in combination to give a description of the migration process. We find that the values for the median shifts are in any case smaller compared to the spread and highly variable from halo to halo, indicating a secondary effect. However, we deem that is more physically motivated to use the quantities w and w_g as main indicators of the migration since this scatter measure contains more information about the radial motions of the stars which are selected in the given ring compared to the median. Still, it must be noted that we find average negative values for the median shift radial profiles, showing a small inwards median motion of the selected stars in the given rings. Although this looks contradictory to the standard picture of stars migrating to and populating the outer parts of discs, it is reconciled by considering that there is always a rather symmetric spread around the median value meaning that we have in all cases a considerable number of stars that have migrated outwards between two snapshots.

We find that, when considering the changes of the guiding centres of the stars, there is a migration process that follows a diffusion-like evolution. The exponent of the timestep dependence is not exactly 0.5, as would be expected for pure diffusion, but slightly lower. This 'slower' diffusion could be attributed to the fact that we average over our different systems with different structural properties and lifetime evolution. In individual halos, we do observe exponents that closely match 0.5. As stated before the diffusion exponent is recovered if we consider only the weakly-barred halos in our sample but the strongly barred systems seem to be regulated by a slower-than-diffusion timestep evolution following $w_g \sim \Delta t^{0.38}$. Indeed, most of the halos in Fig. B.3, that have exponents closer to 0.5 do not have a strong bar in their centre. The mechanism due to which the presence of a strong bar leads to this behaviour could be explore in a future study. The corresponding time evolution of the changes in the galactocentric radii is flatter and less clear than the respective one for the guiding centres. Although it can still be parametrized, we are cautious about any strong statements on the physical significance of this result because there are several processes that could contribute to changes in the galactocentric radii that would require much deeper analysis to disentangle them cleanly.

The parametrizations we present in Eq. 3.2,3.3 describe how strongly stars migrate out of a ring as a function of the radial location of the ring as well as the timestep that is used to between the initial and final observations of the stellar positions. However, as shown in Fig. 3.16, there are secondary dependencies that contribute to scatter about the median relation that we provide. For this figure, we have used a fixed time interval of $n + 10$, but the dependence is similar for all other selections of $n + m$ when $3 < m < 15$. In the case of considering changes in guiding centres, we find that our sub-sample of barred systems has consistently higher values of w_g than the weakly-barred systems, of the order of 30 per cent in the middle parts of the disc. We must caution that the criterion we choose to distinguish between strongly/weakly barred systems (namely, systems with A_2 above/below 0.3) is at some level arbitrary. However, we have tested that if we instead split the sample into three sub-samples with max(A_2) < 0.2 as weakly barred systems, 0.2 < max(A_2) < 0.4 as intermediate and max(A_2) > 0.4 as strongly barred, we find that the mean radial profiles of w_g and $\overline{\Delta r_g}$ for the intermediate sub-sample lie in between the other two. This indicates that our results are consistent with a continuous dependence based on the value of the bar strength. The stellar age adds another source of scatter, with stars in the youngest age bin showing higher values by 20-40 per cent, depending on the radius, compared to those in the oldest age bin. This is similar for both the strongly and weakly barred sub-samples, implying that this source of scatter is independent of the presence of a bar.

In terms of the overall description of radial migration, we do not give distinct parametrizations that each describe the effects of 'churning' and 'blurring' as it has been presented, for example, in Schönrich & Binney (2009) but we can indirectly associate our computed quantities with these suggested modes of stellar migration. The quantities w_g and $\overline{\Delta r_g}$ show the amount of change of the guiding centres, hence the change of orbital angular momentum of the stars, which is predominantly related to the process of 'churning', however the w and $\overline{\Delta r}$ are more general and incorporate information about all possible processes that can result in the change of the orbital radius of a stellar particle.

Indeed, we find that if we create similar histograms in terms of the changes in angular momentum Δl_z and extract the related quantities w_{l_z} and $\overline{\Delta l_z}$, we see that there is a very tight correlation between the corresponding quantities for the guiding centres, as shown in Fig. 3.19 This is expected, as by construction the change of the guiding centre is due to a change in the angular momentum of the star. A correlation between w_{l_z} and w is present, although looser than the one with respect to w_g. This is an indication that the quantity w encapsulates the information from w_g, as well as some additional scatter that can be associated with the 'blurring' process, which describes the changes in the epicyclic amplitudes on top of the effects that change the angular momentum of the star. On the other hand, there is no correlation at all between $\overline{\Delta l_z}$ and $\overline{\Delta r}$. Whereas there is a median change in the galactocentric radius of the stars selected in the ring, this does not result exclusively from a change in the angular momentum, and this is why a correlation does not arise.

Finally, it must be noted that the parametrizations that we extract are calibrated in our available sample, therefore they are describing the migration process at systems that are comparable in size to our Milky-Way but may not be readily available to disc galaxies of different mass range.

All in all, in this study we find that:

- The average change in the radius for a stellar particle over its lifetime, $\langle \Delta R \rangle$, is close to zero for all our systems. However, this is due to the fact that stars experience both negative and positive migration in comparable amounts which cancel out to a close-to-zero average. The typical star experiences a migration of the order of 2 kpc.

- At $z = 0$, we find that older stars (9-12 Gyr) have experienced up to twice the amount of migration compared to newly formed stars (0-3 Gyr). We find a clear age dependence in the migration strength as well as a radial dependence. Stars that have been born at larger radii show broader distributions of $z = 0$ radii, regardless of their $z = 0$ age.

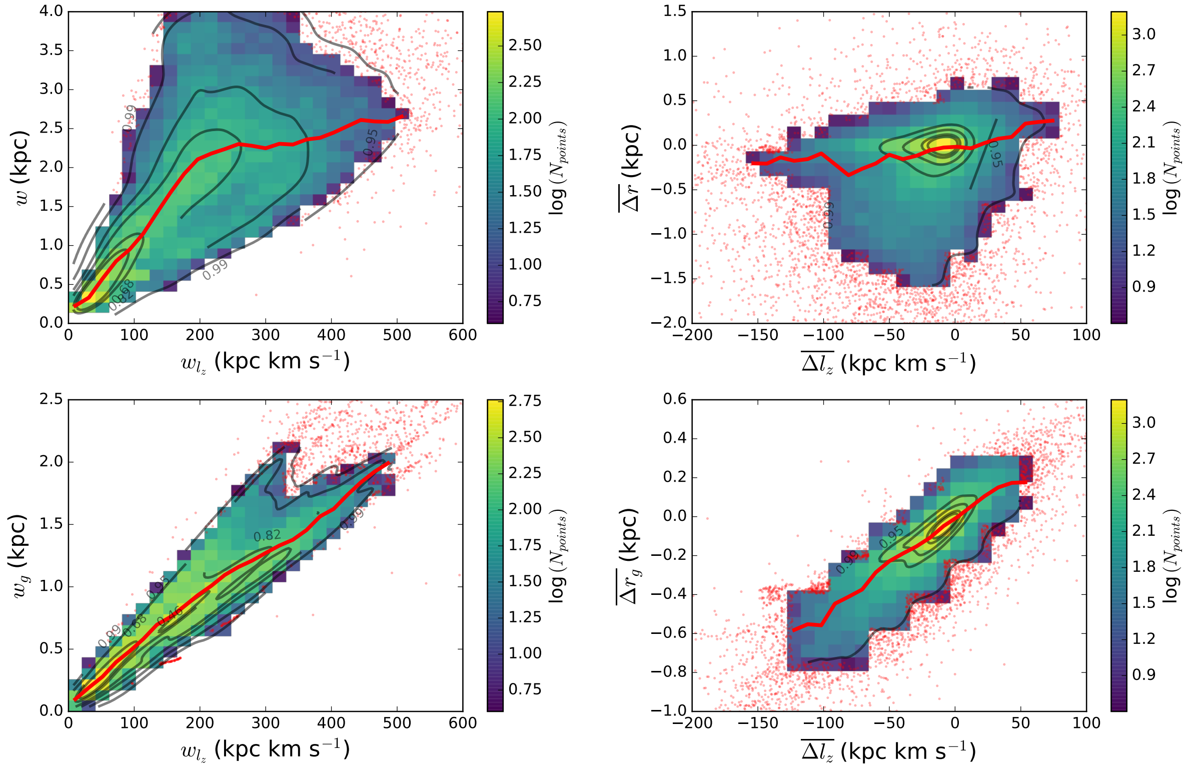

Figure 3.19: The quantities describing the histograms of Δr (top) and Δr_g (bottom) plotted against similarly obtained quantities describing the histograms of the change in angular momentum Δl_z of the stars. We overplot the median lines in red and the density contours in the density colourmaps while the red data points lie outside the 99th percentile contour. We find very strong correlations between the guiding centre changes and angular momentum changes. This is not true for the galactocentric radii changes, and in particular there is hardly any correlation between the median shifts $\overline{\Delta r}$ and $\overline{\Delta l_z}$.

- Stellar migration has a varied effect on the age profiles of the discs at $z = 0$, depending on the particular halo, but it does not affect the scatter around the mean stellar age at a given radius.

- There is no imprint of migration on the total metallicity profiles or the profiles for young stars (< 3 Gyr), but we find significant flattening of the profile gradients in many systems for the older stellar populations. The extent of the flattening is correlated with the presence of a bar in the disc.

- We create distributions of the change in the galactocentric radius Δr and the change in guiding centre Δr_g between two simulation snapshots for the stars within different annuli and quantify them using a measure of their spread w and w_g, and a measure for their median $\overline{\Delta r}$ and $\overline{\Delta r_g}$, respectively. This shows that w and w_g have a power law radial dependence, increasing in the outer regions of the discs as well as a dependence in the time interval between the two snapshots. We present parametrizations that describe these effects. w_g appears to approach a diffusion process at the outermost rings but there is significant halo-to-halo variability.

- $\overline{\Delta r_g}$ correlates exactly with changes in the orbital angular momentum $\overline{\Delta l_z}$ of the stars, as expected in the 'churning' process. $\overline{\Delta r_g}$ is uncorrelated to $\overline{\Delta l_z}$, being a more random measure that includes the additional effect of 'blurring'.

- Combining the findings presented in Figs. 3.10,3.12, and 3.16 we argue that in our sample the systems with a stronger bar are associated with a stronger migration of the stellar particles. This is manifested both in terms of larger values in the changes of guiding radii, Δr_g as well as producing shallower slopes in the metallicity profiles for older stellar populations.

We note that our results are subject to the limitations of the Auriga galaxy formation model. While dynamical interactions of the stellar particles with the bar are accurately captured, smaller scale effects that could result in stellar migration, such as scattering with molecular clouds, cannot be accounted from the modelling of the ISM. We aim to introduce and test the parametrizations for stellar migration in the latest version of the L-Galaxies semi-analytic model of galaxy formation (Henriques et al., 2020; Yates et al., 2021). Here, we present a basic form of such possible parametrizations, focusing on the radial dependence of the migration strength which can be implemented directly into the radial ring model of L-Galaxies. This will allow stars to migrate from ring to ring based on the radial position in each snapshot. As we mention above, the secondary effects of stellar age or bar strength could be also implemented as a scatter around the median radial dependence. Furthermore, it would be of interest to extend this study to discs of smaller masses in order to compare our findings.

Chapter 4

Radial flows in the L-Galaxies semi-analytic model

In this chapter we present a preliminary application of the parametrizations that were derived in the previous two chapters in the L-Galaxies model.

4.1 L-Galaxies Model

L-Galaxies or the 'Munich semi-analytic' model is one of the pioneering SAMs and includes one of the most comprehensive descriptions of galaxy formation. This has emerged from a series of model versions by White & Frenk (1991), Springel et al. (2001), Springel et al. (2005), Croton et al. (2006), De Lucia & Blaizot (2007), Guo et al. (2011), and Henriques et al. (2015), each of which introduced improvements to the model. The current version of L-Galaxies is presented in Henriques et al. (2020) while the model is still continuously updated as illustrated by the two recently created branches by Yates et al. (2021) and Ayromlou et al. (2021).

Regardless of the model version, a galaxy in L-Galaxies is built inside dark matter halos and subhalos that are drawn from the merger trees of either the Millennium (Springel et al., 2005) or the higher resolution Millennium-II (Boylan-Kolchin et al., 2009) simulations. These merger trees are created using the SUBFIND algorithm (Springel et al., 2001; Dolag et al., 2009) which identifies all gravitationally bound substructures in the dark matter. Galaxies are separated into three 'types' according to their subhalo status in the merger trees. "Type 0" galaxies are the central galaxies of each main halo while "Type 1" refers to the satellite galaxies which are within bound subhalos. Finally, "Type 2" galaxies refers to objects which have been stripped of their dark matter subhalo but have not yet merged with the central galaxy.

Each galaxy is modelled by a number of mass reservoirs that represent the different components of a real galaxy. At any time the baryonic mass associated with a particular galaxy can be in one of the following states:

1. 'Hot gas'
2. 'Cold gas'

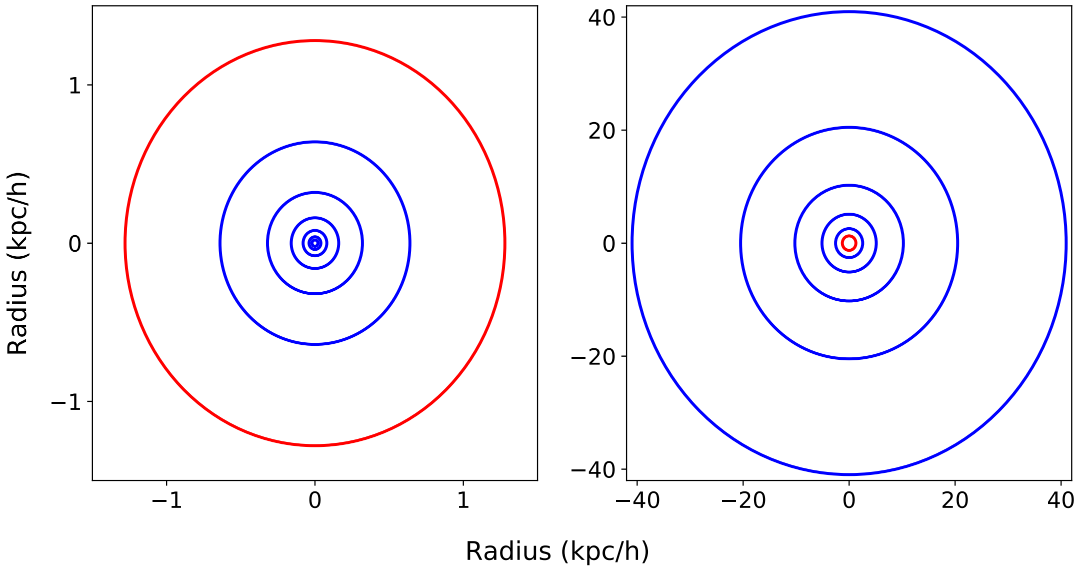

Figure 4.1: The ring structure in the L-Galaxies model. Shown with blue in the left panel are the inner six rings, and in the right panel the five outer rings. In both panels the ring at 1.6 h^{-1}kpc is plotted in red.

3. ‘Stellar disc’
4. ‘Stellar bulge’
5. ‘Ejected Gas’
6. ‘Central Black Hole’

Furthermore, starting with the Henriques et al. (2020) version of L-Galaxies, a radial ring structure has been incorporated in order to allow the modelling and observational comparison of radial profiles in galactic discs. In the default model, both the ‘stellar disc’ and the ‘cold gas’ reservoirs are divided into 12 rings spaced logarithmically in radius with the following configuration.

$$r_i = 0.01 \times 2^i \quad [h^{-1}\text{kpc}];\ i \in [1, 12] \tag{4.1}$$

where r_i is the outer edge of each ring. Although we are not concerned with the ‘stellar bulge’ in this work, we note that a separate ring structure also exists for this component.

In the remainder of this section, we briefly introduce some of the main physics modelling prescriptions in L-Galaxies but for a complete description of the model we point to the supplementary material of Henriques et al. (2020).

- The galaxy building process begins with populating dark matter halos with baryonic matter. The initial baryonic mass within each halo is decided by the mean cosmic baryon fraction $f_{b,\cos} = 15.5\%$ and the halo mass, and is placed in the ‘hot gas’ reservoir, $M_{\text{hot}} = f_{b,\cos} M_{\text{halo}}$.

The baryon fraction needs to be modified in order to account for the heating from the UV-background radiation:

$$f_b(z, M_{200}) = f_{b,\cos}\left(1 + (2^{\alpha/3} - 1)\left[\frac{M_{200}}{M_F(z)}\right]^{-\alpha}\right)^{-3/\alpha}. \tag{4.2}$$

This primarily affects the smaller mass halos, where this heating prevents baryons from accreting into the halo.

- The amount of gas that moves from the 'hot' to the 'cold' gas reservoir is set by the cooling rate. In L-Galaxies there are two cooling pathways corresponding to (1) a rapid cooling regime at earlier times and in small halos when the cooling time is smaller than the free fall time and the gas settles into a cold disc at the dynamical time of the system, (2) a cooling flow regime for later times and more massive halos where gas is shock-heated at the virial radius, forming a hot atmosphere, and then settles onto the disc at a slower rate regulated by the cooling time (White & Frenk, 1991; Guo et al., 2011). In the first case the cooling rate is given by:

  $$\dot{M}_{\rm cool} = M_{\rm hot}\frac{r_{\rm cool}}{R_{200}}\frac{1}{t_{{\rm dyn},h}} \ ; \ \ r_{\rm cool} < R_{200} \tag{4.3}$$

  and in the second by:

  $$\dot{M}_{\rm cool} = \frac{M_{hot}}{t_{dyn,h}} \ ; \ \ r_{\rm cool} > R_{200} \tag{4.4}$$

  In these expressions, $r_{\rm cool}$ is the cooling radius, which is the radius where the cooling time is assumed to be equal to the dynamical time. The cold gas is assumed to accrete onto the ring structure that represents the disc with an exponential profile regulated by a scale radius dependent on the specific angular momentum and the circular velocity of the halo.

- L-Galaxies includes the creation of molecular hydrogen which is used for the formation of stellar mass. The amount of molecular hydrogen is given by a fraction $f_{\rm H_2}$ that dictates how much of the cold gas is in the molecular and how much in the neutral phase:

  $$f_{\rm H_2} = \begin{cases} \frac{2(2-s)}{4+s}, & s < 2 \\ 0, & s \geq 2 \end{cases} \tag{4.5}$$

  The parameter s is a function of the metallicity Z and the surface density $\Sigma_{\rm gas}$ of the cold gas.

- Star formation follows a Kennicutt-type law (Kennicutt, 1998) where the star formation rate density is proportional to the density of the molecular hydrogen (H_2) divided by the dynamical time of the disc (Fu et al., 2013):

  $$\Sigma_{\rm SFR} = \alpha_{\rm H_2}\Sigma_{\rm H_2}/t_{\rm dyn}. \tag{4.6}$$

- The inflow of gas between the different rings follows the prescription by Fu et al. (2013). In this work the authors invoke that the rate of change of the angular momentum of the gas is proportional to its angular momentum, i.e. $\frac{\mathrm{d}L_{\text{gas}}}{\mathrm{d}t} = CL_{\text{gas}}$, which yields an expression for the inflow velocity that is proportional to the radial distance of the ring from the centre of the disc,

  $$v_{\text{inflow}} = \alpha r, \tag{4.7}$$

  where α is a free parameter of the model. This proportionality means that the inflow velocity goes to zero in the central parts, and depending on the choice of α one obtains values of 10-20 km s^{-1} at the outskirts of a typical disc at around 15-20 kpc.

- During stellar evolution, a significant amount of energy is released to the surrounding medium by stellar winds and supernova explosions. In L-Galaxies these processes are modeled as an energy input that a) is heating the cold gas moving it into the 'hot' reservoir, b) is heating the 'hot' component directly and c) moves 'hot' gas out of the galaxy into the 'ejected gas' reservoir.

  The energy released by the stellar winds and supernovae is:

  $$\Delta E_{SN} = \epsilon_{\text{halo}} \Delta M_{*,R} \eta_{SN} E_{SN}, \tag{4.8}$$

  where $\Delta M_{*,R}$ is the mass returned to ISM, η_{SN} the number of supernovae per $\Delta M_{*,R}$, and E_{SN} the energy of 10^{51} erg released by each supernova. Finally, ϵ_{halo} is a free parameter. The mass that moves from the 'cold' to the 'hot' reservoir is $\Delta M_{\text{reheat}} = \epsilon_{\text{disc}} \Delta M_{*,R}$ where ϵ_{disc} is another free parameter of the model. The energy required to drive this mass transition is $\Delta E_{\text{reheat}} = 0.5 \Delta M_{\text{reheat}} V_{200}^2$. ΔE_{reheat} is subtracted from ΔE_{SN} and any residual energy is used to expel gas into the 'ejected gas' reservoir.

- Gas from the 'ejected gas' reservoir is allowed to be reincorporated into the 'hot gas' atmosphere with a rate of reincorporation:

  $$\dot{M}_{\text{reinc}} = \frac{M_{\text{ejec}}}{t_{\text{reinc}}}, \tag{4.9}$$

  where the reincorporation time, t_{reinc}, is inversely proportional to the mass of the halo.

- The treatment of black hole evolution in L-Galaxies is mainly based on Croton et al. (2006). The central black hole grows primarily whenever a merger of two galaxies occurs in the model. Apart from summing the masses of the pre-existing black holes in each of the two galaxies, the merger causes cold gas to be funnelled into the central regions, feeding the black hole in what is called *quasar mode*. Then the black hole mass increases by:

  $$\Delta M_{BH} = \frac{f_{BH} (M_{\text{sat}}/M_{\text{cen}}) M_{\text{cold}}}{1 + (V_{BH}/V_{200})^2}. \tag{4.10}$$

  It is evident from this expression that the mass increase depends on the mass ratio of the merger, the amount of cold gas in the two galaxies, and the virial velocity V_{200} of the halo of the central galaxy. The quantities with the subscript BH are free parameters of the model.

Besides the *quasar mode*, L-Galaxies also considers a *radio mode* accretion onto the black hole. In this mode, gas from the 'hot gas' component directly feeds the black hole over long time scales. Since there is a rate of increase of the black hole mass, energy is released producing the radio mode feedback. This energy enters into the 'hot gas' reservoir, essentially reducing the total cooling rate. In particular, the amount of energy is given by:

$$E_{BH} = \eta \dot{M}_{BH} c^2, \tag{4.11}$$

where

$$\dot{M}_{BH} = k_{AGN} \left(\frac{M_{\rm hot}}{10^{10} M_\odot} \right) \left(\frac{M_{BH}}{10^8 M_\odot} \right) \tag{4.12}$$

and c is the speed of light, η the efficiency parameter set to 0.1, and k_{AGN} is a free parameter.

- The merger of the baryonic components of the galaxies lags behind the dark matter halo merger by a time set by the dynamical friction time-scale:

$$t_{\rm friction} = \alpha_{\rm friction} \frac{V_{200} r_{\rm sat}^2}{G M_{\rm sat} \ln\Lambda}, \tag{4.13}$$

where $\ln\Lambda = \ln(1 + M_{200}/M_{\rm sat})$ is the Coulomb logarithm. Because all galaxies have the same ring structure, when two of them merge the masses in gas and stars are added between the corresponding rings. Moreover, in L-Galaxies a merger triggers a burst in star formation which forms new stellar mass at each ring given by:

$$M_* = \alpha_{\rm burst} \left(\frac{M_1}{M_2} \right)^{\beta_{\rm burst}} M_{\rm cold}, \tag{4.14}$$

where M_1 and M_2 are the baryonic masses of the two objects, $M_{\rm cold}$ is the cold gas mass in the ring and $\alpha_{\rm burst}, \beta_{\rm burst}$ are free parameters.

- The bulge formation and growth in L-Galaxies can result from two channels. The first is after merger events where the mass of the formed bulge is computed from energy considerations with regards to the binding energies of the two merging systems. Bulges can also grow via the secular evolution of the disc by invoking that a disc instability forms a bar that eventually buckles to add to the bulge component. The criterion for the disc instability in the model depends only on the stellar mass and scalelength of the disc:

$$V_{\rm max} < \sqrt{\frac{G M_*}{3 R_*}}. \tag{4.15}$$

When this criterion is satisfied, mass is transferred from the 'stellar disc' to the 'stellar bulge' component.

- L-Galaxies contains a comprehensive galactic chemical enrichment model presented in Yates et al. (2013). In particular, eleven chemical elements are tracked (H, He, C, N, O, Ne, Mg, Si, S, Ca, Fe) which are products of the stellar evolution processes via stellar winds and supernovae (SNe-Ia and SNe-II) explosions. The rate of ejection of a given element X at some time t is:

$$e_X(t) = \int_{M_L}^{M_U} M_X(M, Z_0)\psi(t - \tau_M)\phi(M)\mathrm{d}M, \tag{4.16}$$

where ψ is the star formation rate at the star's birth, ϕ gives the number of stars in given mass, Z_0 is the initial metallicity and M_X is the mass of element X per star.

Besides the aforementioned modelling prescriptions, we note that in L-Galaxies there is also treatment of environmental processes such as tidal and ram-pressure stripping (Ayromlou et al., 2021), and a model for the dust (De Lucia & Blaizot, 2007) which includes extinction due to the interstellar medium and molecular clouds. Including the extinction factor is important in correctly computing the colours of galaxies.

One can observe that the L-Galaxies model has a large number of free parameters. All these parameters influence the evolution of the galaxies, creating a multidimensional parameter space that needs to be searched in order to identify which parameter values produce the model output that reproduces observations best. L-Galaxies uses a Monte Carlo Markov Chain (MCMC) algorithm to evaluate the best fit values and the uncertainties for the set of parameters. Following Henriques et al. (2020), the observational constraints that are usually used to calibrate the model are the stellar and HI mass functions at redshift $z = 0$, and the fraction of the red/passive galaxies as a function of stellar mass at two different redshifts ($z = 0, z = 2$).

In this work we are only concerned with the modelling of the inflow of gas which we aim to update by using as input our analysis of the Auriga simulations. Furthermore, there is no treatment in the current version of the model for stellar migration at all. Whereas gas is exchanged between rings, stars remain exclusively in the ring that they were formed. Hence, we also aim to introduce a prescription with similar functionality to the gas inflow recipe that will allow stars to move between the rings.

4.2 Algorithm description

In the previous two chapters we presented parametrizations that describe how the radial migration of stars and the radial inflow of gas behave in the selected sample of disc galaxies in Auriga. These parametrizations need to be adapted for an integration in the L-Galaxies model, and in this section we describe the algorithmic implementation of the resulting numerical relations in the code.

We start by recalling the equations from the earlier chapters, for the gas flows:

$$w_{\mathrm{gas}} \ / \ \mathrm{kpc} \ = \left[35.9\, R_{sc}^{1.1} + 21.8 \left(f_{\mathrm{acc}} * \frac{60\mathrm{Myr}}{\Delta t} \right) - 2.8 \right]^{1/3} \Delta t^{1/3}, \tag{4.17}$$

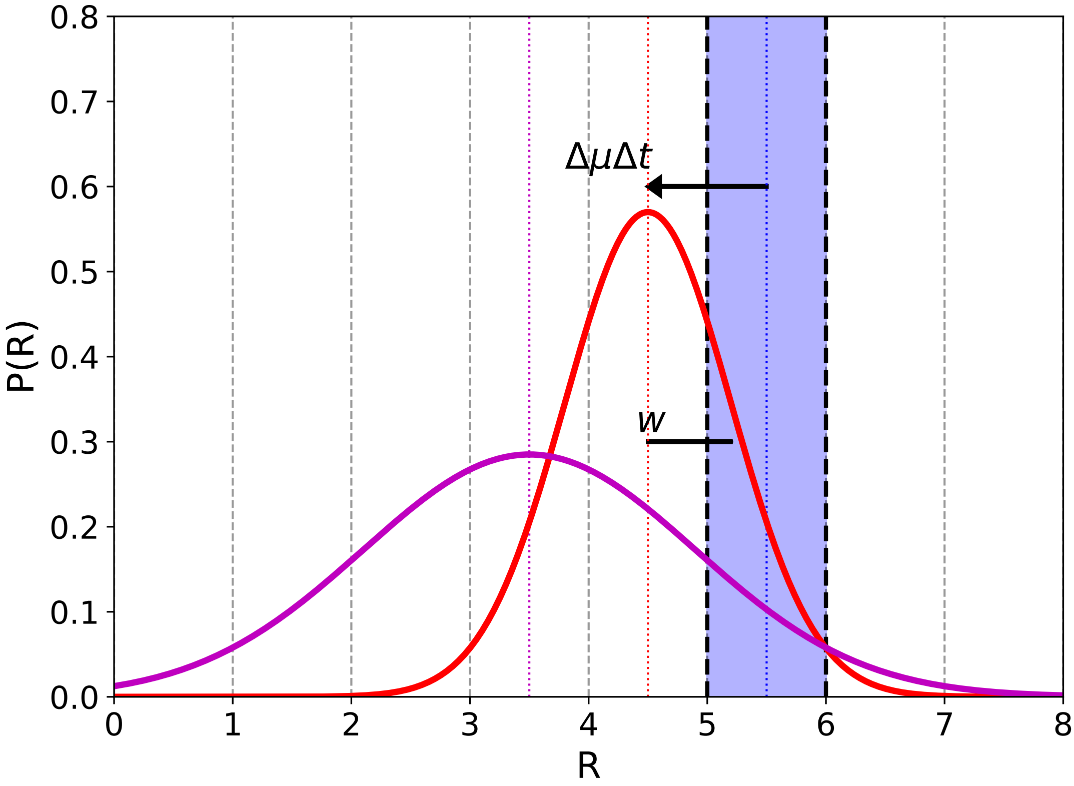

Figure 4.2: Schematic representation of how we distribute the material using the Gaussian functions. In this toy example, material is moved out of the initial ring (shaded in blue) and is distributed across the different radii with the probability function in red. We note in this plot the significance of the parametrized quantities w and $\Delta\mu$ which control, respectively, the width and the median of the distribution. Since $\Delta\mu$ is measured in km s^{-1} it needs to be multiplied by a timestep Δt to get a displacement in units of radius. For comparison, the magenta curve has twice the width and the median shift of the red curve.

$$\Delta\mu_{\rm gas}\,/\,{\rm km\,s^{-1}} = \begin{cases} -1.7 - 6.8\,(f_{\rm acc}\,\frac{60{\rm Myr}}{\Delta t}) & \text{if } r \leq 0.75\,R_{sc} \\ -15.9\,R_{sc} - 6.8\,(f_{\rm acc}\,\frac{60{\rm Myr}}{\Delta t}) + 10.2 & \text{if } r > 0.75\,R_{sc} \end{cases}. \tag{4.18}$$

And for the stellar migration:

$$w_*\,/\,{\rm kpc} = \frac{(\Delta t/{\rm Myr})^{0.45}}{12.2} R_{sc}^{((\Delta t/{\rm Myr})^{0.27}\,/\,6.9)}, \tag{4.19}$$

$$\Delta\mu_*\,/\,{\rm km\,s^{-1}} = 0. \tag{4.20}$$

In both processes, the first equation, for w, measures the amount of spreading of the material around some radius. In particular, we have defined w as half of the 16-84 percentile of a distribution, which in the case of a purely Gaussian distribution corresponds to the 1σ interval around the median. On the other hand $\Delta\mu$, which is non-zero only for the gas component, measures the bulk flow velocity of the material, or equivalently, how much has median of the distribution has shifted from the point of origin after a given time period. For the case of the stars, we use Eq. (3.2) for the guiding centres, which are the mean circular radii of a stellar orbit, instead of the corresponding expression for the galactocentric radii.

As mentioned in the previous section, the disc of every galaxy is represented by twelve fixed rings, both for the stellar and the cold gas components. At any snapshot time, we have access to stored arrays which give us information about the stellar and gas mass of each ring. The purpose of our algorithmic design is to decide how much mass is to be exchanged between the rings after every update of the model. In more detail, at the initial time the mass within a given ring is thought to be a top-hat function, evenly spread between the radial boundaries of the ring. After a timestep Δt we postulate that the gas from this particular ring has diffused to radii outside the ring boundaries, following a Gaussian profile. The median and the spread of this new distribution are determined by the values of w and $\Delta\mu$ which we calculate based on the properties of the ring (mainly its radius) before the update of the quantities. The fraction of mass from the initial ring that is outside the ring boundaries is assigned to the other rings depending on how much overlap there is between the distribution function and the 'receiving' ring. The choice of the Gaussian-shaped distribution is motivated by the shape of the distributions that we measured in the Auriga simulation, which in the majority of instances were well approximated by a Gaussian function. We show a basic schematic representation of these distributions in Fig. 4.2, where also the meaning of w and $\Delta\mu$ is more clearly illustrated.

We now present the mathematical formulation of the redistribution process. To begin with, a ring i is centred at a radius R_{cen} and contains mass M_i. Depending on the total mass of the galaxy, which is the sum of the masses in all rings, we compute the radii which enclose 90% and 95% of the total mass. This is necessary because the parametrizations are cast in terms of normalised radii, R_{sc}; for the stellar component $R_{sc} = R_{cen}/R_{90}$ whereas for the gas component $R_{sc} = R_{cen}/R_{95}$. Given the integration timestep Δt of the model and R_{sc} we can then calculate the values for the spread w and the median shift $\Delta\mu$.

These are the required parameters so that we can construct the distribution function f, which gives the probability that mass from the initial ring will end up in any radius r,

$$f(r; R_{sc}, w, \Delta\mu, \Delta t) = \frac{1}{\sqrt{2\pi}\, w(R_{sc}, \Delta t)} \exp\left(-\frac{(r - \mathcal{M})^2}{2\, w^2(R_{sc}, \Delta t)}\right), \tag{4.21}$$

where $\mathcal{M}$ is the median of the distribution expressed as:

$$\mathcal{M}(\Delta\mu, \Delta t) = R_{cen} + \Delta\mu(R_{sc}) \times \Delta t. \tag{4.22}$$

Eq. (4.21) is a normalised probability distribution therefore the integration over all radii should be equal to unity, ensuring that all of the mass M_i has been assigned to a radius within the galaxy,

$$\int_0^\infty f(r; R_{sc}, w, \mathcal{M}, \Delta t)\, \mathrm{d}r = 1. \tag{4.23}$$

In the model we have a certain number of rings with their centres set at specific values at all snapshots. This immediately leads to a discretized, rather than a continuous problem, and Eq. (4.23) should be expressed in a discrete form as well:

$$\sum_j f_j(r_j; w_i, \mathcal{M}_i, \Delta t)\, \Delta r_j = 1. \tag{4.24}$$

The amount of mass that is being been transferred from a given ring i to a ring j is computed as the product of a) the distribution function associated with ring i, evaluated at a radius r that corresponds to the centre of the ring j, and b) the width of the ring j, Δr_j.

We define the quantity inside the sum as:

$$q_{i,j} = f_j(r_j; w_i, \mathcal{M}_i, \Delta t)\, \Delta r_j, \tag{4.25}$$

where $q_{i,j}$ represents a weighting factor that informs us about which fraction of the mass has moved from ring i to ring j.

Because of the discrete nature of this redistribution, and the fact that we deal with a very coarse resolution of only 12 rings, it is expected that in most instances the normalisation condition of Eq. (4.24) is not automatically satisfied. However, it is necessary that mass conservation is obeyed in the code, meaning that all the mass that exits a given ring should subsequently be found in one of the other rings.

Therefore we must enforce the normalisation which we do by adjusting the value of the weights by a correction factor, C, for each ring. Expressed in mathematical notation, we define this factor for every ring i as:

$$C_i = \sum_j f_j(r_j; w_i, \mathcal{M}_i, \Delta t)\, \Delta r_j = \sum_j q_{i,j} \tag{4.26}$$

where C_i can obtain vales different than 1, both larger and smaller. We then compute the corrected weights as:

$$\tilde{q}_{i,j} = \frac{q_{i,j}}{C_i} \tag{4.27}$$

By this construction it then follows that:

$$\sum_j \tilde{q}_{i,j} = \sum_j \frac{q_{i,j}}{C_i} = \frac{1}{C_i} \sum_j q_{i,j} = \frac{C_i}{C_i} = 1 \tag{4.28}$$

Using the weights $\tilde{q}_{i,j}$, we then assign the fraction of the mass that 'originates' from ring i and moves into ring j as:

$$m_{i \to j} = \tilde{q}_{i,j} M_i \tag{4.29}$$

After the redistribution process, the mass at the 'receiving' ring j is simply the sum of all the masses transferred from the other rings, that is:

$$M_j = \sum_i m_{i \to j}. \tag{4.30}$$

The same equations apply for the gas mass and stellar mass in each ring, as well as the masses of the individual metals and elements that are simulated in L-Galaxies.

The only modification in the redistribution algorithm between the gas and stellar components is that the stellar migration parametrization includes only a spread quantity and not a shift to the median. Under this condition the equation for the new median of the distribution is simply given by $\mathcal{M} = R_{cen}$, where R_{cen} refers to the ring out of which the mass is originating.

4.2.1 Probability at $R < 0$

From a mathematical standpoint any Gaussian function is well-defined and extends to infinity in both directions. However, in our application our independent variable is the radius from the centre of the galaxy, at $R = 0$, so negative values have no physical meaning. The algorithm that we use deals naturally with this issue. When there is a fraction of the distribution that enters negative radii, it follows that the sum of the weights in the 12 rings will be less than 1. The difference will be accounted for by the correction factor, which will scale the weights accordingly. Essentially this creates a fictitious outwards flow of material, because the weights of all the rings at $R > 0$ will be increased. This issue is quite negligible for the majority of the rings because the distributions are sufficiently peaked so that only a negligibly small fraction gets negative radii assigned. However, this is not always the case for the three innermost rings. The probability distributions at these very small radii are extremely peaked (very low values of w) and because of the negative bulk flow ($\Delta\mu$) the median of the distribution can end up at a negative value. As a result the area under the curve is predominantly at $R < 0$ and there is little contribution at $R > 0$ where our rings are located. It then follows that the correction factor C_i, being the sum of the weights at all rings, becomes unrealistically small. We alleviate this problem by imposing a condition that when the median $\mathcal{M}$ becomes negative, we set it at the centre of the innermost ring at 0.01 kpc. This issue is much less pronounced in the stellar component since the median always remains at the centre of the rings.

4.2.2 Probability at $R > R_{\text{gal}}$

A similar problem is encountered on the other end of the radial ring structure, where the probability distribution extends at a radius that is larger than the radius of the last ring in L-Galaxies. To put a concrete number, that is whenever $R > R_{\text{max}} = 40.96\ h^{-1}$kpc.

In contrast to what was discussed in the previous paragraph, the outer boundary affects primarily the treatment of stellar migration. In the case of the gas radial flows there is an inwards bulk flow of mass with the inflow velocity ($\Delta\mu$) increasing linearly with radius. Hence, in the outermost ring, despite the Gaussian distribution being much broader, it is also more strongly shifted inwards. As a result only a small fraction of the mass in the tail of the distribution falls at $R > R_{\text{max}}$, and the correction factor C_i remains reasonably close to one. However, in the stellar migration treatment there is no net inwards flow but rather only a spreading of the material around the centre of each ring. Therefore, for the outermost rings there can be a considerable fraction of the mass that has moved outside the maximum ring radius. Because of the scaling that we apply with the correction factors, the mass that has been moved beyond R_{max} will artificially be 'compensated' by increasing the values of the masses in each of the rings within the disc. The eventual state can be a non-physical build up of mass in the outer ring. It must be noted that this issue is not too problematic in the greater picture of the model because the stellar profiles in galactic discs follow an exponential radial profiles and thus only a small fraction of the mass is located at the outer rings. A potential solution that can be explored in the future is to consider a secondary 'ejecta' reservoir which will store the mass that has barely exited the ring structure, and use some mechanism that will more smoothly re-incorporate this mass to the rest of the rings.

4.2.3 Modification to the semi-analytic modelling prescriptions

The incorporation of a recipe obtained from a simulation to a different model is not a trivial task. The most challenging aspect in our application is the default ring structure in L-Galaxies which places much emphasis on the innermost regions of the galaxy. Because of the logarithmic spacing, 6 out of the 12 rings are centred at a radius less than 1 kpc. In our studies with Auriga, we similarly used a ring decomposition for the simulated discs which was however linearly spaced. As a result, our innermost ring was placed around the 1 kpc region from which it follows that we did not realistically probe any regions further inwards. Therefore the interpolation of the equations within the inner kpc should be treated with caution.

The profile for the median shift $\Delta\mu$ that is described by Eq. (4.18) will tend to a non-zero value with $\Delta\mu < -1.7$ km s^{-1} as $R \to 0$. We argue that it is not physically sound to adopt this interpolation, and instead it must be imposed that $\Delta\mu \to 0$ as $R \to 0$. Because we lack any input from our analysis in Auriga, we resort to using the existing inflow recipe of L-Galaxies at these inner radii since that implementation naturally tends to zero as we approach the centre of the galaxy. Hence we use $\Delta\mu = -\alpha r$ km s^{-1} when $R < 1$ kpc.

In the case of the spreading parameter w, we do interpolate safely to low radii as the function monotonically increases with radius and approaches zero at the centre. That applies both to w_{gas} and w_*. The modification that needs to be implemented in the case of w is a scaling to the width of the ring. The rings that were used to extract the parametrizations were of equal width of about 1 kpc. In the L-Galaxies structure there is an extreme difference between the width of the inner and outer rings spanning three orders of magnitude. We find that if we blindly apply the parametrization for w, material diffuses too much in the inner rings and does not spread enough in the outer rings with the extreme case in the largest/outermost ring where no material spreads beyond the ring boundaries. Upon testing with higher resolution runs and several scalings of the values of w, we conclude that it is reasonable to scale the value of w by the width of the respective ring. Hence, the quantity that enters Eq. (4.21) is $\tilde{w} = w/\Delta R_{ring}$, in place of w.

4.2.4 Modification to the ring resolution

We have conducted several tests with a different ring structure (e.g. linear spacing) and number of rings, the presentation of which is beyond the scope of this thesis. Nevertheless, we note that the model yields different results when we have a higher radial resolution (i.e. larger number of rings) not only in the radial profiles but also in the global properties of galaxies (see following section 4.4). This is not surprising as we expect that to some extent all recipes that operate on a ring level will perform differently in higher resolution. Ideally, one would like to achieve as high resolution as possible for the radial decomposition of the disc. However, there is a significant computational cost associated with adding more rings to the model since then every calculation needs to be repeated considerably more times. In particular, we find that tripling the number of rings causes the code to run three times slower. This is still acceptable when using a subset of trees but if the full Millennium box is to be used then the increasingly longer running time cancels the advantage of a semi-analytic model which is to run much faster compared to a full scale numerical simulation.

We have employed a partial workaround by increasing the ring resolution only within our recipes for the radial gas flows and stellar migration instead of applying it globally to the rest of the code. We input the same radial ring structure from Eq. (4.1) and because the resolution in the 8 inner rings is already high enough we preserve the structure for them. The width of the outer four rings is a factor of 2 larger than the previous ones so we split each ring by dividing by this factor and we create equal radial width annuli. That is to say the 9th ring is split in 2, 10th in 4, 11th in 8 and the outermost 12th ring into 16 subrings. The mass of the parent ring is also split equally between each of the subrings. We then apply our recipes to this higher resolution structure which in total has 38 rings. The new resolution is $\sim$ 1.5 kpc in the outer radii, comparable to our analysis in Auriga. This implementation reduces the running time by 50% compared to initializing the model with 38 rings.

4.3 Single galaxy toy model

As we discussed before, L-Galaxies is an extensive code that models several physical processes that happen during galaxy formation and evolution. Our additions are incorporated as part of this code and perform the radial transport of mass while at the same time gas accretion, star formation, AGN and stellar feedback and mergers are triggered by the corresponding modelling prescriptions. Naturally, these processes are interconnected in a non-linear fashion, and the output of one recipe can immediately affect another. When testing for the robustness and accuracy of our modelling it is preferable to isolate its effect, therefore we have created a simple toy model of a single ‘galaxy’ where the only process that operates is the transport of mass between different rings. Because of the similar implementation of the stellar and gas radial transport, for this toy application we use only one mass component, and in particular we assume the parametrizations that describe the gas transport as they include non-zero bulk inflow therefore providing a more generalised picture.

We use the same code that is written for the recipe in L-Galaxies with minor modifications to allow it to function outside the full model, and we set arbitrary initial conditions for the mass at each ring. Within this framework, we can also choose the number of time iterations, the timestep Δt that we desire while the ring structure can also be modified for further experimentation.

A most useful check is to confirm that a diffusive process is simulated by our toy code. For that purpose we employ a setup with a large number of rings to improve the resolution, and we populate with gas only one of these rings at $t = 0$. The initial gas distribution in this example is a narrow top hat which according to the functionality of the code should evolve with time into a Gaussian-shaped distribution which becomes broader and more shifted to inner radii at every timestep. This is shown in Fig. 4.3 where we indeed see that the initially spiked distribution broadens with time and moves inwards owing to the $\Delta\mu$ parameter for the bulk inflow.

In order to approximate the functionality of the recipes in L-Galaxies, we copy the ring structure that is used in the model’s main code, that is 12 rings with a logarithmic spacing (Eq. 4.1). We choose arbitrarily a monotonically decreasing initial mass profile with the form $M_i = 1000 \times (12 - i)$. The exact shape of the profile is not important in this application. Finally we assume a timestep of $\Delta t = 15$ Myr which is comparable with the integration timestep in L-Galaxies.

In Fig. 4.4 we show how the mass and surface density evolve from the initial profile after integrating for 3 Gyr (that is 200 iterations). We present two separate versions of the parametrizations, a) where we assume that the bulk velocity is a non-zero constant at $R = 0$ and b) where the bulk velocity tends to 0 at $R = 0$ as in Fu et al. (2013). Comparing the two results we see a difference in the evolution of the profiles for the inner rings during the first few iterations. In the default version of the parametrizations, (a) mass from the second and third rings is rapidly pushed to the centre of the galaxy and builds up in the innermost rings while these rings become depleted because mass from outside was not transported fast enough to refill them. However, after integrating for longer times we see that mass gradually moves inwards and the mass in the second and third rings increases again. In the modified version (b) the transport of mass to the innermost ring is much more gradual, and we observe peaks of the profile which move inwards with time in a wave-like fashion. Interestingly, after the full 3 Gyr integration time the same steady state is obtained. The behaviour at the outer rings is identical since the modification to the parametrizations does not impact these outer radii. In the Appendix C, Fig. C.1 shows the same plot with only the 10 first iterations to stress that this early evolution deviates between the two versions.

We further expand this toy model by adding the increased resolution treatment that was discussed in the previous section. In Fig. 4.5 we show the outcome of the toy model with the same initial conditions when we have modified the inflow velocity profile at the inner radii and

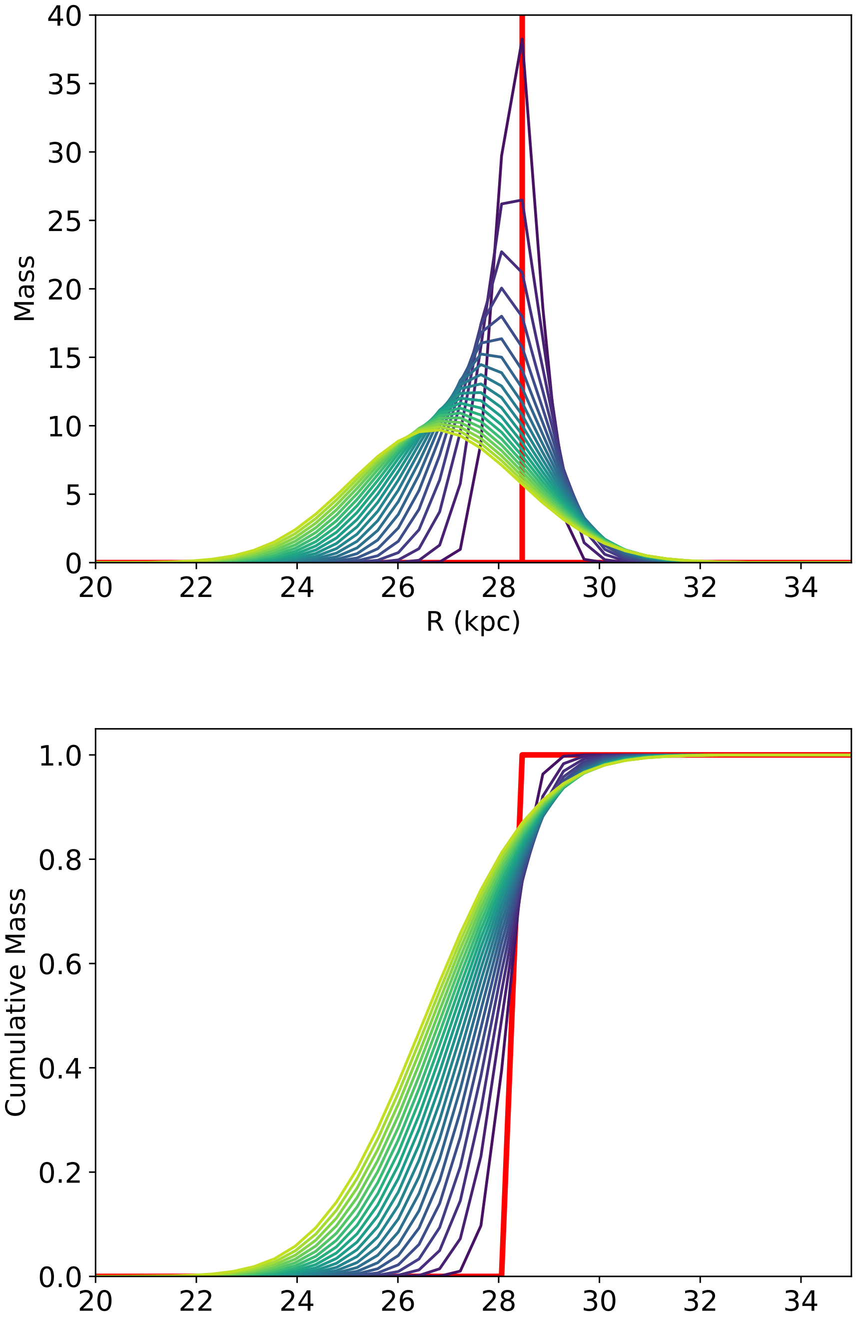

Figure 4.3: Diffusion of mass from a single ring to its neighbouring rings. On the top panel, we show the mass and on the bottom the cumulative mass. For this example we are using 100 rings linearly spaced between 0 and 40 kpc where only one ring centred at 28.5 kpc is populated with mass $M = 100$ at $t = 0$. We show 20 time iterations with lighter colors representing later times. We point to the Gaussian like distributions that are created with time and which become increasingly broader and shifted to smaller radii.

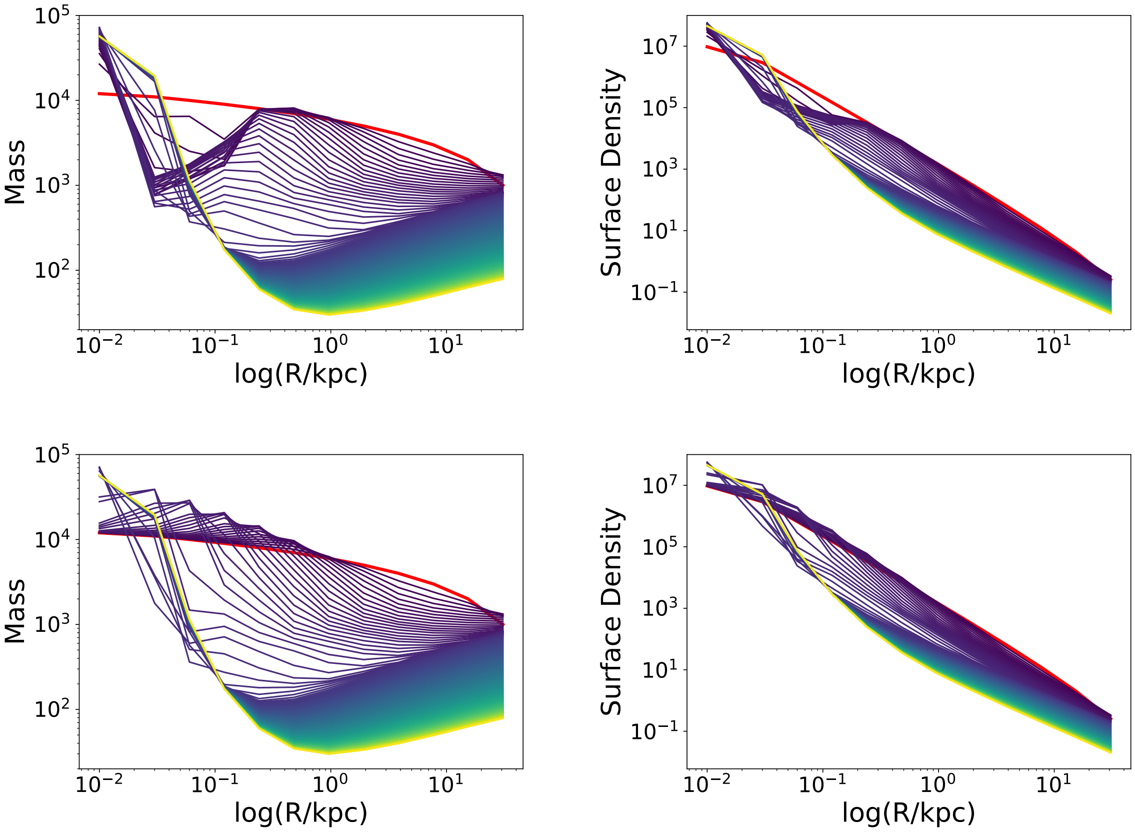

Figure 4.4: In this plot we show the redistribution of mass in a toy galaxy when applying our algorithm. We use the same structure as in L-Galaxies of 12 logarithmically spaced rings, initialized with an arbitrary mass profile which decreases monotonically with radius (red curve). We show in this plot 200 iterations with Δt = 15 Myr. The top panels show the cases where we extrapolate our recipe in the inner 1 kpc, whereas the bottom panels where we use the Fu et al. (2013) recipe for these regions. It is interesting to note that whereas the evolution appears different at the early times (purple hued curves) the same steady state is approached when integrating for 3 Gyr (yellow curve).

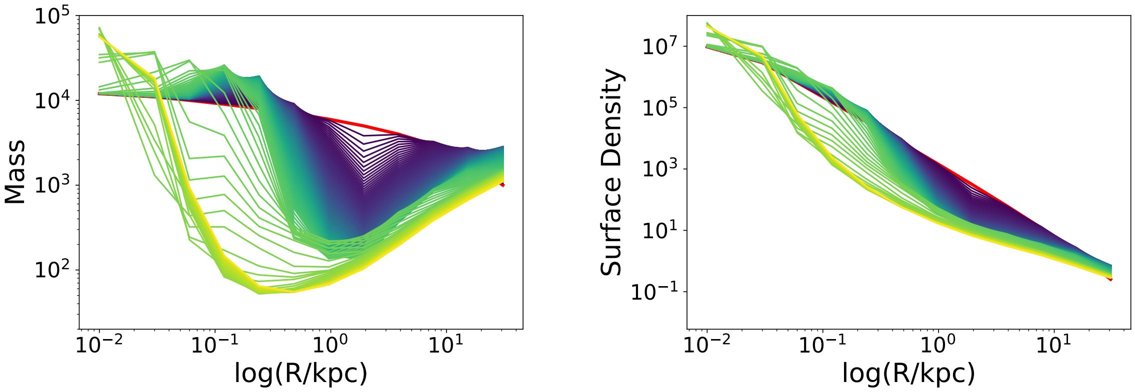

Figure 4.5: Similar plot to Fig. 4.4 with the same initial conditions and iterations but for the case where we have increased the resolution in the outer rings. The final steady state remains the same, however, the mass progresses slower towards the inner radii. There is also a build up of mass in the outer ring as expected due to the presence of a hard boundary at the outer radius.

adopting higher resolution in the outer rings. It is worthwhile to compare with the bottom panels of Fig. 4.4. We observe that the profile within 0.1 kpc is identical at the final time (yellow curve), despite the fact that the mass arrives at much later times in these radii. The outer rings are split into a series of smaller subrings, therefore mass transport becomes much more gradual through them as it is better tracked by the increased resolution. In this example we also note the build up of mass at the outer edge of the system which is not observed in the default ring resolution case. This can be explained in light of the slower rate of inwards mass transport. Mass remains for longer in the outermost ring, and because of the spreading parameter some part of it is moved to radii larger than the edge of the system. Since we do not allow mass to escape the system it is forced to concentrate in this outer boundary. This is a topic that needs potential improvement in our model.

It must be stressed that in all these examples there is neither the addition of new gas onto the rings nor the transformation of gas mass into stellar mass via the star formation process. Therefore it is expected that outer rings will be significantly depleted with time as mass flows inwards and at the same time gas mass will significantly build up in the centre of the galaxy. This toy model has no physical significance other than showing how the algorithm yields different results when modifying several parameters. However, in the full scale L-Galaxies model the differences that we find in how fast and to what extent mass builds up in given radii may significantly influence the outcome. For example, a very rapid concentration of gas at small radii and at early redshifts may trigger very high rates of star formation and subsequently an immediate depletion of gas in the inner regions that cannot be replenished in time, as well as induce larger amounts of stellar and AGN feedback which alter the cooling rates of these halos. This once again shows how each recipe is intertwined with the rest of the modelling in the L-Galaxies code, and highlights the necessity to re-calibrate the model after any modification to its structure.

4.4 Results from L-Galaxies

In this section we present results from a preliminary application of the new recipes in L-Galaxies. We choose to present a subset of results which are relevant to the topic of this thesis and highlight the differences between the model versions. In particular, we compare two versions of our implementation. In the first (orange color) we are using our parametrizations for the gas radial flow and stellar migration with the default radial ring structure and the modification to the velocity profile for the gas inflow at low radii that was mentioned before. The second run (green color) is using the exact same equations but we have employed the high resolution treatment for the outer rings, or in other words there is no change in the applied physics but only in the underlying structure on which the recipes are applied. In all cases we also compare with the result from the Henriques et al. (2020) model (blue color, referred to as Hen20). We do not run the model in the whole volume of the Millennium simulation but only in a selected merger tree file. This file has been specifically used for test runs of L-Galaxies because it has enough galaxies and produces a representative stellar mass function.

4.4.1 Mass Functions

In Fig. 4.6 we show the neutral hydrogen (HI) mass function at redshift $z = 0$ along with observational data (Jones et al., 2018; Haynes et al., 2011; Zwaan et al., 2005). Focusing on the masses above 10^9 $\mathrm{M}_{\odot}$ and comparing with the Hen20 curve we see that the low resolution version forms fewer gas rich objects whereas the opposite is true for the high resolution version. It is interesting that in the latter case the shape of the curve is very similar to the Hen20 model but shifted to the right, which indicates that a potential re-calibration of the model parameters could actually yield convergent results with two versions as well as with the observational data.

In Figures 4.7 and 4.8, we present gas (total and molecular), stellar and SFR mass functions at five different redshifts. The differences between the three curves in the stellar mass functions are minor in all cases showing that the stellar migration recipe is not as radical in changing global disc properties. Regarding the gas mass functions we find, as discussed for HI, that the high resolution version tracks the Hen20 model better, and we also see that any deviations arise at late times since for large redshifts there is extremely tight matching. In the low resolution version, we encounter the formation of a large number of galaxies with low gas (total and H_2) masses, a phenomenon starting at the largest redshift and persisting at all redshift values. In the future, we plan to use observational data to compare with these curves in detail, but doing so at this stage, before re-calibrating the model, is not conclusive.

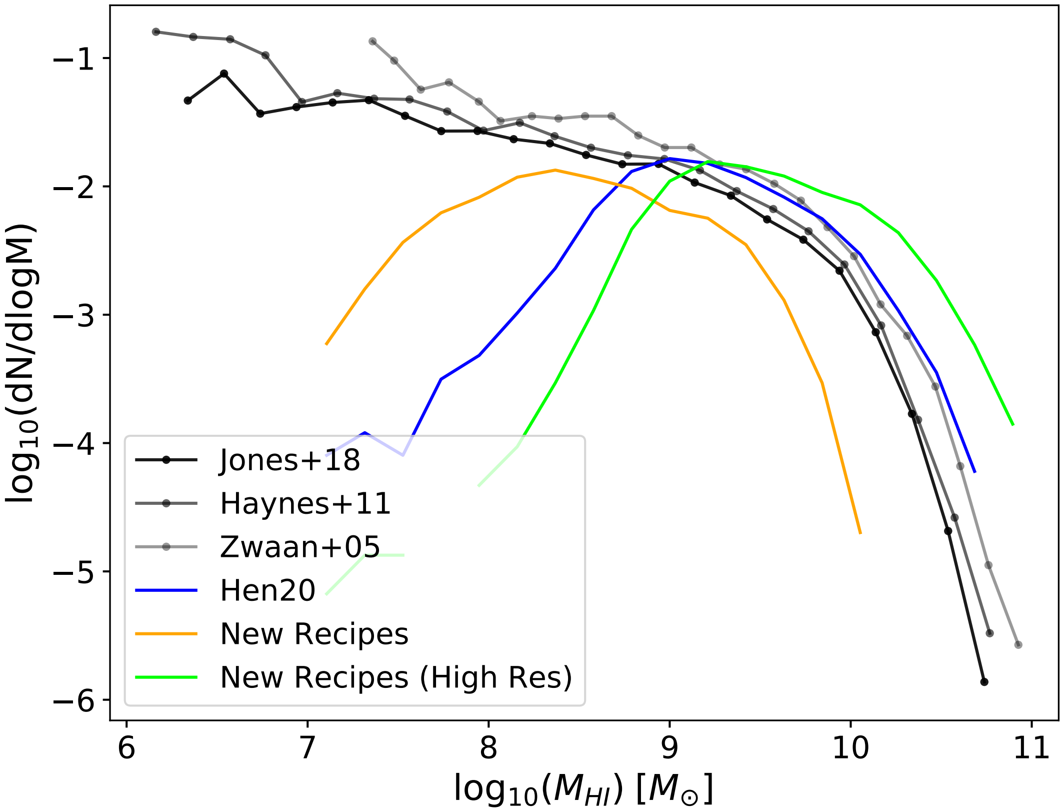

Figure 4.6: Neutral hydrogen mass functions by considering all the central galaxies in the single tree file. We plot the Henriques et al. (2020) result in blue and the outcome of our recipes in the default implementation (orange) and with increased resolution in the outer rings (green). We also show for comparison observational results from Jones et al. (2018); Haynes et al. (2011); Zwaan et al. (2005). It is expected that the Hen20 model matches the observations since it has been specifically calibrated to do so.

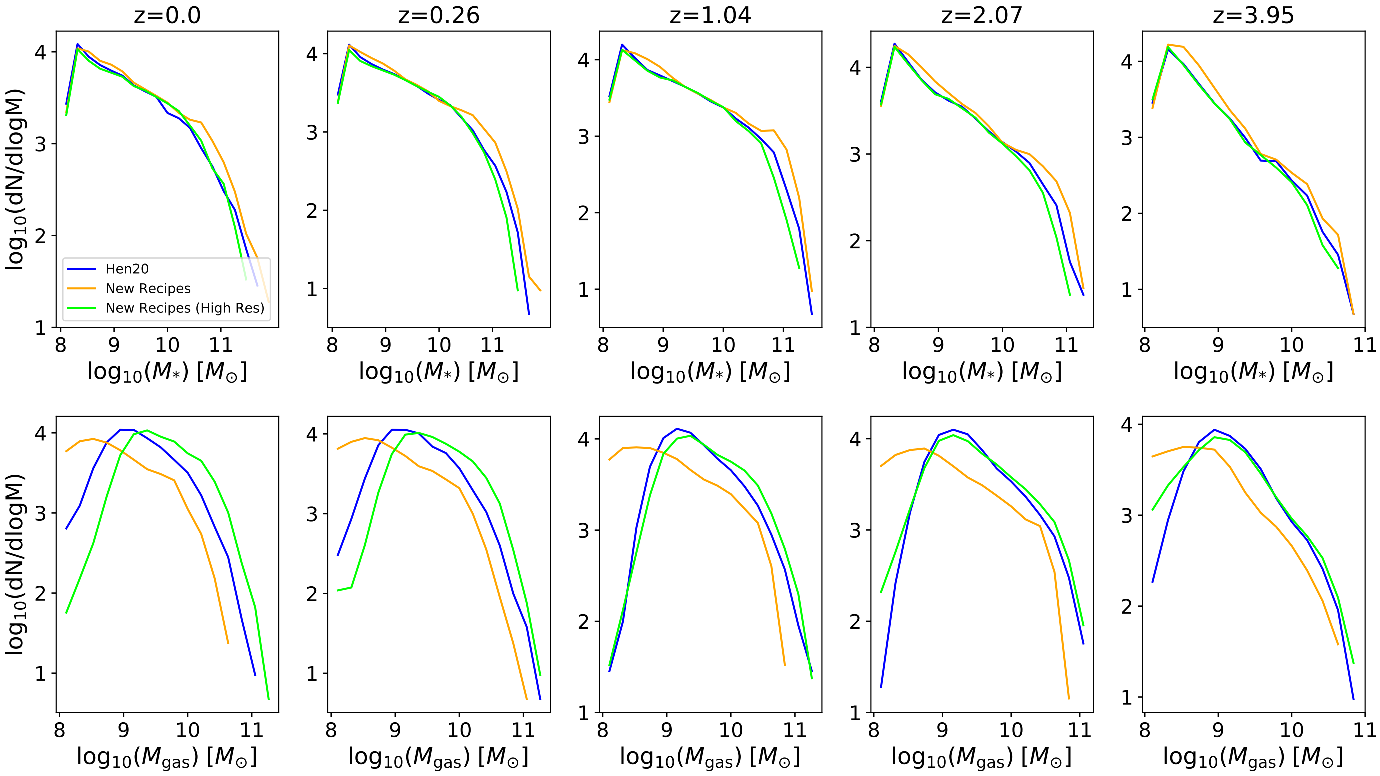

Figure 4.7: Mass functions for the stellar mass (top) and total gas mass (bottom) using all the central galaxies in the single tree file computed at five different redshifts. We plot the Henriques et al. (2020) result in blue and the outcome of our recipes in the default implementation (orange), and with increased resolution in the outer rings (green). We notice that the green curve shows better agreement with the Hen20 model over all redshifts.

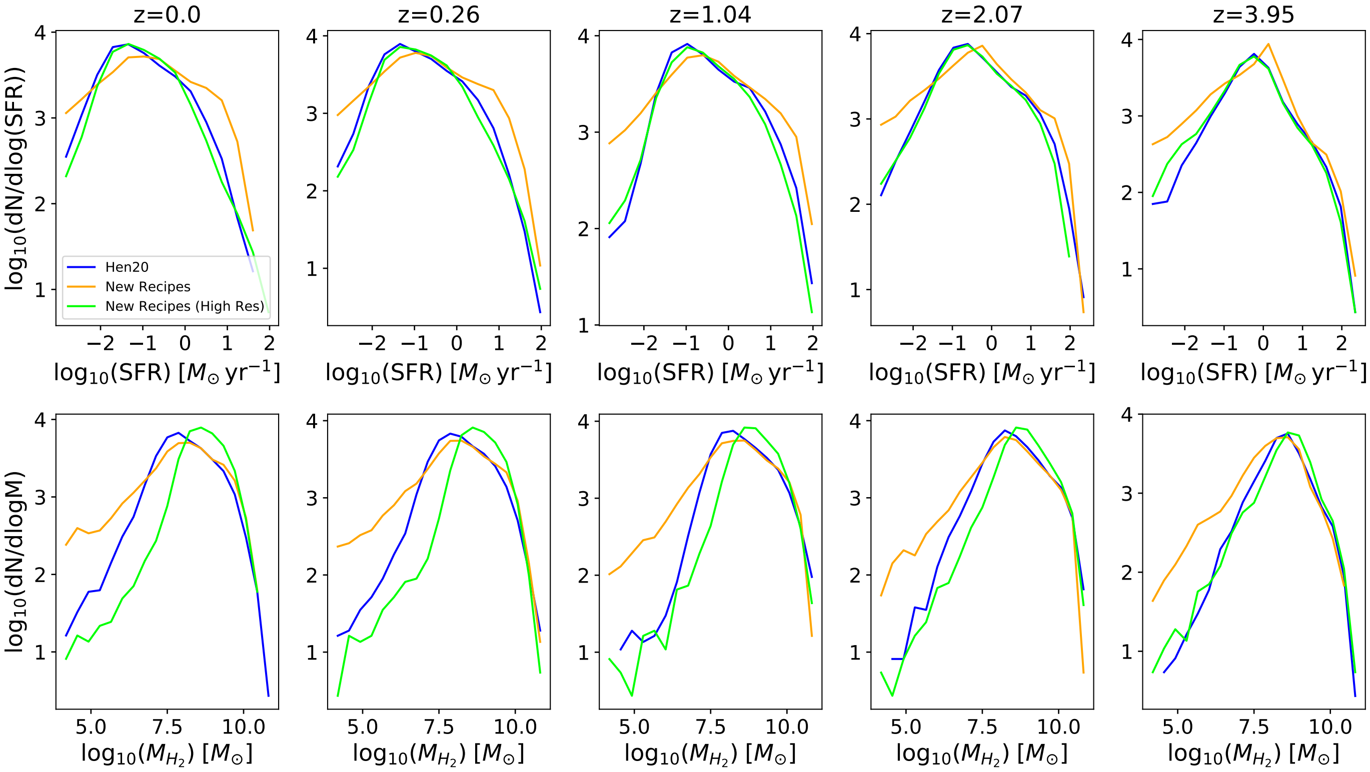

Figure 4.8: Star formation rate functions (top) and molecular gas mass functions (bottom) using all the central galaxies in the single tree file computed at five different redshifts. We plot the Henriques et al. (2020) result in blue and the outcome of our recipes in the default implementation (orange) and with increased resolution in the outer rings (green). We notice that the green curve shows better agreement with the Hen20 model over all redshifts.

4.4.2 Global relations

In the previous sub-section we have discussed how the change in ring resolution results in a substantially different outcome in the model's mass functions. We expand further on this topic by looking at relations between global properties of the galaxies.

In Fig. 4.9 we plot the total gas mass against the total stellar mass of all the galaxies that are produced in our runs at five redshift values. This figure confirms the findings of Fig. 4.7 in that from the earliest redshift there is an overproduction of galaxies with low gas mass in the low-resolution run while the range of stellar masses is similar for all models. Our explanation for this phenomenon is that gas is consumed by star formation very early in the evolution of the galaxies. Gas is funneled too rapidly towards the innermost rings where densities are high and star formation is efficient, while there is not enough time to be replenished by newly accreted gas onto the disc. We observe that the discrepancy between the low-resolution and the Hen20 models becomes smaller at lower redshifts as the systems approach a steady state. However, galaxy evolution is a sequential, causal process, thus the fact that many early galaxies are gas-depleted permeates into the subsequent evolution and cannot be completely washed out resulting in different outcomes by $z = 0$. On the other hand, the high-resolution run is consistent with the Hen20 model at high redshifts to a large degree, but at $z = 0$ we find an a excess of high-gas mass galaxies at large stellar masses and a deficit of low-gas mass galaxies at small stellar masses.

In Fig. 4.10 we plot the mean gas metallicity against the stellar mass at the same redshift values, where the gas metallicity is approximated by the ratio of the oxygen to hydrogen abundances. The low-resolution run produces an extreme range of metallicity values at early redshifts which is not agreeing with the predictions from the Hen20 and high-resolution models, while late redshift results are more divergent. A distinctive feature in the Hen20 contour plots is the dichotomy of low and high metallicity galaxy populations at low stellar masses. The high-resolution model is successful in reproducing this dichotomy although the locus is not as pronounced as in Hen20. Besides, the median curves for both Hen20 and the high-resolution run are in excellent agreement within the error bars for all the redshift values.

Fig. 4.11 shows the mean stellar metallicity plotted against the stellar mass. Much of the observations for the gas component also apply in this case, including the better agreement between the high resolution run and Hen20. At early redshifts the contour shapes in the low resolution model are comparable with Hen20 but the median is systematically higher. At later redshifts the low resolution model fails completely to reproduce the metallicity dichotomy at low stellar masses, whereas the high resolution model shows a more promising outcome.

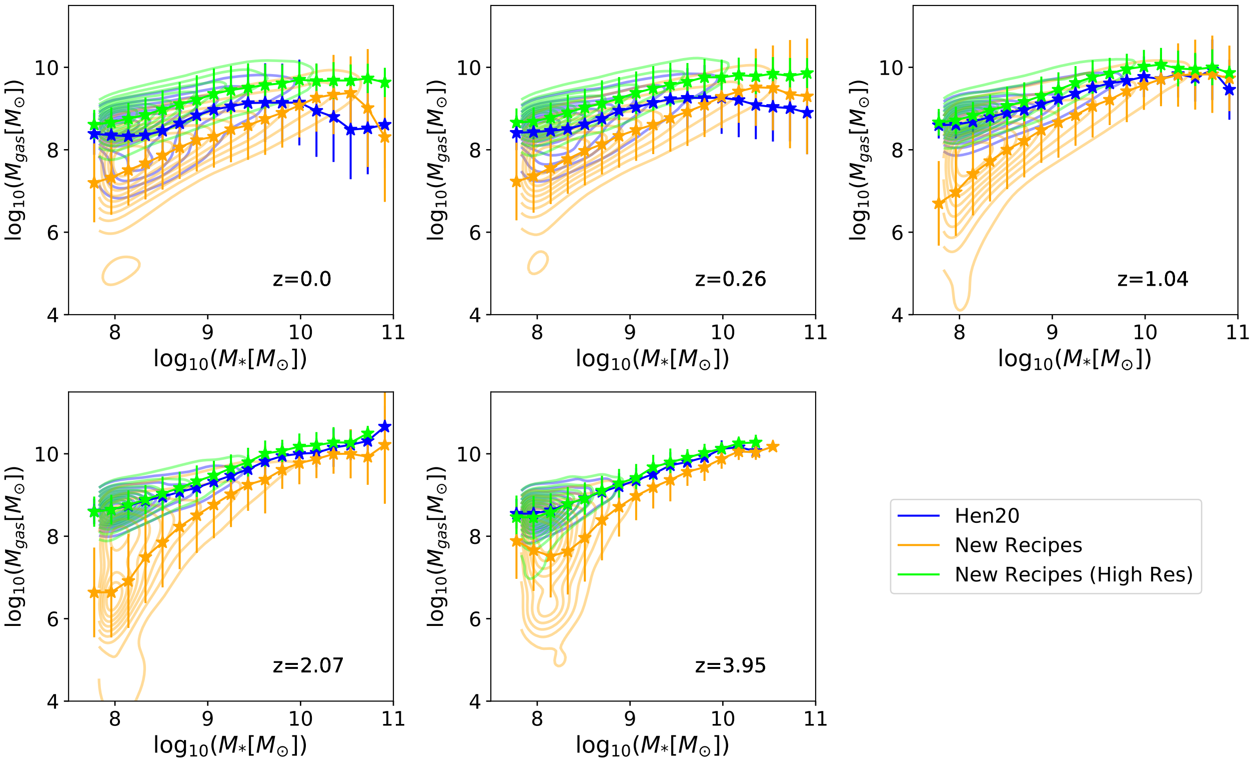

Figure 4.9: Total gas mass versus total stellar mass for all the central galaxies at five different redshifts. We plot the Henriques et al. (2020) result in blue and the outcome of our recipes in the default implementation (orange) and with increased resolution in the outer rings (green). We present the data points with the contour plots and also show the median curve with the 1 standard deviation error bars. The default implementation of the new recipes fails to match the gas-stellar mass relation in Hen20 starting from early redshifts. However, when we increase the resolution the results are in better agreement, although the Hen20 model is producing a higher number of low stellar mass-low gas mass galaxies at $z = 0$ which are not present in the high resolution run.

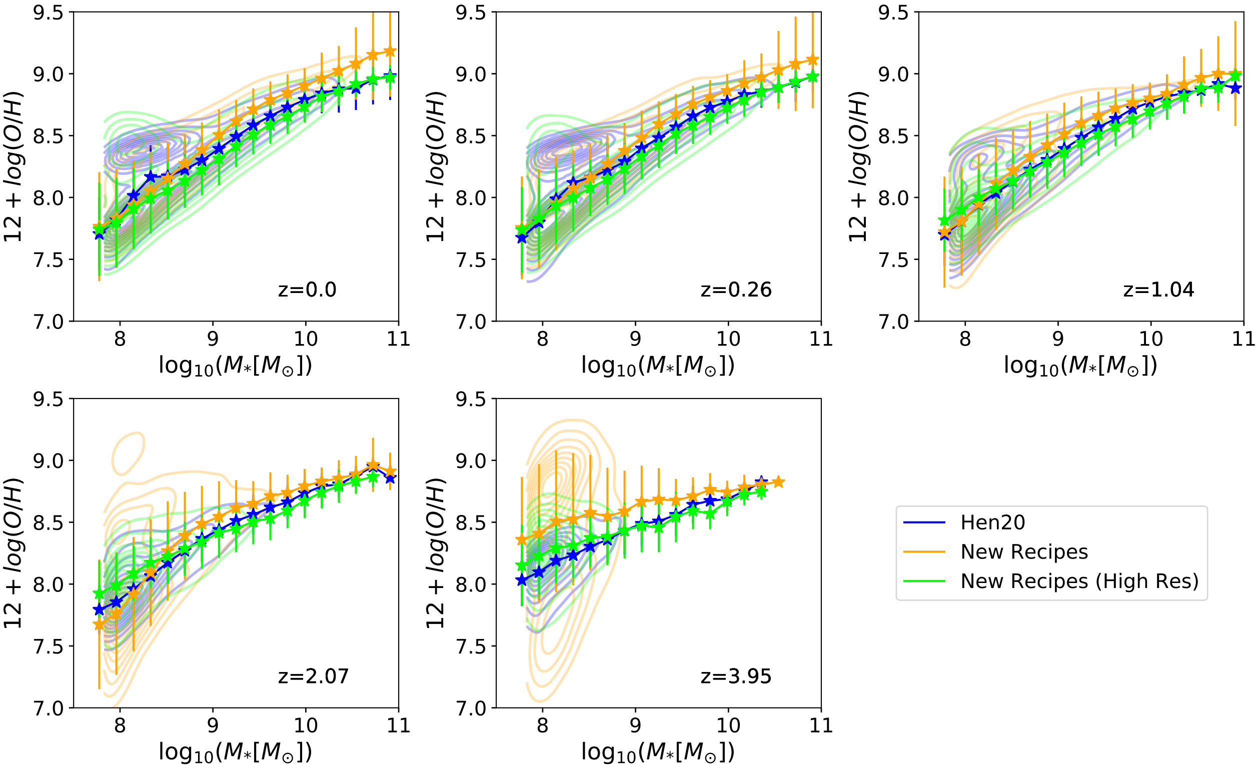

Figure 4.10: Similar to Fig. 4.9 but showing the global gas phase metallicity traced by the [O/H] ratio as a function of stellar mass. The default implementation (orange) again fails beginning at early redshifts but seems to match better the Hen20 model (blue) at later times. The increased resolution model (green) manages to reproduce to some extent the bimodality that is present in the contour plots of the Hen20 model.

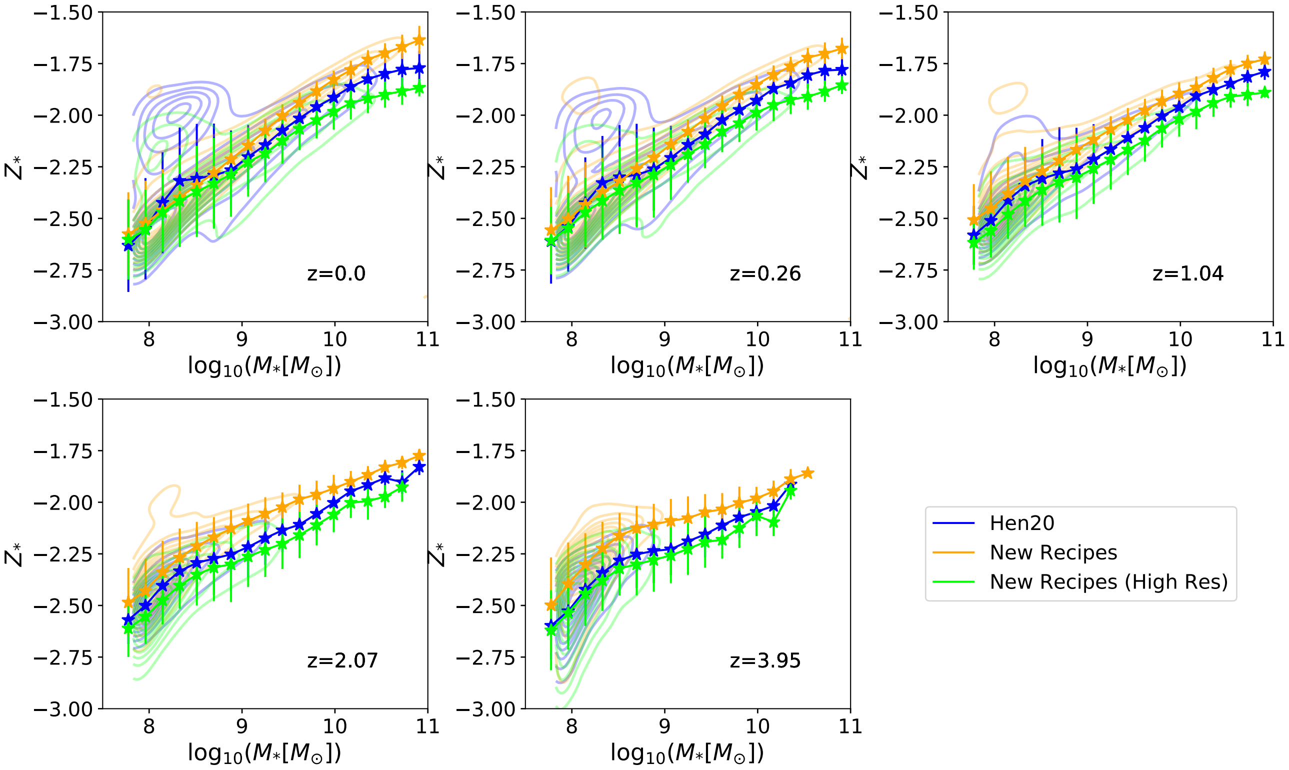

Figure 4.11: Similar to Fig. 4.10 but showing instead the global stellar metallicity in the galaxies against the stellar mass. In this case the default implementation (orange) is not extremely different to the Hen20 model (blue) although the stellar metallicity appears systematically higher. The increased resolution model (green) is closer to the Hen20 model but the locus of high metallicity-low mass galaxies at low redshifts is not as pronounced.

4.4.3 Radially resolved properties

We now turn our attention to radially resolved properties. We are only using the information for the stellar and gas mass in each ring in central galaxies (“Type 0”) in the model in order to compute mean radial profiles of the gas, stellar and star formation rate surface densities. These are shown, respectively, in Fig. 4.12 (gas), Fig. 4.13 (stars) and Fig. 4.14 (SFR) at redshift $z = 0$. We are splitting the galaxies into three mass bins, and we also add observational data from Leroy et al. (2008), for comparison. The observations are available mostly within 10 kpc hence the values from our model at the outer rings are not shown in these Figures. Despite some qualitative differences, all models fall within the range of the observations, rendering it difficult to extract a strong conclusion in favor of any of the versions. We notice that in the low resolution version, the gas (and by extension the star formation rate) appears much more concentrated in the innermost ring, resulting in steeper radial profiles, especially for the most massive bin.

In Figures 4.15 (gas), 4.16 (stars), and 4.17 (SFR) we show the radial profiles for the same three quantities for the whole range of the ring structure. We use the same mass bins and plot the results for five different redshift values. The main takeaway from all three plots is that the mean radial profiles predicted by the low resolution version are steeper than the Hen20 outcome in all mass bins and over all redshifts. On the other hand, the ones for the high resolution version are universally shallower than Hen20. This is in large part due to the larger concentration of mass in the outer ring which is the same observation that was discussed in the toy model above. We note that the mean radial profiles for all the individual elements that are tracked in L-Galaxies follow the shape of the gas surface density radial profiles.

We refrain from adding a more extensive discussion for these plots since this is ongoing work which is still subject to changes. Nevertheless, the differences that arise in the global disc properties when altering the ring resolution, primarily in the gas mass-stellar mass relation and secondarily in the mass functions, need careful exploration and a deeper understanding of how all physical processes interact during the evolution of the model galaxies. Moreover, the results in this section are obtained using the model parameters from Henriques et al. (2020) with readjustment. In this paper it is already shown that there are some best fit parameters that are significantly changed comparing to the previous model versions. As a future goal we would like to re-run the MCMC fitting process with our new recipes which may alter parameters in the model such as the star formation rate scaling or the supernova feedback strength significantly. Once there is enough confidence on the robustness of the new recipes the model can be run in the whole volume of Millennium as well as the high resolution Millennium-II. We also defer more rigorous comparisons with observations to future work when the new model has been fully established.

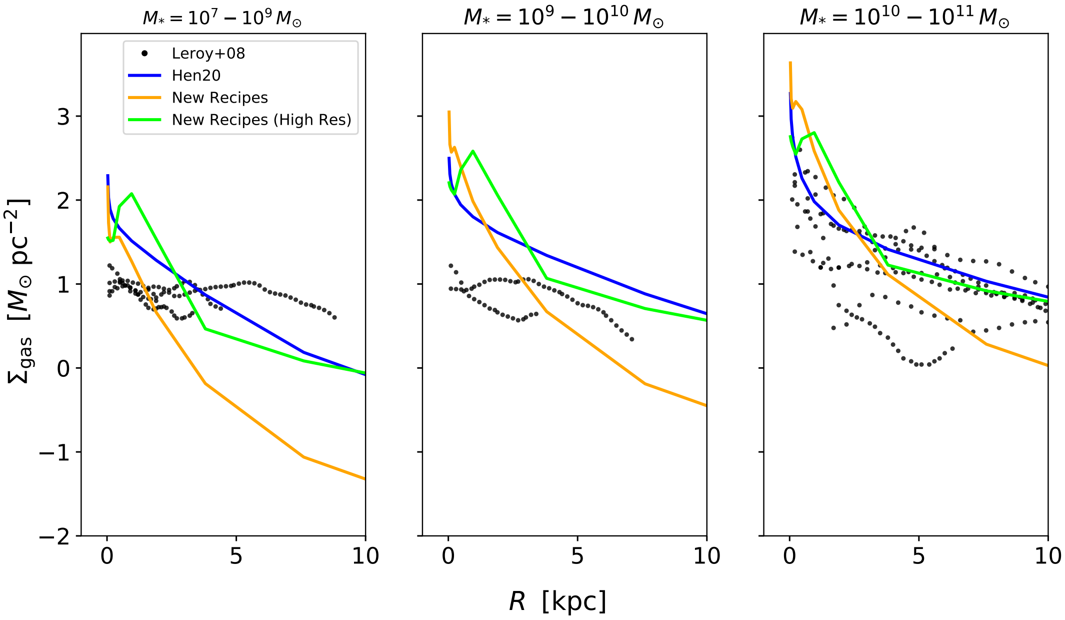

Figure 4.12: Mean gas surface density radial profiles for central galaxies at three different mass ranges. We plot the Henriques et al. (2020) result in blue and the outcome of our recipes in the default implementation (orange) and with increased resolution in the outer rings (green). We also plot observational data from Leroy et al. (2008) with the black points. However, it is not straightforward to decide which model matches the observations best.

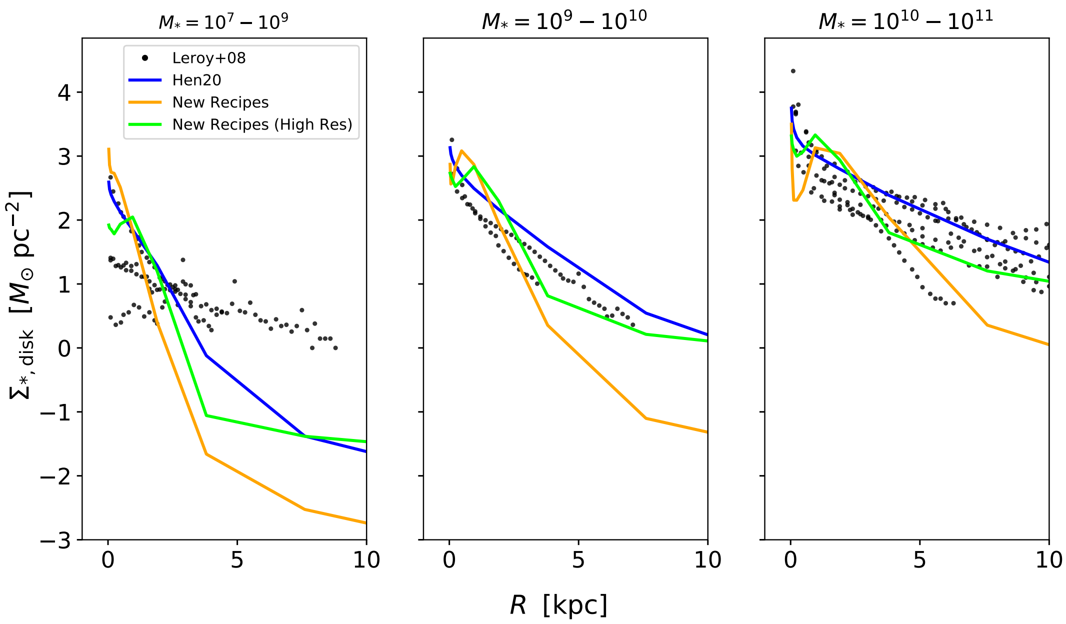

Figure 4.13: Similar to Fig. 4.12 but for the stellar surface density of the disc. The observational data are also drawn from Leroy et al. (2008). We arrive to the same conclusion that all three models seem to match the range of the observations.

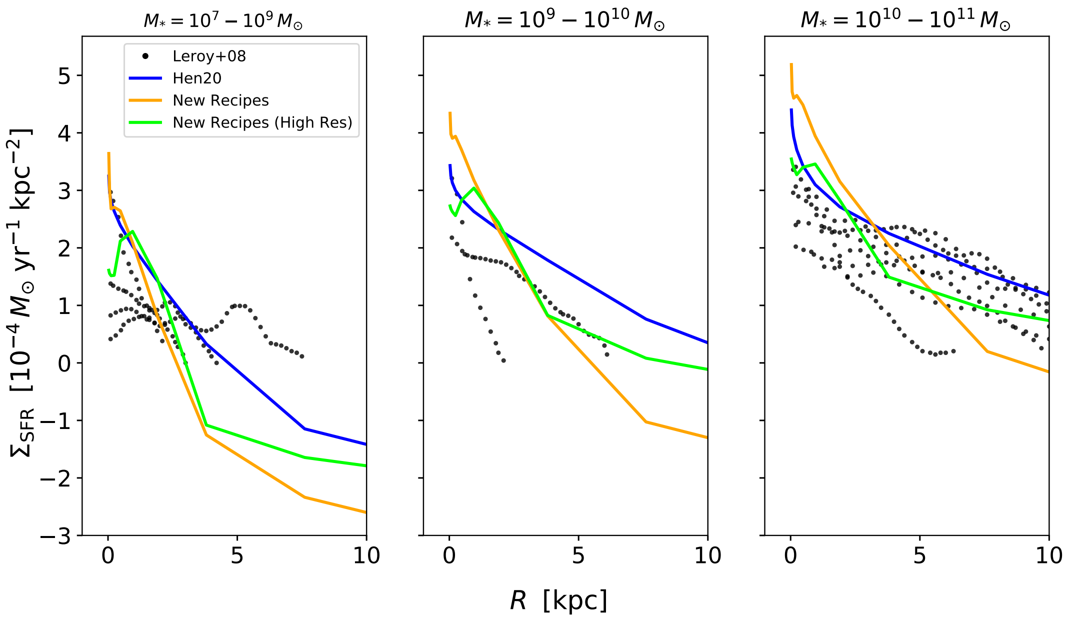

Figure 4.14: Similar to Fig. 4.12 but for the star formation rate surface density.

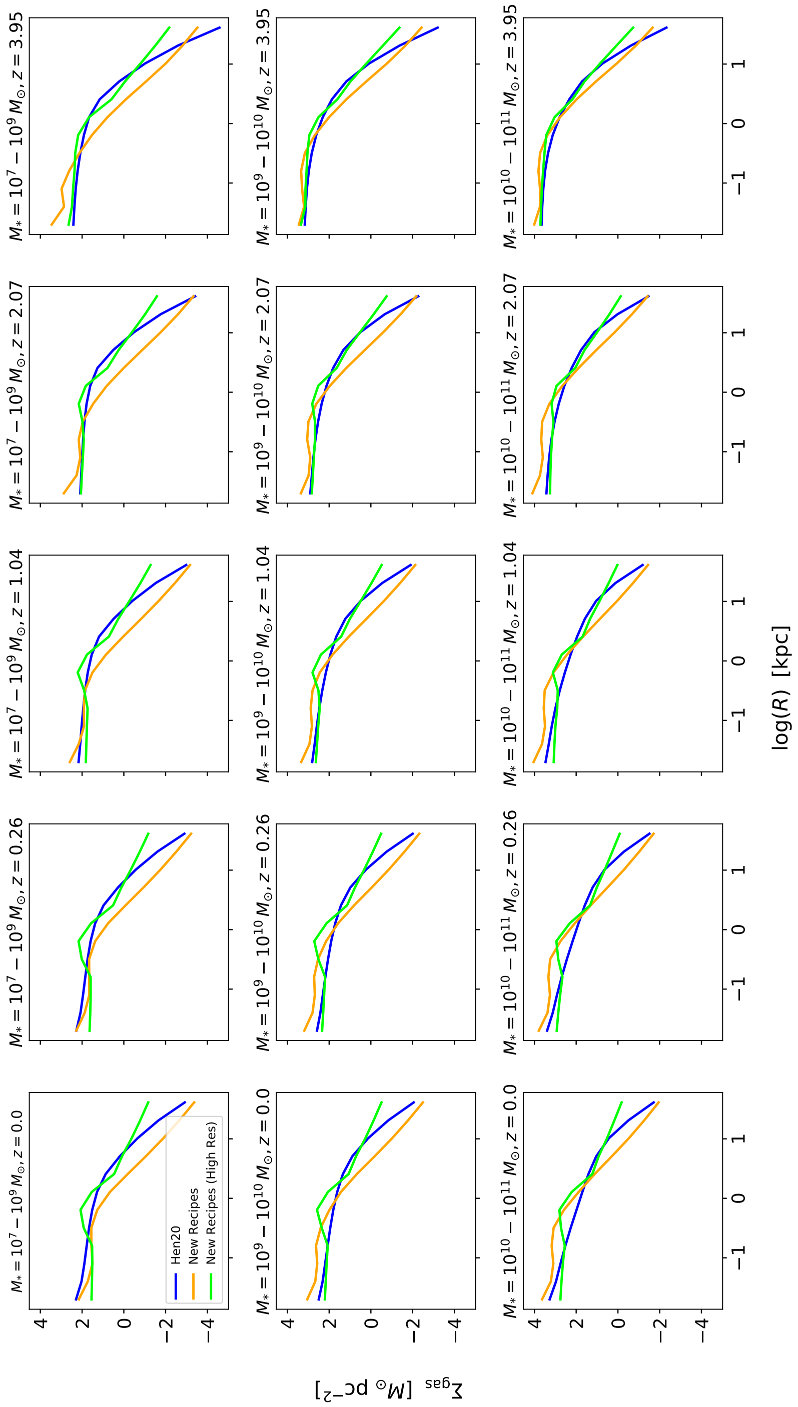

Figure 4.15: Mean gas surface density radial profiles for all the central galaxies at five different redshifts and three different mass ranges. The exact values are written on the top of each panel. We plot the Henriques et al. (2020) result in blue and the outcome of our recipes in the default implementation (orange) and with increased resolution in the outer rings (green). The default implementation tends to produce in general steeper radial gradients, while if we increase the resolution in the outer rings the gradients appear flatter than the Hen20 model.

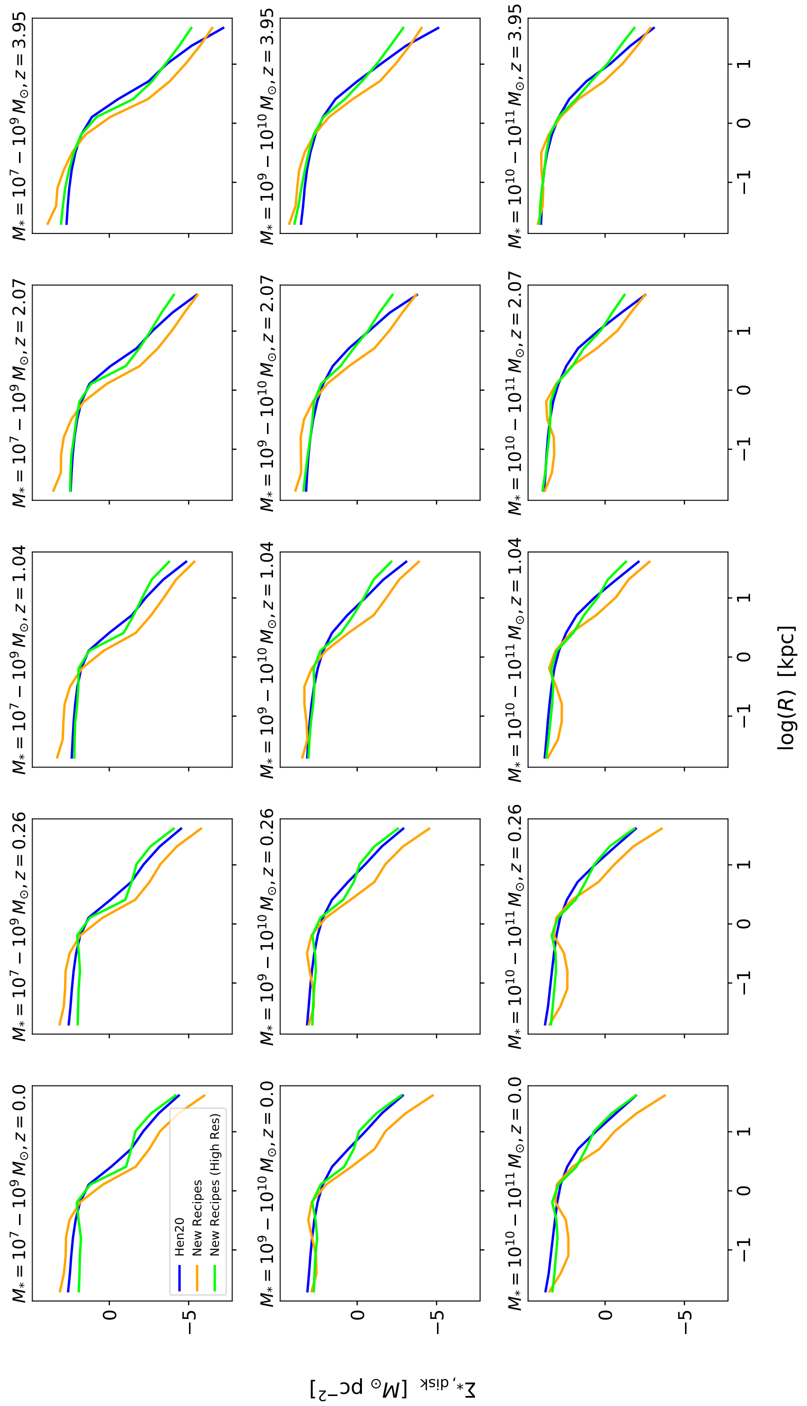

Figure 4.16: Similar to Fig. 4.15 but showing the mean radial profiles for the stellar surface density. The same conclusion that was discussed in terms of the steepness of the gas radial profiles applies for the stars. This is not surprising since the location of the gas determines the radii where star formation happens.

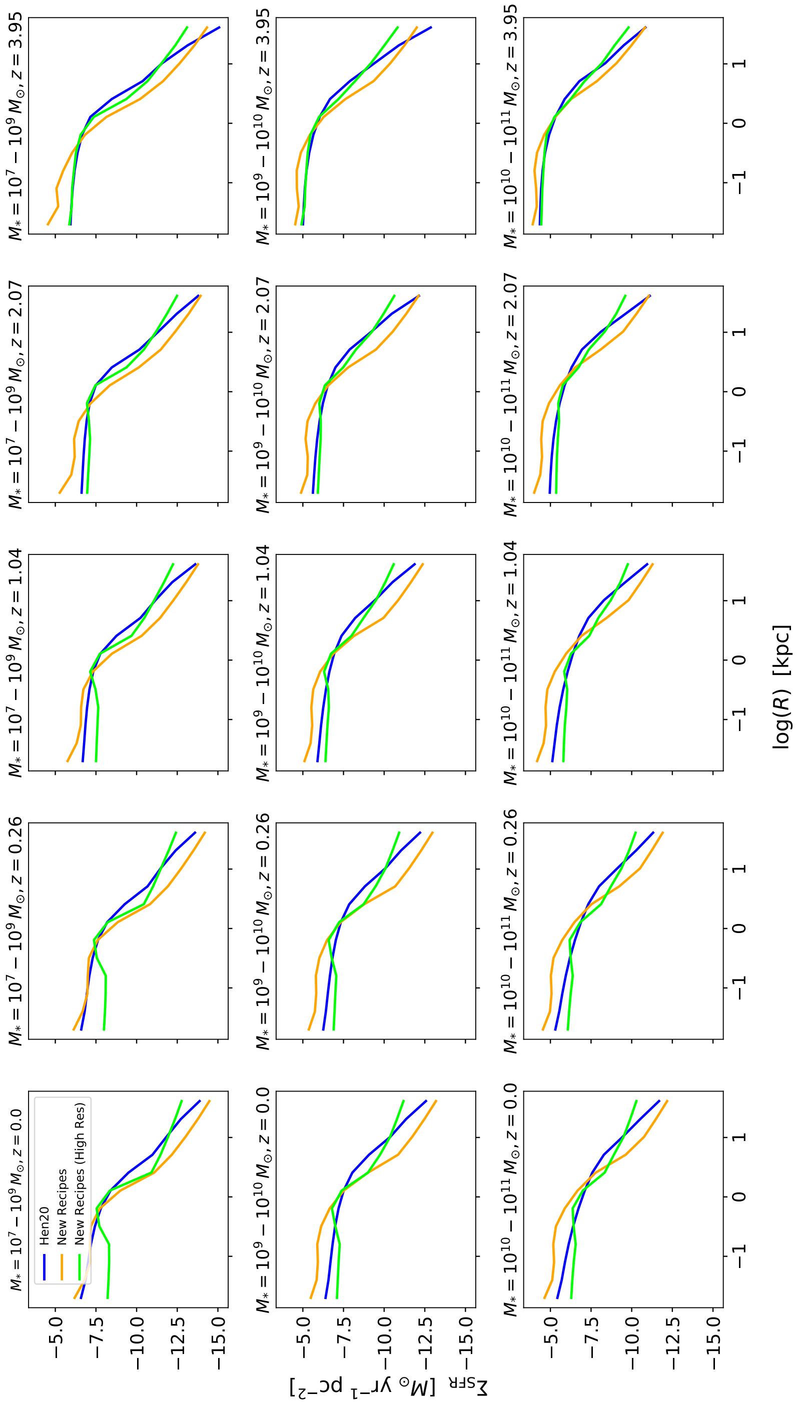

Figure 4.17: Similar to Fig. 4.15 but showing the mean radial profiles of the star formation rate density. The same conclusion that was discussed in terms of the steepness of the gas radial profiles applies for the star formation rate which is a reasonable consequence since the star formation rate is proportional to the gas surface density.

Chapter 5

Summary and future outlook

In the final chapter of this thesis we restate and summarize the main results from the previous three chapters while exploring their importance in the field of disc galaxy evolution. We conclude the thesis by suggesting possible new directions of research that can follow from this work.

Study of radial transport processes in Auriga

Gas component

In Chapter 2, we studied the radial gas flows in a sample of Milky Way-like disc galaxies from the Auriga simulation suite. The choice of this simulation for our analysis was made due to the fact that Auriga is specifically designed to simulate realistic disc galaxies in relatively isolated environments with very high resolution. These are ideal conditions to study the secular processes of galaxy evolution. Furthermore, Auriga includes a comprehensive galaxy formation model and has been produced using the state-of-the-art moving mesh code AREPO which combines the advantages of both grid-based codes and SPH codes.

In order to track the flow of gas between different cells and by extension different radii within the plane of the galaxies we have used tracer particles that are exchanged between different cells, following the flow of material. We applied a ring decomposition of the discs and measured the amount of radial displacement of the tracers within each ring between pairs of snapshots. We quantified the strength of the radial flow at each ring/radius with two parameters, a bulk flow velocity $\Delta\mu$ which indicates how much the median position of the selected tracers have changed and a radial spread w which shows the radial dispersion of the tracers around the new median. We list below our main conclusions for the mean properties of these quantities over all our galaxies.

- The spread w increases with the timestep Δt in a $w \propto \Delta t^{1/3}$ fashion which is slower than true diffusion which would have an exponent with value 0.5.
- The spread w increases almost linearly with radius from the centre of the disc, that is the tracers diffuse more strongly in the outer regions.
- The bulk flow velocity $\Delta\mu$ has a flat radial profile for radii at the inner part of the disc (between 10-70% of the disc radius) with a median value of $-2.4\,\mathrm{km\,s^{-1}}$, while beyond

70% of the disc radius the inflow velocities increase linearly with radius reaching values of tens of km s^{-1}. Hence, we conclude that there are two different regimes, an equilibrium region for the inner part of the discs and an accretion dominated region at the outer parts of the discs which drives larger flows.

- The analysis of the residuals around the median curves shows that larger values of w are obtained in rings with higher velocity dispersion and higher accretion rate of new gas. This can be connected to having larger turbulence and therefore more energy dissipation. On the other hand, there is no strong correlation with the surface density of the ring or its star formation rate.
- $\Delta\mu$ correlates very strongly with the change of the specific angular momentum of the tracers, confirming that the inwards bulk flow is connected to the loss of angular momentum of the gas. From the residual analysis we also find that there are increased inward flows in rings where there is a higher accretion rate of new gas.
- We find no redshift dependence of the strength of the radial flows for the time period of 6 Gyr that we study.
- Finally, we are presenting parametric equations for w and $\Delta\mu$ that describe their radial dependence as well as their dependence on the secondary properties, the radial velocity dispersion σ_r and the accreted mass fraction $\dot{f}_{acc}$. These parametrizations can be cast into theoretical models of galaxy evolution.

Stellar component

In Chapter 3, we worked with the same sample of Auriga galaxies, focusing on the stellar component. We have asked how the galactocentric radii and guiding centres of stellar orbits change from the birth radii of stars and also between different snapshots. Furthermore, we have investigated the effect of the stellar migration process on the metallicity and age profiles of the discs, and we have provided a quantification of the strength of migration in different types of systems. We have applied a similar radial decomposition, as in the gas analysis, and within each ring, we have measured the change in the median galactocentric radii, $\overline{\Delta R}$, of stars and the spread w around the median for different pair of snapshots. However, for the stellar component we have tracked additionally the corresponding changes in the guiding centres of the stellar orbits, $\overline{\Delta R_g}$ and w_g. The findings from this chapter can be summarized as follows:

- We have quantified the migration strength $\sigma_{\rm migr}$ during the lifetime of the stars in individual systems as well as in the average of our sample. We find that at redshift $z = 0$ young stars ($\sim$ 2 Gyr) have migrated on average 1-2 kpc whereas older stars ($\sim$ 10 Gyr) moved between 2-4 kpc. This age dependence agrees with the theoretical modeling by Frankel et al. (2020). Furthermore we find that stars that have been born at larger radii have experienced, on average, stronger migration, meaning that they were most affected by torques in the disc.
- The effects of stellar migration on the total metallicity profiles are minute, and this is also the case when we look only into the young (< 3 Gyr) stars in the disc. However, we find that if we isolate the older stellar populations (9-12 Gyr) there is a considerable flattening of the

radial metallicity profiles for most systems. This is explained on the basis that older stars were subject to changes in their orbital characteristics for longer time, enough to imprint the effect of stellar migration.

- Upon further exploring the flattening of metallicity profiles we have found correlations of the change in the outer slope $\Delta\alpha$ with the strength of the non-axisymmetries in the disc (i.e. presence or absence of a bar) as well as the stellar mass of the systems.
- By measuring the timestep dependence of w and w_g we have explored whether the stellar migration can be treated as a diffusion process. For the galactocentric radii, w, we find a very weak dependence on the snapshot spacing, Δt, which does not follow a diffusion evolution. On the other hand, changes in the guiding centres resemble to a good degree a diffusion process (i.e. $w_g \sim \Delta t^{0.5}$) in many of our systems, but only if we consider stars that are located at outermost radii of the discs, while for inner radii the exponent decreases and becomes sub-diffusive.
- We find that galaxies in our sample that develop a stronger bar are linked with enhanced stellar migration, i.e. stars on average experience larger changes in their guiding centres. This statement is further supported by the fact that for barred galaxies we measure shallower slopes in the metallicity profiles for older stellar populations. The physical explanation is that the bar is exerting strong torques onto the orbits of the stars, altering their angular momentum and causing them to migrate inwards or outwards. Consequently, metallicity gradients are washed out by the mixing of populations with different metallicities that have been born at different radii in the disc.
- Finally, we parametrize the migration strength via the quantities w and w_g as a function of radius R and time Δt. In particular our best fit equations suggest a power law dependence with regards to both R and Δt. We find that for the same time period and at the same radius, w obtains larger values than w_g, however, w_g has a stronger dependence on R and Δt.

Study of radial transport processes in L-Galaxies

In Chapter 4, we described the introduction of two new physical prescriptions in the L-Galaxies semi-analytic model. We have updated the existing recipe of radial flows in the model while also adding a new prescription that allows stars to be exchanged between different radii in an attempt to simulate the stellar migration process. The core difference between our gas flow recipe and the current L-Galaxies version is that we apply a spreading of the gas on top of the median bulk flow. This means that at any given radius there are fractions of the total mass that move both to inner and outer rings. The contents of Ch. 4 are part of ongoing work and further tests are required to extract robust, meaningful conclusions. However, we summarize here some preliminary observations and results that are already available from our new implementation.

- We redistribute the gas between different rings in the model using a Gaussian probability distribution function the width of which is derived by our parametrizations from the previous two chapters. We employ an algorithmic design to decide what fraction of mass from a given ring ends in all of the other rings, while ensuring mass conservation.

- There is a need for adjustments to the parametrizations that were derived from Auriga in order to incorporate them in a different model. In particular we are scaling the spreading parameter w by the width of the rings in L-Galaxies and we do not interpolate our equation for the gas bulk flow velocity, $\Delta\mu$, in the inner rings but rather force it to approach zero as $R \rightarrow 0$.
- We find an intriguing dependence of the output of the model to the resolution of the ring structure. In particular the results of our version agree better with the Henriques et al. (2020) model if we increase the number of rings in the outer radii of the discs. Besides in the default lower resolution version our parametrizations do not yield reasonable gas mass – stellar mass, and metallicity – stellar mass relations.
- The mean radial profiles predicted by different versions of our model are all within the range of observational data. Therefore, arriving at a definite conclusion as to which model version is better in reproducing these observations is not trivial.

Future prospects

In this work we presented for the first time a qualitative and quantitative description for the radial gas flows and stellar migration as obtained from the analysis of a relatively large number of simulated disc galaxies, compared to earlier works were either such a quantitative description was lacking or the study was limited to a very small number of galaxies. Moreover, we were able to pinpoint the physical characteristics of the discs that are contributing in the redistribution of material within the galactic plane. The parametrizations that we derived can have useful applications in theoretical modelling of galaxy evolution, both in semi-analytic and chemodynamical models. Since they are directly describing the behaviour that is observed in a reliable high resolution hydrodynamic simulation they are complimentary to purely theoretically derived recipes.

Within this thesis we already presented such a preliminary application into the L-Galaxies semi-analytic model. In future work, we aim to extend the work that was presented in Ch. 4 by conducting more tests for the behaviour of our new models in L-Galaxies and in particular checking the limits of their application in galaxies of different masses. Ultimately we aim to run the updated version of the model in the whole volume of the Millennium and Millennium-II simulations, allowing us to create catalogues of the properties of a vast number of galaxies with higher physical fidelity, and make to statistically significant statements for the whole galaxy population.

A further path of great interest would be to repeat the same analysis that we did for Auriga in a different set of simulations. This could include either a) other zoom-in cosmological simulations with a different treatment of several physical mechanisms and in particular a different treatment of the physics of the interstellar medium, b) simulations of isolated discs where there is no effect from the surrounding cosmological environment, or c) large-scale hydrodynamical simulations, such as Illustris-TNG, which despite the lower resolution in the disc, can offer a much larger statistical sample and many different galaxy types.

Appendix A

Fig. A.1 shows a case where the radial distribution of the tracers at snapshot $n + 1$ is highly asymmetric, and a Gaussian fit is not accurately describing the shape of it. There is a considerable difference in the value of the 16-84 percentile range and the width of the Gaussian fit. Such histograms appear mostly at outer regions of the discs and are probably pointing to material in the accretion phase. In Fig. A.2 we see that for the total sample of the rings the calculation of the width of the distribution described by the 16-84 percentile range and the σ of the Gaussian fit is on average consistent. There are outlier points mostly in the lower right part of the plot which indicates that for these rings the Gaussian fit underestimates the width comparing to the percentile range calculation (as shown in Fig. A.1). In Fig. A.3 we examine the resolution convergence by calculating the median profiles for w and $\Delta\mu$ for a single halo from the simulation suite simulated with the fiducial and lower resolution.

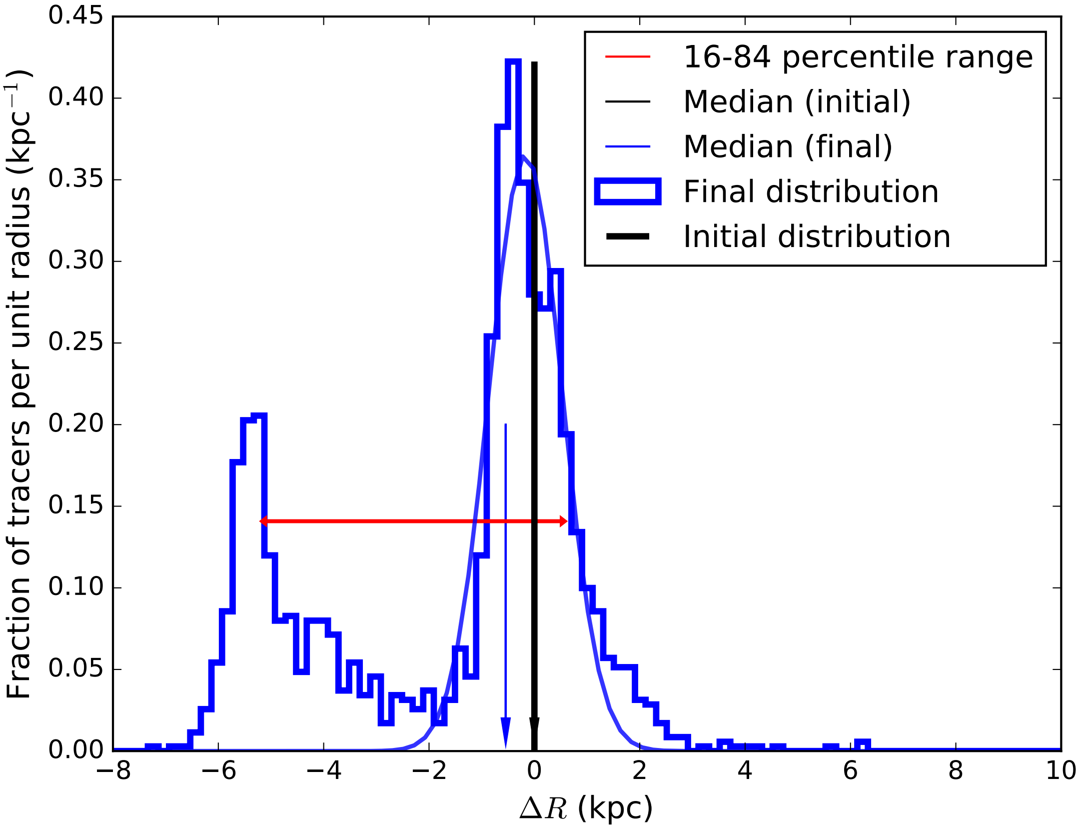

Figure A.1: Asymmetric histogram example where a Gaussian is not well fit.

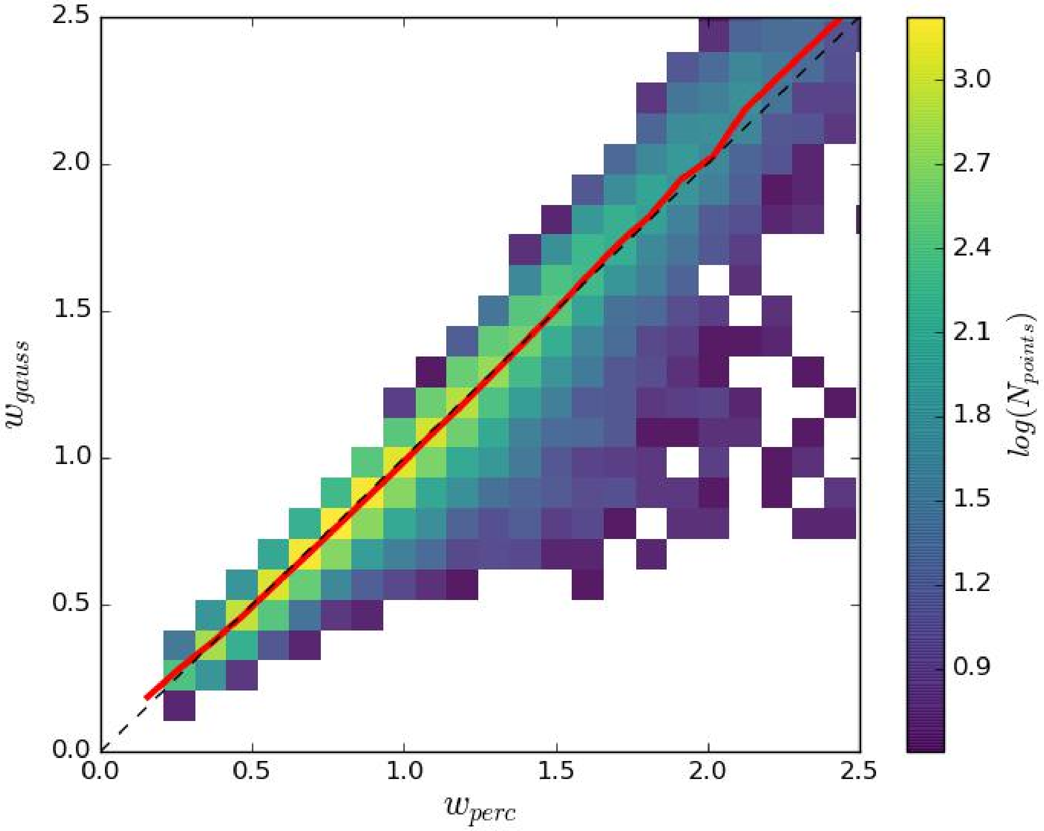

Figure A.2: Comparison of the Gaussian width (y-axis) and the 16-84 percentile range values (x-axis). We observe that there is very close 1-1 correspondence of the two measurements, and they can mostly be used interchangeably.

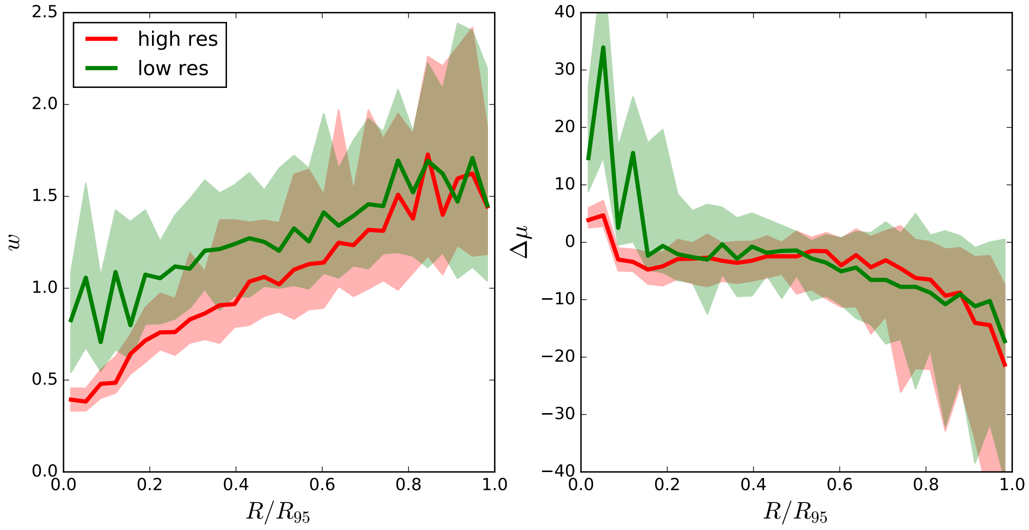

Figure A.3: Comparison of the mean radial profiles of the quantities w and Δ_{mu} when using a lower resolution simulation. This graph is made only for one halo of the set that was available in a low resolution run. The deviation from the fiducial resolution is more evident in the inner regions where tracers appear to be more diffusive.

Appendix B

In Fig. B.1 we plot the migration strength σ_{migr} versus the age of the stars at $z = 0$. We use four radial bins, each shown in the four panels and we also split the stars based on their age at $z = 0$ in four further bins. In this figure, each datapoint is drawn from a separate halo and represents the width of histograms, such as those presented in 3.6. The same information is conveyed in Fig. 3.7 in a more concise presentation, showing the scatter of the data points with error bars around the median curves.

In Fig. B.2 we give examples of how the histograms in ΔR look like. From such histograms we extract the median ($\overline{\Delta r}$) and the width (w) which we use to describe stellar migration for the stars in the given ring. Histograms in terms of ΔR_g look very similar.

In Fig. B.3 we show the time interval dependence of the quantity w_g, similar to Fig. 3.14, for each individual galaxy in three different radial bins. We notice that in some disks, in the two outermost rings the value of the slope is near or around the diffusion value of 0.5.

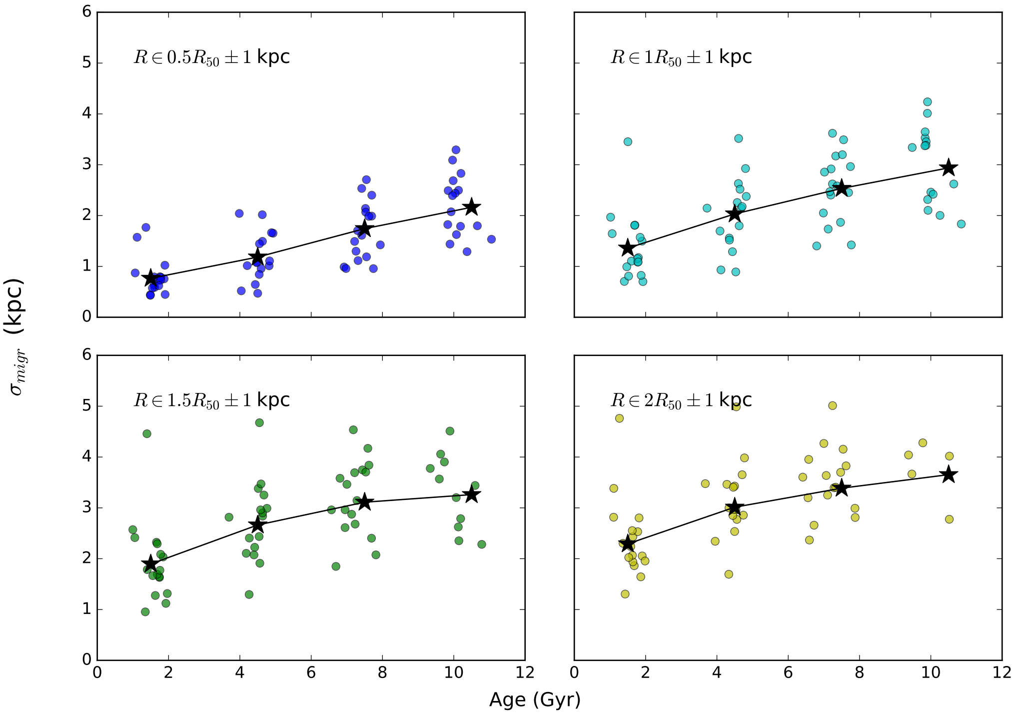

Figure B.1: The information used in Fig. 3.7 presented in separate panels, showing the data points that are used to calculate the median curves and the errors.

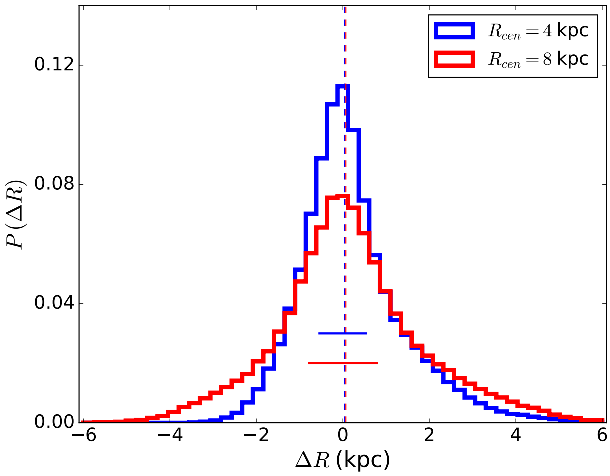

Figure B.2: Example distributions of the change of the galactocentric radii for the stars selected at two given rings centred at 4 (blue) and 8 (red) kpc for ‘halo_6’. From these histograms we compute the median shift ($\overline{\Delta r}$) shown with the dashed line, and the 16-84 percentile range (w) shown by the horizontal lines. We observe that for the outer ring the distribution is more broadened. In both rings the shift of the median from zero is very small, and in these particular examples is slightly positive.

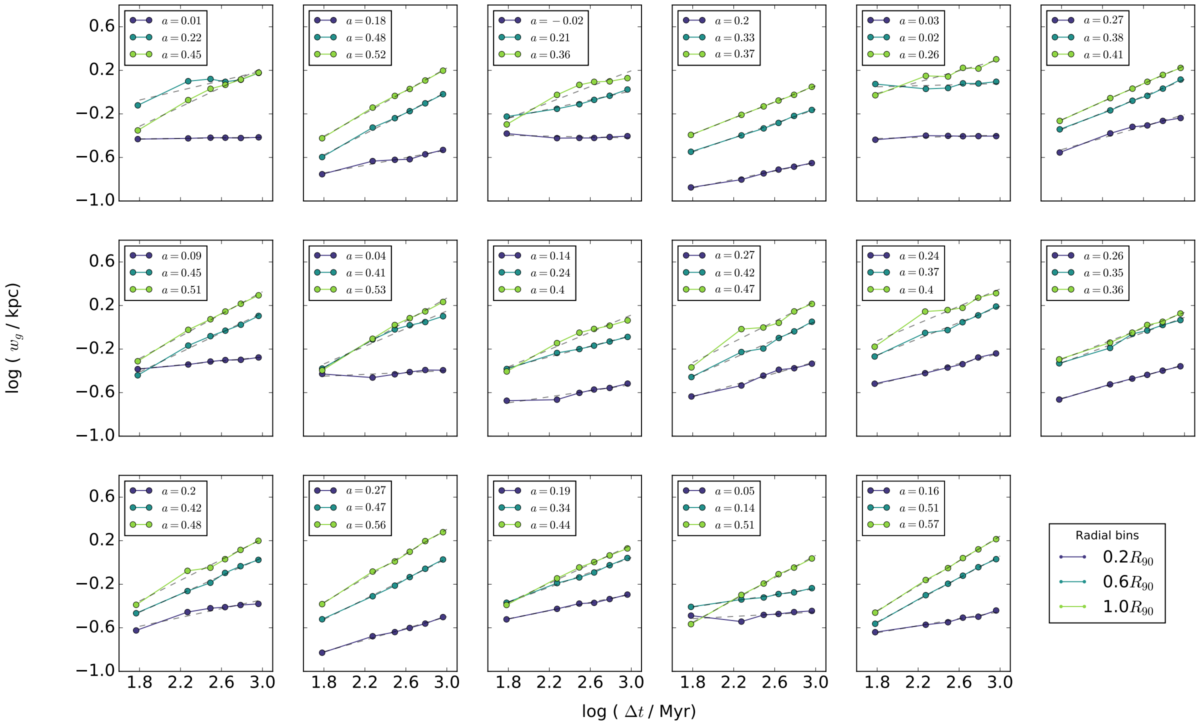

Figure B.3: Logarithmic plots of the spread w_g against the time interval Δt for individual halos. The different curves are for different normalised radii within the disks. The slope of the best fit line is quoted in the legend in each panel. We find a variety of different values for the slopes, ranging between 0.3-0.6 in most galaxies for the two outermost rings (cyan and green).

Appendix C

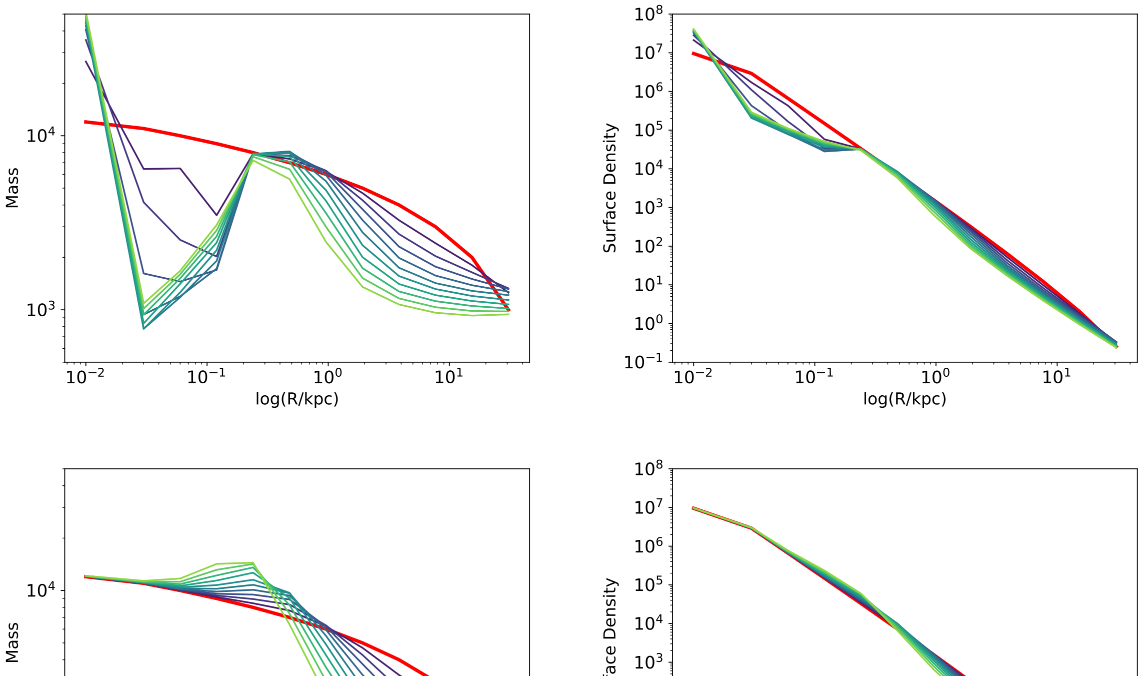

Figure C.1: Same as Fig. 4.4 but plotting only the first 10 iterations to stress the early times response.

Bibliography

Agertz O., Kravtsov A. V., Leitner S. N., Gnedin N. Y., 2013, ApJ, 770, 25

Agertz O., et al., 2021, MNRAS, 503, 5826

Anders F., et al., 2014, A&A, 564, A115

Asplund M., Grevesse N., Sauval A. J., Scott P., 2009, ARA&A, 47, 481

Athanassoula E., 2013, in Falcón-Barroso J., Knapen J. H., eds, , Secular Evolution of Galaxies. p. 305

Aumer M., White S. D. M., Naab T., Scannapieco C., 2013, MNRAS, 434, 3142

Aumer M., Binney J., Schönrich R., 2016, MNRAS, 459, 3326

Ayromlou M., Kauffmann G., Yates R. M., Nelson D., White S. D. M., 2021, MNRAS, 505, 492

Baba J., Saitoh T. R., Wada K., 2013, ApJ, 763, 46

Bakos J., Trujillo I., Pohlen M., 2008, ApJ, 683, L103

Bergemann M., et al., 2014, A&A, 565, A89

Bigiel F., Blitz L., 2012, ApJ, 756, 183

Bilitewski T., Schönrich R., 2012, MNRAS, 426, 2266

Binney J., Tremaine S., 2008, Galactic Dynamics: Second Edition

Boylan-Kolchin M., Springel V., White S. D. M., Jenkins A., Lemson G., 2009, MNRAS, 398, 1150

Brook C. B., et al., 2012, MNRAS, 426, 690

Buck T., 2020, MNRAS, 491, 5435

Bustamante S., Sparre M., Springel V., Grand R. J. J., 2018, MNRAS, 479, 3381

Casagrande L., Schönrich R., Asplund M., Cassisi S., Ramírez I., Meléndez J., Bensby T., Feltzing S., 2011, A&A, 530, A138

Cavichia O., Mollá M., Costa R. D. D., Maciel W. J., 2014, MNRAS, 437, 3688

Clarke A. J., et al., 2019, MNRAS, 484, 3476

Croton D. J., et al., 2006, MNRAS, 365, 11

Croton D. J., et al., 2016, ApJ, 222, 22

Davé R., Anglés-Alcázar D., Narayanan D., Li Q., Rafieferantsoa M. H., Appleby S., 2019, MNRAS, 486, 2827

De Lucia G., Blaizot J., 2007, MNRAS, 375, 2

DeFelippis D., Genel S., Bryan G. L., Fall S. M., 2017, ApJ, 841, 16

Di Matteo P., Haywood M., Combes F., Semelin B., Snaith O. N., 2013, A&A, 553, A102

Dolag K., Borgani S., Murante G., Springel V., 2009, MNRAS, 399, 497

Dubois Y., et al., 2014, MNRAS, 444, 1453

Dutton A. A., 2009, MNRAS, 396, 121

Efstathiou G., Lake G., Negroponte J., 1982, MNRAS, 199, 1069

El-Badry K., Wetzel A., Geha M., Hopkins P. F., Kereš D., Chan T. K., Faucher-Giguère C.-A., 2016, ApJ, 820, 131

Elmegreen B. G., Scalo J., 2004, ARAA, 42, 211

Fall S. M., Efstathiou G., 1980, MNRAS, 193, 189

Fanali R., Dotti M., Fiacconi D., Haardt F., 2015, MNRAS, 454, 3641

Font A. S., et al., 2020, MNRAS, 498, 1765

Forbes J., Krumholz M., Burkert A., 2012, ApJ, 754, 48

Forbes J. C., Krumholz M. R., Burkert A., Dekel A., 2014, MNRAS, 438, 1552

Forbes J. C., Krumholz M. R., Speagle J. S., 2019, MNRAS, 487, 3581

Fragkoudi F., et al., 2020, MNRAS, 494, 5936

Frankel N., Rix H.-W., Ting Y.-S., Ness M., Hogg D. W., 2018, ApJ, 865, 96

Frankel N., Sanders J., Ting Y.-S., Rix H.-W., 2020, ApJ, 896, 15

Fu J., et al., 2013, MNRAS, 434, 1531

Fuhrmann K., 1998, A&A, 338, 161

Gaia Collaboration 2016, A&A, 595, A1

Gaia Collaboration 2021, A%A, 649, A1

Genel S., Vogelsberger M., Nelson D., Sijacki D., Springel V., Hernquist L., 2013, MNRAS, 435, 1426

Genzel R., Eisenhauer F., Gillessen S., 2010, Reviews of Modern Physics, 82, 3121

Georgelin Y. M., Georgelin Y. P., 1976, A&A, 49, 57

Goldbaum N. J., Krumholz M. R., Forbes J. C., 2015, ApJ, 814, 131

Goldbaum N. J., Krumholz M. R., Forbes J. C., 2016, ApJ, 827, 28

Grand R. J. J., Kawata D., Cropper M., 2012a, MNRAS, 421, 1529

Grand R. J. J., Kawata D., Cropper M., 2012b, MNRAS, 426, 167

Grand R. J. J., Kawata D., Cropper M., 2015, MNRAS, 447, 4018

Grand R. J. J., Springel V., Gómez F. A., Marinacci F., Pakmor R., Campbell D. J. R., Jenkins A., 2016, MNRAS, 459, 199

Grand R. J. J., et al., 2017, MNRAS, 467, 179

Grand R. J. J., et al., 2018, MNRAS, 474, 3629

Grand R. J. J., et al., 2019, MNRAS, 490, 4786

Guo Q., et al., 2011, MNRAS, 413, 101

Halle A., Di Matteo P., Haywood M., Combes F., 2018, A&A, 616, A86

Hayden M. R., et al., 2015, ApJ, 808, 132

Haynes M. P., et al., 2011, AJ, 142, 170

Haywood M., 2008, MNRAS, 388, 1175

Haywood M., Di Matteo P., Lehnert M. D., Katz D., Gómez A., 2013, A&A, 560, A109

Helmi A., 2020, ARAA, 58, 205

Henriques B. M. B., White S. D. M., Thomas P. A., Angulo R., Guo Q., Lemson G., Springel V., Overzier R., 2015, MNRAS, 451, 2663

Henriques B. M. B., Yates R. M., Fu J., Guo Q., Kauffmann G., Srisawat C., Thomas P. A., White S. D. M., 2020, MNRAS, 491, 5795

Herpich J., Stinson G. S., Rix H. W., Martig M., Dutton A. A., 2017, MNRAS, 470, 4941

Hirschmann M., Dolag K., Saro A., Bachmann L., Borgani S., Burkert A., 2014, MNRAS, 442, 2304

Hopkins P. F., et al., 2018, MNRAS, 480, 800

Hubble E., 1929a, PNAS, 15, 168

Hubble E. P., 1929b, ApJ, 69, 103

Hunt J. A. S., Hong J., Bovy J., Kawata D., Grand R. J. J., 2018, MNRAS, 481, 3794

Irodotou D., et al., 2022, MNRAS, 513, 3768

Johnson J. W., et al., 2021, MNRAS, 508, 4484

Jones M. G., Haynes M. P., Giovanelli R., Moorman C., 2018, MNRAS, 477, 2

Jurić M., et al., 2008, ApJ, 673, 864

Kawata D., Baba J., Ciucă I., Cropper M., Grand R. J. J., Hunt J. A. S., Seabroke G., 2018, MNRAS, 479, L108

Kennicutt Robert C. J., 1998, ApJ, 498, 541

Kereš D., Katz N., Weinberg D. H., Davé R., 2005, MNRAS, 363, 2

Khoperskov S., Haywood M., Snaith O., Di Matteo P., Lehnert M., Vasiliev E., Naroenkov S., Berczik P., 2021, MNRAS, 501, 5176

Kordopatis G., et al., 2015, MNRAS, 447, 3526

Kormendy J., 2013, in Falcón-Barroso J., Knapen J. H., eds, , Secular Evolution of Galaxies. p. 1

Kormendy J., Kennicutt Robert C. J., 2004, ARAA, 42, 603

Krumholz M., Burkert A., 2010, ApJ, 724, 895

Krumholz M. R., Burkhart B., Forbes J. C., Crocker R. M., 2018, MNRAS, 477, 2716

Kubryk M., Prantzos N., Athanassoula E., 2013, MNRAS, 436, 1479

Kubryk M., Prantzos N., Athanassoula E., 2015, A&A, 580, A126

Lacey C. G., Fall S. M., 1985, ApJ, 290, 154

Lacey C. G., et al., 2016, MNRAS, 462, 3854

Leroy A. K., Walter F., Brinks E., Bigiel F., de Blok W. J. G., Madore B., Thornley M. D., 2008, AJ, 136, 2782

Lin D. N. C., Pringle J. E., 1987, ApJ, 320, L87

Lin C. C., Shu F. H., 1964, ApJ, 140, 646

Loebman S. R., Roškar R., Debattista V. P., Ivezić Ž., Quinn T. R., Wadsley J., 2011, ApJ, 737, 8

Lynden-Bell D., Kalnajs A. J., 1972, MNRAS, 157, 1

Ma X., Hopkins P. F., Wetzel A. R., Kirby E. N., Anglés-Alcázar D., Faucher-Giguère C.-A., Kereš D., Quataert E., 2017, MNRAS, 467, 2430

Mackereth J. T., et al., 2019, MNRAS, 482, 3426

Majewski S. R., et al., 2017, AJ, 154, 94

Marinacci F., Pakmor R., Springel V., 2014, MNRAS, 437, 1750

Marinacci F., Grand R. J. J., Pakmor R., Springel V., Gómez F. A., Frenk C. S., White S. D. M., 2017, MNRAS, 466, 3859

Martig M., Minchev I., Flynn C., 2014, MNRAS, 442, 2474

Mayer L., Governato F., Kaufmann T., 2008, Advanced Science Letters, 1, 7

McMillan P. J., 2011, MNRAS, 414, 2446

Mikkola D., McMillan P. J., Hobbs D., 2020, MNRAS, 495, 3295

Minchev I., Famaey B., 2010, ApJ, 722, 112

Minchev I., Famaey B., Quillen A. C., Di Matteo P., Combes F., Vlajić M., Erwin P., Bland-Hawthorn J., 2012a, A&A, 548, A126

Minchev I., Famaey B., Quillen A. C., Dehnen W., Martig M., Siebert A., 2012b, A&A, 548, A127

Minchev I., Chiappini C., Martig M., 2013, A&A, 558, A9

Minchev I., Chiappini C., Martig M., 2014, A&A, 572, A92

Minchev I., Martig M., Streich D., Scannapieco C., de Jong R. S., Steinmetz M., 2015, ApJ, 804, L9

Mo H. J., Mao S., White S. D. M., 1998, MNRAS, 295, 319

Mo H., van den Bosch F. C., White S., 2010, Galaxy Formation and Evolution

Naab T., Burkert A., 2003, ApJ, 597, 893

Navarro J. F., Benz W., 1991, ApJ, 380, 320

Nelson D., Genel S., Vogelsberger M., Springel V., Sijacki D., Torrey P., Hernquist L., 2015, MNRAS, 448, 59

Nelson D., et al., 2018, MNRAS, 475, 624

Nelson D., et al., 2019, MNRAS, 490, 3234

Netopil M., Oralhan İ. A., Çakmak H., Michel R., Karataş Y., 2022, MNRAS, 509, 421

Nidever D. L., et al., 2014, ApJ, 796, 38

Nordström B., et al., 2004, A&A, 418, 989

Nuza S. E., Scannapieco C., Chiappini C., Junqueira T. C., Minchev I., Martig M., 2019, MNRAS, 482, 3089

Okalidis P., Grand R. J. J., Yates R. M., Kauffmann G., 2021, MNRAS, 504, 4400

Okalidis P., Grand R. J. J., Yates R. M., Springel V., 2022, MNRAS, 514, 5085

Pakmor R., Marinacci F., Springel V., 2014, ApJ, 783, L20

Pakmor R., Springel V., Bauer A., Mocz P., Munoz D. J., Ohlmann S. T., Schaal K., Zhu C., 2016, MNRAS, 455, 1134

Pakmor R., et al., 2017, MNRAS, 469, 3185

Pakmor R., Guillet T., Pfrommer C., Gómez F. A., Grand R. J. J., Marinacci F., Simpson C. M., Springel V., 2018, MNRAS, 481, 4410

Pakmor R., et al., 2020, MNRAS, 498, 3125

Peebles P. J. E., 1971, A&A, 11, 377

Pezzulli G., Fraternali F., 2016, MNRAS, 455, 2308

Pillepich A., et al., 2018, MNRAS, 475, 648

Planck Collaboration 2014, A&A, 571, A16

Planck Collaboration 2020, A&A, 641, A6

Press W. H., Schechter P., 1974, ApJ, 187, 425

Quillen A. C., Minchev I., Bland-Hawthorn J., Haywood M., 2009, MNRAS, 397, 1599

Radburn-Smith D. J., et al., 2012, ApJ, 753, 138

Rees M. J., Ostriker J. P., 1977, MNRAS, 179, 541

Renaud F., Agertz O., Andersson E. P., Read J. I., Ryde N., Bensby T., Rey M. P., Feuillet D. K., 2021, MNRAS, 503, 5868

Roškar R., Debattista V. P., Stinson G. S., Quinn T. R., Kaufmann T., Wadsley J., 2008, ApJ, 675, L65

Ruiz-Lara T., et al., 2017, A&A, 604, A4

Schaye J., et al., 2015, MNRAS, 446, 521

Schmidt T. M., Bigiel F., Klessen R. S., de Blok W. J. G., 2016, MNRAS, 457, 2642

Schönrich R., Binney J., 2009, MNRAS, 396, 203

Schönrich R., McMillan P. J., 2017, MNRAS, 467, 1154

Sellwood J. A., Binney J. J., 2002, MNRAS, 336, 785

Sellwood J. A., Evans N. W., 2001, ApJ, 546, 176

Sellwood J. A., Moore E. M., 1999, ApJ, 510, 125

Sellwood J. A., Sánchez R. Z., 2010, MNRAS, 404, 1733

Sheth K., et al., 2008, ApJ, 675, 1141

Solway M., Sellwood J. A., Schönrich R., 2012, MNRAS, 422, 1363

Somerville R. S., Hopkins P. F., Cox T. J., Robertson B. E., Hernquist L., 2008, MNRAS, 391, 481

Speights J. C., Godwin C., Reimer R., Benton A., Lemaire R., 2019, ApJ, 883, 77

Spitoni E., Matteucci F., 2011, A&A, 531, A72

Springel V., 2010, MNRAS, 401, 791

Springel V., 2016, Saas-Fee Advanced Course, 43, 251

Springel V., Hernquist L., 2003, MNRAS, 339, 289

Springel V., White S. D. M., Tormen G., Kauffmann G., 2001, MNRAS, 328, 726

Springel V., et al., 2005, Nature, 435, 629

Springel V., Frenk C. S., White S. D. M., 2006, Nature, 440, 1137

Springel V., et al., 2018, MNRAS, 475, 676

Stevens A. R. H., Croton D. J., Mutch S. J., 2016, MNRAS, 461, 859

Stevens A. R. H., Lagos C. d. P., Contreras S., Croton D. J., Padilla N. D., Schaller M., Schaye J., Theuns T., 2017, MNRAS, 467, 2066

Stevens A. R. H., Lagos C. d. P., Obreschkow D., Sinha M., 2018, MNRAS, 481, 5543

Toomre A., 1964, ApJ, 139, 1217

Tremonti C. A., et al., 2004, ApJ, 613, 898

Tully R. B., Fisher J. R., 1977, A&A, 54, 661

Vallée J. P., 2014, AJ, 148, 5

Vera-Ciro C., D'Onghia E., Navarro J., Abadi M., 2014, ApJ, 794, 173

Verma K., Grand R. J. J., Silva Aguirre V., Stokholm A., 2021, MNRAS, 506, 759

Vogelsberger M., Genel S., Sijacki D., Torrey P., Springel V., Hernquist L., 2013, MNRAS, 436, 3031

Vogelsberger M., Marinacci F., Torrey P., Puchwein E., 2020, Nature Reviews Physics, 2, 42

Walcher C. J., et al., 2016, A&A, 594, A61

Wang J., et al., 2014, MNRAS, 441, 2159

Wang L., Dutton A. A., Stinson G. S., Macciò A. V., Penzo C., Kang X., Keller B. W., Wadsley J., 2015, MNRAS, 454, 83

Wegg C., Gerhard O., 2013, MNRAS, 435, 1874

Weinberger R., Springel V., Pakmor R., 2020, ApJs, 248, 32

White S. D. M., Frenk C. S., 1991, ApJ, 379, 52

White S. D. M., Rees M. J., 1978, MNRAS, 183, 341

Wong T., Blitz L., Bosma A., 2004, ApJ, 605, 183

Yang C.-C., Krumholz M., 2012, ApJ, 758, 48

Yates R. M., Henriques B., Thomas P. A., Kauffmann G., Johansson J., White S. D. M., 2013, MNRAS, 435, 3500

Yates R. M., Henriques B. M. B., Fu J., Kauffmann G., Thomas P. A., Guo Q., White S. D. M., Schady P., 2021, MNRAS, 503, 4474

Zwaan M. A., Meyer M. J., Staveley-Smith L., Webster R. L., 2005, MNRAS, 359, L30

van den Bosch F. C., Abel T., Croft R. A. C., Hernquist L., White S. D. M., 2002, ApJ, 576, 21

van der Kruit P. C., Freeman K. C., 2011, ARAA, 49, 301

Acknowledgements

First and foremost I would like to thank my supervisor Volker Springel who provided me with valuable input and support, was always approachable and kind and eventually guided me towards the completion of my PhD degree. A most sincere thanks to the two postdocs that I collaborated during my time at MPA, Rob Grand and Rob Yates. They were present at all stages of the degree, welcomed me at MPA, shared with their expertise in simulations and semi-analytic models, believed in me, improved my research skills, allowed me to bother them with all sorts of questions and were always willing to meet in person or online. I also thank Guinevere Kauffmann for her contribution to ideas and guidance at the early stages of my PhD projects and Eiichiro Komatsu for assisting me as a member of my PhD committee. Similarly I thank Klaus Dolag for agreeing to be the second reader of my thesis and Joseph Mohr and Gerhard Buchalla for participating in my oral defense. Lastly, I thank the secretaries at MPA; Maria, Gabi, Cornelia and Sonja for their help with every problem during my 4 years at the institute.

A very special thanks to the best friends I could make at MPA, Abhijeet, Ilkham and Spandan. We were together in this PhD journey from the first to the last moment. It is rare for 4 people to all just click together so well. Countless lunches, dinners, coffee breaks, discussions. So many activities, be it movies or escape rooms or going to the stadium or the shops. We travelled as far and wide as we could, seeing beautiful places and making so many memories. Thank you guys and may we always be in touch. I should also thank Aniket and Andrija for always being around for a chat.

Further, I want to thank my high school physics teachers from Arsakeio high school who truly inspired me to follow this career path, Mr Kavardinas, Mr Temperekidis, Mr Chrysovergis and Ms Polyzopoulou. I also thank Mr Zachilas for getting me engaged with astronomy. Moreover, I should thank the people who I collaborated with in my time at the University of Edinburgh, my personal tutor Ken Rice, my master and bachelor project supervisor Sadegh Khochfar and Michal Michalowski. They really opened the door for me to pursue a competitive PhD degree.

Of course I should thank my family, my mother Vassiliki, my father Vassilis and my sister Argietta who love me beyond limits and are always supporting me in everything I do. It was so valuable that I could talk to them every day and that they managed to visit me so many times in Munich. A special thanks to my grandpa Lefteris and grandma Argietta for offering me their unconditional love and who faced some hard times these years but still going strong hopefully for many years to come. I also thank my uncles (Antonis, Christos and Fotis), aunts (Areti and Chara) and cousins (Ioanna, Lefteris, Konstantina, Vangelis, Michalis) for always welcoming me with warmth when visiting Greece and communicating often on my progress.

Finally, I thank all my good friends in Greece who were always up for a call to share our news and were keen on meeting when I was visiting home, Christos, Thanasis, Angelos, Stefanos, Giorgos, Michalis, Vassilis P., Vassilis M., Nikos, Achilleas, Marios, Thanasis P. and Konstantinos.